Università degli Studi di Torino

Doctoral School of the University of Torino

PhD program in Pharmaceutical and Biomolecular Sciences

(XXXV cycle)

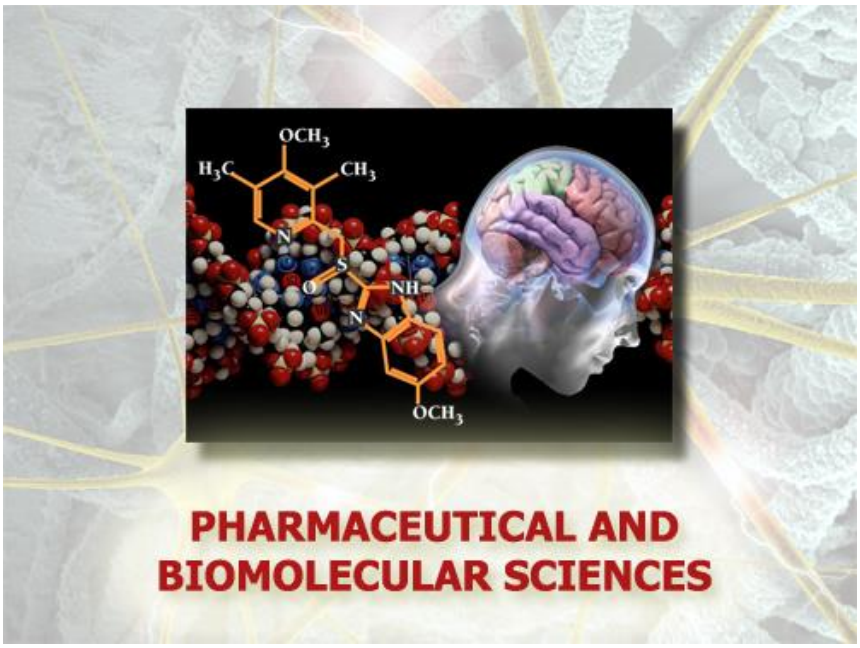

Surface key features of silica particles mediating toxicological responses at the molecular level.

Candidate: Chiara Bellomo

Tutor: Prof. Francesco Turci

Co-tutor: Dr. Cristina Pavan

Università degli Studi di Torino

PhD program in Pharmaceutical and Biomolecular Sciences

Department of Chemistry

Cycle: XXXV

Title: Surface key features of silica particles mediating toxicological responses at the molecular level.

CANDIDATE: Chiara Bellomo

TUTOR: Prof. Francesco Turci
CO-TUTOR: Dr. Cristina Pavan

Jury Members:

Prof. Francesca Cecchet	**Université de Namur**
Prof. Francesco Di Benedetto	**Università degli Studi di Ferrara**
Prof. Piero Ugliengo	**Università degli Studi di Torino**

Coordinator of the PhD program: Prof.ssa Roberta Cavalli

Academic Years: AA 2019-2020, AA 2020-2021, AA 2021-2022.
SETTORE SCIENTIFICO-DISCIPLINARE: CHIM/03 – Chimica Generale e Inorganica.

This PhD work has been carried out at the Department of Chemistry of the University of Turin and at the Interdepartmental Scansetti Center for the study of asbestos and other toxic particulates.

The PhD project is part of the Eurosil project part 2, funded by the European Association of Crystalline Silica Producers, to which Chiara Bellomo is grateful.

Abbreviations

ALF = Artificial Phagolysosome Fluid
ANSES = French Agency of Food, Environmental and Occupational Health and Safety.
AM = Alveolar Macrophage
AOP = Adverse Outcome Pathway
AOT = dioctyl sulfosuccinate sodium salt
b.t. = beam temperature
BET = Brunauer–Emmett–Teller
BSA = bovine serum albumin
CMC = critical micellar concentration
CPMC method = ground-state constrained-path Monte Carlo method
DCS = Differential Scanning Centrifuge
DFT = Density Functional Theoy
DLS = Dynamic Light Scattering
DO = dioleoyl
DOPS = dioleoyl phosphatidylserine
DOPC = dioleoyl phosphatidylcholine
DPPC = dipalmitoyl phosphatidylcholine
DPPS = = dipalmitoyl phosphatidylserine
EM = Electron Microscopy
EPR = Electron Paramagnetic Resonance
FESEM = Field Emission Scanning Electron Microscopy
FTIR = Fourier-transform infrared spectroscopy
HEPES = 4-(2-hydroxyethyl)-1-piperazineethanesulfonic acid
HF= Hydrofluoric Acid
HOMO = Highest Occupied Molecular Orbital
HR-TEM = High Resolution Transmission Electron Microscopy
Hz = Hertz
IARC = International Agency for the Research on Cancer.
IR = Infra-Red
MIE = Molecular Initiating Event
NFS = nearly free silanols
(n)MR = (n) Membered Ring
OPO = Optical Paramagnetic Oscillator
PC = phosphatidylcholine
PL = phospholipid
PS = phosphatidylserine
PSD = Particle size Distribution
PBS = phosphate buffer solution

RBC = red blood cell
RCS = Respirable Silica Particles
RH = relative humidity
RNS = Reactive Nitrogen Species
ROS = Reactive Oxygen Species
RT = room temperature (25°C)
SBF = simulated biological fluids
SFG = Sum-Frequency Generation
SM = Sphingomyelin
SSA = Specific Surface Area
SSLB = Solid Supported Lipid Bilayer
SS-NMR = solid-state Nuclear Magnetic Resonance
TGA = Thermogravimetric Analysis
TRX = Triton-X
XRPD = X-Ray Powder Diffraction.

List of publications

1. C. Pavan, G. Escolano-Casado, C. Bellomo, S. Cananà, M. Tomatis, R. Leinardi, L. Mino, F. Turci, Nearly free silanols drive the interaction of crystalline silica polymorphs with membranes: implications for mineral toxicity. **2023**, Frontiers in Chemistry, 10, 1092221.

2. C. Bellomo, C. Pavan, G. Fiore, G. Escolano-Casado, L. Mino, F. Turci, Top-down preparation of nanoquartz for toxicological investigations. **2022**, International Journal of Molecular Sciences, 23(23), 15425.

3. S. Cananà, C. Pavan, C. Bellomo, G. Escolano-Casado, G. Chilla, D. Lison, L. Mino, F. Turci, Interaction of Layered Silicates with Biomembranes: Ion Exchangers and Non-Exchangers. **2022**, Advanced Materials Interfaces, 9(29), 2201347.

4. C. Pavan, M. J. Sydor, C. Bellomo, R. Leinardi, S. Cananà, R. L. Kendall, E. Rebba, M. Corno, P. Ugliengo, L. Mino, A. Holian, F. Turci, Molecular recognition between membrane epitopes and nearly free surface silanols explains silica membranolytic activity. **2022**, Colloids and Surfaces B: Biointerfaces, 217, 112625.

Table of contents

CHAPTER 1: Introduction

1.1 Crystalline silica. A well-known toxic particle.

1.1.1 Silica

The Silicon atom (Si) is the second most abundant atom present on Earth, and represents ca. 28% by weight of the Earth's crust. Silicon is mainly bound to oxygen in two vast classes: oxides and silicates.
Silicon dioxide is the chemical definition of a series of species characterized by silicon and oxygen atoms combined. The empirical formula of this chemical species is SiO_2 and it is usually called silica. In most of the cases, the silicon atom is surrounded by four oxygen atoms which have a direct bond with it (Figure 1.1), forming a tetrahedron. The bond in the solid has a double nature, because of the electronegativity (χ) of the two atoms. According to the Pauling's method, silicon has an electronegativity of 1.9 and oxygen of 3.44. [1] A ionic solid is formed when the difference of electronegativity is 2 or more. Considering that the value in the case of silica is 1.54, the nature of the bond is both covalent and ionic. Still, it is not considered a ionic solid (such as MgO), but a covalent solid with some deviation from the covalent behavior due to the high polarity of the Si–O bond.[2]

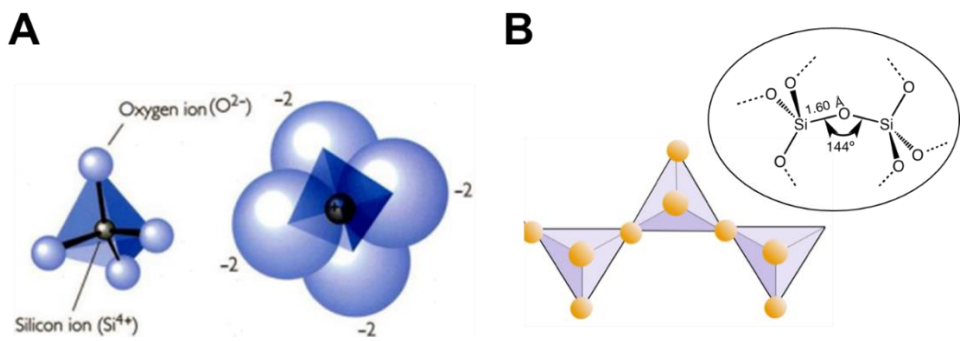

Figure 1.1: Structure of silica (A) Silica tetrahedron in ball and stick representation (on the left) and with the actual atomic dimension (on the right); (B) tetrahedral organization of silica, and focus on the angle Si–O–Si connecting different tetrahedra units.

The tetrahedral organization of silica is rigid, but the angle Si–O–Si which connects two distinct tetrahedra is flexible, giving rise to a wide range of silica based materials, both crystalline and amorphous.[3]
Table 1.1 reports the most common types of silica-based materials.
When silica is in its crystalline form, it has a group of polymorphs which organize the structure in regular long-range arrangements, and can be formed at different conditions of temperature and pressure (Figure 1.2). The crystalline polymorphs of silica are quartz, tridymite, coesite, cristobalite and stishovite, but quartz is the most common among them, and the most thermodynamically stable at room temperature. Among the other polymorphs, the most common are cristobalite and tridymite, (founded mostly in volcanic ashes) but their abundance is low because of the difficulty to obtain them, since a rapid cooling at room temperature is needed.[4]
Stishovite is the only silica polymorph characterized by a rutile geometry, with a octahedral coordination geometry, with silicon bounded to six oxygen instead of four (SiO_6). Accordingly, it is denser and harder. [5, 6]

Table 1.1: Most common silica forms, divided by crystal structure and origin.

	Natural	**Synthetic**
Crystalline	quartz cristobalite tridymite coesite stishovite	quartz crystals porosils
Amorphous	vitreous silica opal diatomaceous earth	pyrogenic silica colloidal silica precipitated silica silica gel mesoporous silica

Examples of synthetic crystalline forms of silica (Table 1.1, line 1), are reported in literature. [8, 9] Among them, some examples of quartz crystals were recently reported in literature, along with porosils. [10, 11]
At the opposite, a few examples of amorphous silica particles are present in nature, in the forms of opals and vitreous silica, but many examples can be observed of synthetic silica nanoparticles. Amorphous silica is normally characterized by disordered structures, random networks without any periodicity. Silica particles can be synthetized starting from a templating agent dissolved in water and treated with different conditions of pH, temperature and pressure. Amorphous silicas are used in a wide range of applications, as research, desiccant, additives, nanomedicine and drug delivery. [12]

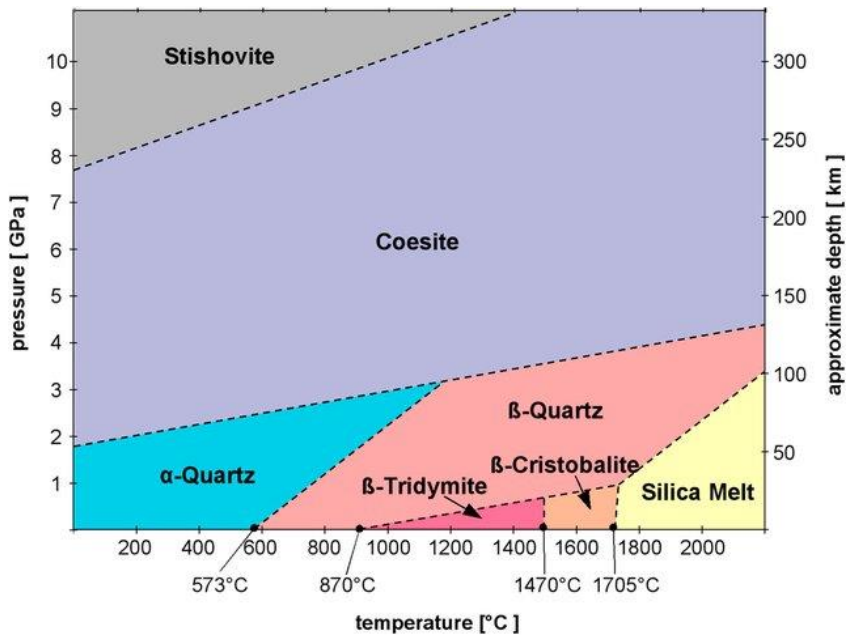

Figure 1.2: phase diagram of crystalline silica polymorphs. Reproduced from [7].

1.1.1.1 Quartz

Quartz is the most common crystalline polymorph in the Earth crust and the only thermodynamically stable at the normal conditions of pressure and temperature. Around the 12% in weight of the Earth crust is composed by quartz, and it is second most abundant material after feldspar. [13]
As evidenced in Figure 1.3A, quartz is organized in six-membered rings in the bulk, with six silicon atoms and six oxygen atoms. The order is broken on the surface, in which the rings are open and the atoms are exposed to the external environment. This six-membered rings organization is not found in amorphous silica, in which the rings are composed by a casual number of atoms without any periodicity.[3]
Quartz exists in two forms, α and β quartz. The two forms are an example of a displacive transformation, which involves the stretching of the bonds and the modification of the angles between the tetrahedra, without the breakage the bonds. [14] In fact, α-quartz is a trigonal system, β-quartz is an hexagonal system, which crystallizes at 573°C (Figure 1.3B). [15] The transformation is reversible because β-quartz is metastable, and reorganize after the cooling of the material. Nonetheless, there is a relevant change in volume between the two phases, which can lead to micro fracturing of the Earth's crust and other materials. [16, 17]

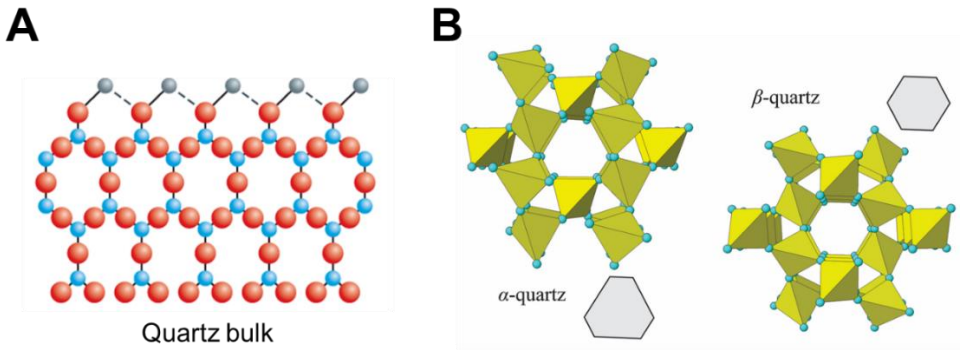

Figure 1.3: crystalline structure of quartz. (A) six-membered ring organization of quartz bulk In blue Si atoms, in red O atoms, in grey hydrogen atoms on the surface. Adapted from [18] (B) α and β quartz geometries. Reproduced from [19].

1.1.2 Exposure to crystalline silica and toxic effects.

The inhalation of Respirable Crystalline Silica (RCS) is related to several diseases of occupational origin. [20, 21] RCS is defined as the airborne fraction of crystalline silica particles smaller than 10 µm, with a median value of 4.25 µm [22, 23]. RCS is able to reach the lung alveoli when inhaled. The first and most common disease related to RCS is silicosis. Silicosis is known to be one of the most ancient disease known by humankind. [24, 25] It is a pulmonary disease which affects people who chronically inhale dusts with RCS in it. The illness is characterized by the inflammation and the scarring of the lung parenchyma, leading to a particular form of fibrosis called pneumoconiosis. Even if the acknowledgement of the negative consequences of breathing dusts was already assessed by ancient Greeks and Romans, [26] only by the 1800s the death of silicosis was recognized and associated to silica exposure. [27] A contribution to this late association is due to the delay between the exposure to silica dust and the expression of the symptoms, especially in the chronic form. In fact, according to the different exposure to dust containing crystalline silica, the silicosis can be acute or chronic. The acute form is characterized by multiple symptoms, such as shortness of breath, fever, cough and cyanosis, and it appears with high concentrations of crystalline silica and in a low amount of time (weeks-months). The chronic form is associated to a lower exposure to silica dust, and it is the most common of the silicosis forms. [28, 29] Silicosis is the most common occupational disease in the world, with thousands of deaths each year in working environment, especially in underdeveloped countries. [30] China, for example, from 1991 to 1995, registered 24000 silicosis deaths each year. For silicosis there is no cure, [31] but it is possible to prevent the illness by avoiding the inhalation of

silica containing dusts. Thanks to stricter regulations and the use of protective measures (masks, respirators, dust control systems) the death rate declined easily, especially in developed countries. [32, 33] Almost all the cases of silicosis are reported in a working environment, in which the silica dust is manipulated, such as in mining, sandblasting, pottery and ceramics, glass production, construction, and painting. [34] In all these occupations, silica dust is cut, grinded, drilled and crushed. Silicosis cases are not reported in non-occupational environments, except for some cases of long-term exposure to sand dust in desert areas. However, in those cases silicosis is coupled with another lung disorder (Al Eskan disease). [35, 36]

Silicosis pathophysiology starts when the RCS is inhaled and reaches the alveolar sacs in the lung. When the particle is in the alveolar sac, it is no longer possible to clear it with cough and mucus. Alveolar macrophages (AMs), the deputy cells for the clearance of the tissues from foreign bodies, eat the particles and start an inflammatory response. This inflammation stimulates the proliferation of fibroblasts which produce collagen to isolate the particle and avoid a further inflammation. These actions, however, generate various fibrotic lesions in the lungs, called silicotic nodules, characterized by a central necrotic area, surrounded by laminar masses of collagen and with several types of inflammatory cells in periphery. The silicotic nodules are specifically generated by crystalline silica, thus their presence is directly related to it. [37] Multiple scar lesions of this kind diminish the elasticity of the lung, and lead to a reduced pulmonary activity and to a serious damage of the organ. [29, 38]

In first world countries, the prevention of this pathology is successful, but new outbreaks of silicosis are documented in sandblasting denim operations and in the installation of engineered stone countertops. Particularly impacting is the death of an Australian worker in dry cutting, dead before his 40s. [38-44] Therefore, even if the prevention has improved markedly, silicosis remains a great occupational issue which must be taken under control.

Apart from silicosis, other pathologies are considered to be related with the RCS occupational inhalation.

Several epidemiological studies highlighted an association between RCS and lung cancer. [34, 45-47] However, no direct correlation was found, both in the generation of lung tumor and in the acceleration of it. Still, the International Agency for the research on Cancer (IARC) decided in 1997 and confirmed in 2012 the classification of respirable crystalline silica particles in Group 1 as carcinogenic to humans, because there were sufficient empirical evidence of the carcinogenicity of silica on animals and humans. [48, 49] Finally, silica exposure has been associated also with some autoimmune diseases, such as chronic renal disease, rheumatoid arthritis and systemic sclerosis.[50-53]

1.1.3 The cellular mechanism related to silica induced lung injury.

At the beginnings of the 2000s, the protein complex called inflammasome was discovered. Inflammasome is able to trigger an inflammatory reaction in response to a plethora of external stimuli, and silica was one of them. Thanks to this discovery, the knowledge about the inflammatory path of silica particles had a big improvement. [54, 55]

Several mechanisms have been proposed in the following years and IARC was able to summarize them in its report in 2012. [48] The details go beyond the purpose of this thesis, therefore only the general aspects will be reported here.

As schematized in Figure 1.4, RCSs arrive in the alveoli coated with surfactants and phospholipids. The airway lining layer is the first line of interaction between silica particles and the lungs and is covered by a surfactant film. The contact between the particle and a biological medium rich in biomolecules, such as pulmonary surfactants and plasma, results in the formation of the "biomolecular protein corona", which consists in the adsorption of proteins and lipids on the surface of the particle until the full coverage. [56, 57] The proteins which are statistically more abundant in the biological milieu are first adsorbed on the surface, and then gradually replaced by proteins with higher affinity for the particle chemical nature. [58][59] The composition of the protein corona is dependent by the surface features of silica particles. It is still unresolved if this protein corona favors the interaction of the particle with the alveolar macrophages, or the interaction occurs with the nude particle.

After arriving in the alveoli, the particles are detected as foreign bodies, and they elicit the response of the immune system in the form of the alveolar macrophages (AM). AM express a variety of receptors on the surface able to uptake silica particles. When they came in contact, the particle is engulfed by AM into a phagosome fused with a lysosome, called phagolysosome. The phagolysosome has the ability to disrupt foreign bodies into low molecular weight products. [60] At this point, AMs can either succeed in the particle clearance or, on the contrary, be damaged and start inflammation.

Particles inside the phagolysosome can interact with the internal membrane and cause the destabilization and lysis. [62]. Recently, a paper from some of us [63], reported that the silica particle enters the AM with the molecular corona, but inside the phagolysosome the molecular corona is disrupted and the nude particle exposed, eliciting an inflammatory response. The lysis of the phagolysosome membrane is called membranolysis and it is the Molecular Initiating Event (MIE) of the inflammation path of silica particles. Lysosomal enzymes and RCSs are released in the cytoplasm and triggers AM death and inflammatory pathways (Figure 1.4).

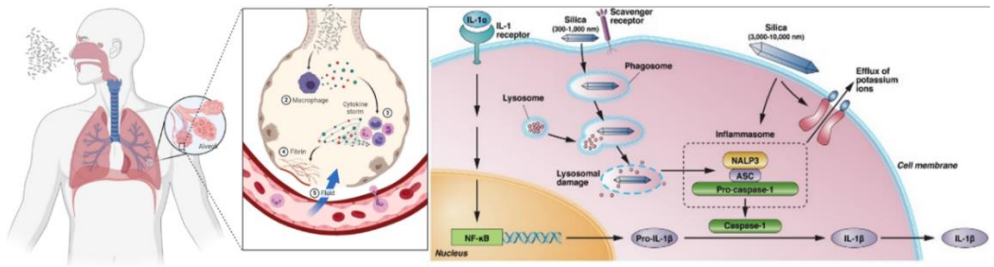

Figure 1.4: general scheme of the path of silica particles in the lungs. Adapted from [61].

The inflammation is the result of the activity of cell derived mediators and of activated biochemical cascades in response to cellular irritants, in this case silica particles. Silica particles cause the activation of AM, lymphocytes and epithelial cells and induce them to produce alarmins, cytokines, chemokines, growth factors, prostaglandins, reactive oxygen species (ROS) and reactive nitrogen species (RNS). [64-66] The two main transcriptional regulators of pro inflammatory responses to silica are the nuclear factor-*k*B and the activator protein-1. [66, 67] In the past decade, it was proved that the development of the lung inflammation produced by silica is predominantly caused by the NRLP3 inflammasome. [68] Inflammasomes in the body are cytosolic multiprotein oligomers responsible of the activation of inflammatory responses and present in the alveolar macrophage. [69] Cassel and coworkers [68] observed that the activation of macrophages induced by silica particles in the cytosol resulted in a strong secretion of interleukin 1β in a manner-dependent with the NRLP3 inflammasome. In fact, AM deficient of this inflammasome were incapable of secreting interleukins. The activation of the inflammasome causes the production of ROS and efflux of intracellular potassium. [70, 71] Inflammasome activation leads to a persistent inflammation, generated by the continuous recruitment of AMs and neutrophils. Bronchial and alveolar cells are then affected both by the production of AMs but also by the presence of the particles themselves. Inflammation factors are released, resulting in a stimulation of fibroblasts and collagen which then lead to the formation of the already described silicosis nodules (Paragraph 1.1.2). [64, 72-74]

1.1.4 The quartz hazard: a variable entity.

In 1997, IARC classified quartz in Group 1 as carcinogenic to humans. [49] Curiously, only quartz and another crystalline polymorph, cristobalite, were classified as carcinogenic to humans, but they are only a part of the forms that silica can be found in nature or produced (Table 1.1). [48] For instance,

amorphous silica was excluded by this classification, and in fact amorphous silica nanoparticles are widely used in pharmaceutical research. As a consequence, the pivotal idea was that the long range order of crystalline silica was the determinant feature able to provoke the membranolysis of phagolysosome in the AMs. [49, 75]

However, not all crystalline polymorphs of silica have the same effect. Quartz and cristobalite are highly toxic, but stishovite was found inert compared to quartz, cristobalite and tridymite. [76] But neither quartz itself is found equally pathogenic, and quartzes from different origins have different biological activity. [77] For instance, a complex study on the toxicity of a large panel of commercial quartz samples deriving from different industries showed a high variability in cytotoxicity, genotoxicity, inflammation and fibrogenic effects in *in vitro* and *in vivo* tests. [78-81] This variable effect was also observed in occupational settings. It was reported by Donaldson and Borm in 1998 that "carcinogenicity to humans was not detected in all industrial circumstances studied and that carcinogenicity may be dependent on inherent characteristics of the crystalline silica or on external factors affecting its biological activity". [77] Therefore, it is still difficult to find a two-way correlation between quartz and carcinogenicity effects, and IARC, even after the official classification in Group 1, confirmed this difficulty. As observed by Bruch in 2004, [78] "in the coal mining industry exposure to quartz in mixed dusts does not provoke the expected incidence of lung cancer corresponding to animal toxicological data. With regard to the specific situation in coal mining, IARC exempted these work sites from the general classification. Several experimental investigations have contributed information about the protective action of metallic ions such as iron, [82] or aluminum, [83, 84] which might derive from accompanying minerals in particular clay minerals. However, with regard to human exposure the adjustment of these experimental findings to the work site risk (non-coal mining) is controversial."[85]

Moreover, among the industrial silica flours analyzed though the years, Vallyathan and coworkers observed that crystalline silica when is just subjected to mechanical fracturing, a common process in occupational settings, has a stronger toxic potency than aged dust, because workers who directly fracture the dusts were more affected by occupational illnesses than workers who manipulate the dust after the fracturing (*i.e.,* for storing operations).[86]

On the contrary, no action was taken against all the amorphous silica forms. Even if it is proven that different types of amorphous silica have different chemical properties and can lead to different types of inflammations, still this inflammation *in vivo* is considered transient, probably due to better solubility

of amorphous silica particles than crystalline ones. [87] Nonetheless, also in the case of amorphous particles a certain variability *in vitro* and on animals was observed. While colloidal silica, silica gel and mesoporous silica are considered inert, pyrolytic silicas are highly reactive toward cell membranes and in animal models. [88-91] This means that the variability of the hazard of silica is not only related to crystalline silica, but it belongs to a wider panel of silica materials which comprehends also amorphous nanometric particles. [87, 92, 93]

In conclusion, all silicas are characterized by the same building block (SiO_2), but each type exhibits particular physicochemical features and surface functionalities which depend on the origin, the mechanical and the thermal manipulation of the dust, and the evolution with time of the dust. Thus, regardless of the crystal structure, other properties may impart a different toxic potential to silica particles. [94, 95]

1.2 Key physicochemical properties of silica relevant to toxicology.

Considering the peculiar variability of the silica hazard, the scientist formulated the hypothesis that the different toxic effect related to silica are linked to its physicochemical properties. The physicochemical properties are defined as the intrinsic physical and chemical characteristics of a substance.

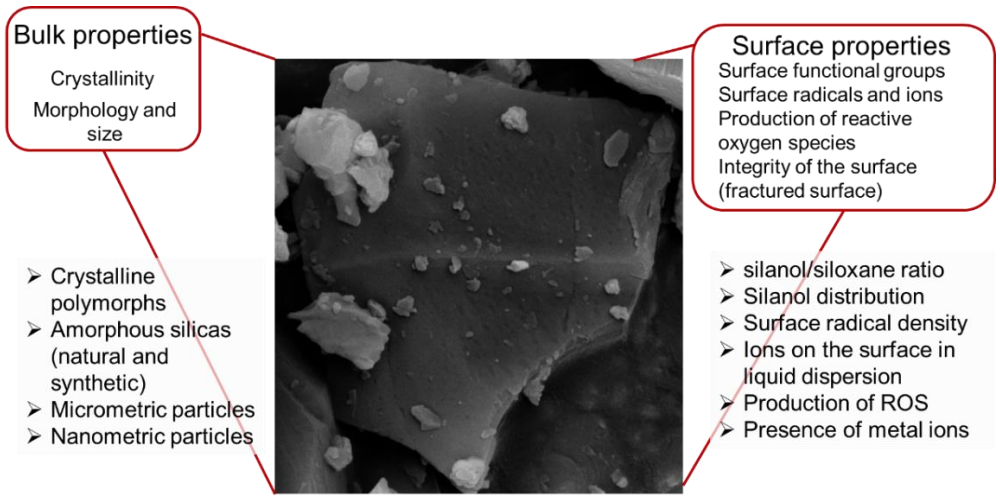

Figure 1.5: Physicochemical properties of silica determining the large variability of silica toxicity.

The variability in the biological effects of silica is primarily due to the multiplicity of silica sources (Table 1.1). Different origins differentiate silica

samples because of variable bulk and surface features. The differentiation between bulk and surface properties is quite important. Bulk properties define the crystal structure, and the size and the morphology of the particle. Surface features are controlled by surface radicals, surface functional groups, and surface charge in a dispersion medium. Figure 1.5 reports about the most important characteristics related to silica particles. In the following paragraphs some of them will be analyzed.

1.2.1 Bulk properties

1.2.1.1 Crystallinity

Crystallinity is the degree of long-range order of SiO_2. Crystalline SiO_2, as mentioned in Paragraph 1.1.1, occurs in several crystalline polymorphs, generated in different conditions of temperature and pressure (Figure 1.2). Among them, the most common is α-quartz, which is the central topic of this PhD thesis. The different crystal habits are characterized by a regular arrangement of the tetrahedra [SiO_4]. Conversely, in amorphous silica, the long-range order of tetrahedra is lost, even if a short-range order can sometimes be preserved in limited regions. However, the reason behind this extreme variability is the high flexibility of the Si–O–Si bridges between the tetrahedra, which give rise to a large panel of silica forms, from dense crystalline and amorphous structures (quartz and glasses) to aerogel and sponges (porous systems) to other mesoporous materials. [3]

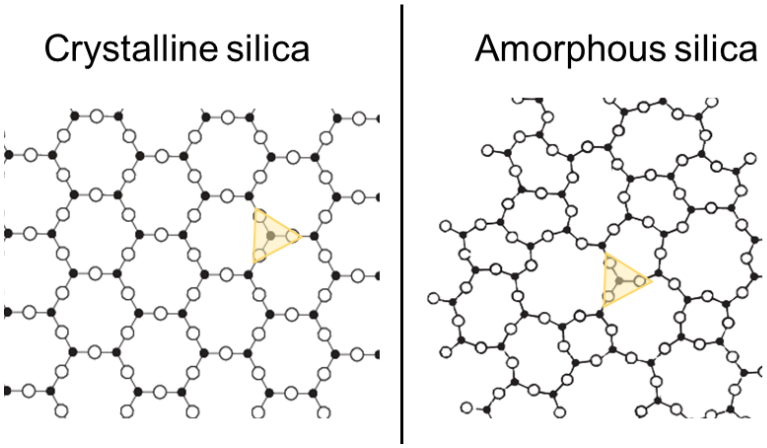

Figure 1.6: difference in the long range order between crystalline and amorphous silica. Black dots= Si atoms; white dots= oxygen atoms. This is a bidimensional representation of the material. The tetrahedron [SiO_4] is here represented as the triangle labeled in yellow.

1.2.1.2 Morphology and size of the particles

This feature is strictly dependent on the particle origin. Amorphous particles of synthetic origin are characterized by different morphologies according to their different synthesis. Pyrolytic silicas often exhibit aggregates of heterogeneous shape but a high specific surface area. However, they are usually difficult to disperse and assess the primary size of the particles. Colloidal silicas, on the other hand, are characterized by a regular spherical shape and a very good disaggregation behavior in liquid media. [89, 96]
For crystalline silica, the morphology is usually irregular and characterized by spikes, sharp edges and irregular forms. Quartz crystals are usually subjected to mechanical stress (Paragraph 1.1.2), which alter the regular morphology of an intact quartz crystal. Thus, the crystal morphologies are usually irregular, and the particles can range between the micrometric and the nanometric range. [97] Of particular interest are the peculiar conchoidal fractures observed on quartz of irregular morphology. Conchoidal fractures are usually characteristic of amorphous materials and are remnant of the vitreous origin of quartz, and they evidence the lack of preferential planes in the structure of quartz. More insights are reported in Chapter 1.3. In recent years, some synthetic procedures of quartz have been reported successfully, [8, 9, 98] and it was possible to observe a quartz with regular surfaces and edges an of micrometric/nanometric size.
Size is another crucial factor in the variability of silica bulk properties. Nanometric amorphous silicas are widely studied for their multiple applications in technology and pharmaceutics. Concerning crystalline silica, the core interest is related to respirable micrometric quartz particles (RCS), the ones related to occupational diseases. When quartz is subjected to mechanical stress, not only micrometric particles are usually generated, but also nanometric ones, which normally adhere on the surface of bigger particles. The characteristics of this nanometric fraction are unknown, because of the difficulty to separate it from the micrometric one.
Size has been claimed to have an impact on the inflammogenic activity of silica but with contrasting findings.[8, 99, 100]

1.2.2 Surface properties

In particle toxicology and in material chemistry, the bulk and the surface of a material are very distinct — though related — entities. In fact, the last atomic layer of a solid can be described as a discontinuity point, an interface between the underlying bulk structure and the surrounding medium (air, water, solvent, complex media like serum or blood). The surface of a solid is a complex and dynamic entity, that can actively interact with surrounding

medium, *e.g.*, undergoing protonation/deprotonation, adsorbing/desorbing moieties and biomolecules, reacting with molecules present in the external environment with the aim of catalyzing chemical transformations. [101] Thus, it is common that surface properties are crucially different than bulk properties, and should be investigated properly.

1.2.2.1 Surface functionalities: silanols and siloxanes.

The silica surface profile is for the most part characterized by silanol groups (≡Si-OH, =Si(OH)$_2$) and siloxane bridges (≡Si-O-Si≡). These two functional groups reside on the surface of the solid, except for occasional vacancies present in the bulk. While siloxane bridges are not in general classified for their distribution on the surface, this classification in done with silanols. Silanols are classified in different families according to their ability to establish mutual interactions, such as hydrogen bonds and/or Van del Walls weak interactions. They are considered responsible for the hydrophilic properties of silica particles, because of their ability to interact with external molecules through hydrogen bonding, being polar groups. [102, 103]

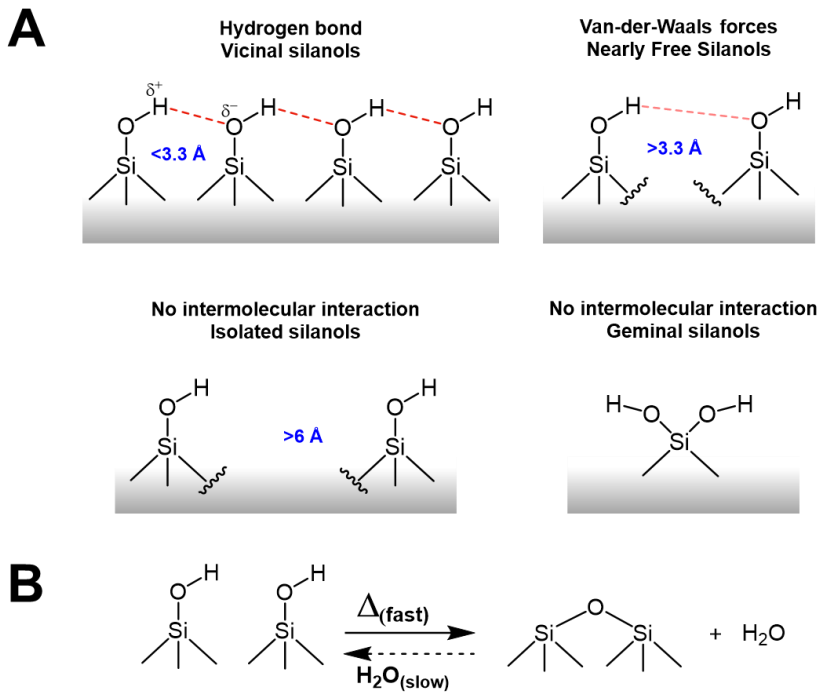

Figure 1.7: surface functional groups. (A) different silanol families on silica surface and their ability to engage intermolecular bonding between each other. (B) reaction of surface silanols and siloxanes in presence of heat and in presence of water.

As shown in Figure 1.7, silanol families might be classified according to their mutual intersilanol distances. Vicinal silanols and H-bonded silanols are defined by an intersilanol distance minor than 3.3 Å, around 2.5 Å. They are considered vicinal silanols when they share a common oxygen vertex. [3] They poorly interact with the external environment, because they are usually involved in hydrogen bonding between each other. [104, 105] H-bonded silanols, which are involved in strong intermolecular interactions with vicinal silanols but do not share a common oxygen atom, poorly interact with the external environment.

The weakly interacting silanols are a family of silanol which is separated for more than 3.3 but for less than 6 Å. They normally interact between each other though Van der Waals forces and are in general more prone to the interaction with the molecules present in the external environment than vicinal and H-bonded silanols. [106-108] A subfamily of the weakly interacting silanols are the nearly free silanols (NFS), recently identified by some of us [109]. NFS are found on the surface of fractured crystalline silica and on some amorphous pyrogenic silicas. They are characterized by an intersilanol distance of 4-6Å and they are very reactive toward the external environment. Isolated and geminal silanols, finally, are surface functionalities free to establish hydrogen bonds with external environment and can act as electron donor or acceptor, only if placed in the right position, because of the directional nature of the H-bonding. Curiously, the OH groups of a geminal silanol are unable to interact with each other. They are both generally quite rare in silica not thermically treated. [3, 110]

Silanols and siloxanes are present at different extent on all the silica particles, both crystalline and amorphous. They are detectable with several techniques, such as SS-NMR, Raman and Infrared Spectroscopy. [3] It is possible to probe the surface silanol content of silica particles by thermal treatment (Figure 1.7). [94]

Thermal treatment of silica particles can help to reduce the amount of surface silanols by condensation into siloxane rings, followed by the production of water molecules. The reaction can be reversed by the contact of water with the dehydrated silica surface, however, it appears to be slower. To obtain a strong hydration of the silica surface is necessary to work in an hydrothermal environment, at 250°C and at high pressures of water vapor and humidity. Except for specific treatments, the exchange between silanols and siloxanes can occur also in mild conditions, with kinetics of evolution highly dependent by the type of silica and the external conditions applied. [111]

Surface functionalities, and in particular the distribution of the silanol families on the surface, have been considered lately as the most important feature able to interact with cellular membranes and provoke the MIE (molecular

initiating event) of the pathogenic pathway of silica particles in the lung, which is the membranolysis of the phagolysosome in the alveolar macrophage. [112, 113]
Recently, a strong paradigm between the presence of specific silanol distributions and the membranolytic activity of silica particles individuated the weekly interacting silanols, and in particular the nearly free silanols (NFS) as the critical molecular moiety able to interact with cellular membranes. NFS are characterized by an intersilanol distance of 4-6 Å, which appeared to be the optimal distance to interact with the phosphate groups of phospholipids which compose the cellular membranes. [109] Further insights about this topic will be discussed in Paragraph 1.4.

1.2.2.2 Surface radicals and ions.

When silica is subjected to mechanical stress, such as ball milling and fracturing in occupational and laboratory settings, an alteration of the bulk and the surface of the particle occurs. A crystalline particle, when it is subjected to mechanical fracturing, undergoes the breakage of the crystals and of the covalent bonds between silicon and oxygen, characteristic of the silica bulk. When this happens, new surface features with a high reactive energy are generated, which can be considered defective sites. These surface features can be ions or radicals, and are normally defined as coordinatively unsaturated sites. As introduced in Paragraph 1.1.1, the nature of the bond between silicon and oxygen in SiO_2 is considered covalent with some deviations from the covalent behavior due to the polarity. [2, 114, 115] The dual nature of the bond can generate either radicals through an homolytic fracture or ions through an heterolytic fracture. In Figure 1.8 is reported the model of reaction.

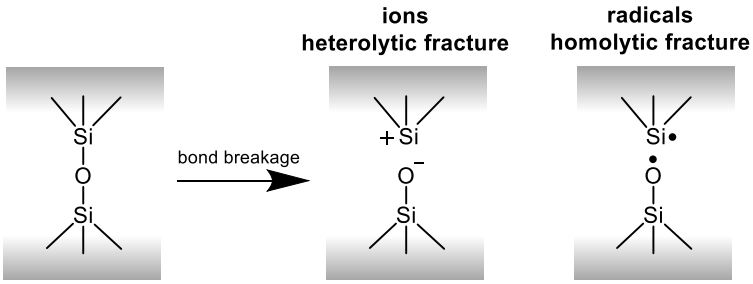

Figure 1.8: heterolytic and homolytic cleavage of the silicon-oxygen bond when quartz is subjected to mechanical pressure.

Several computational studies have been performed on the stability of ions and radicals and on which type of breakage is favored. The results are not concordant. According to cluster calculations, the charge separation

generated by the heterolytic breakage is less stable than the homolytic one. [116] Conversely, spin-polarized and spin-paired calculations described a difference in surface energy between the two types of active sites minor than 2%, because cluster calculations do not take into account intersite electrostatic interactions. [117-119] Thus, it is difficult to assess which kind of active site is favored, but it now established that the reactive energy of these sites is quite high, and that probably they react rapidly to recombine in more stable arrangements. This concept is called "surface reconstruction". For this reason, we cannot know which active sites are directly generated by the bond breakage, but it is easier to say which sites are more stable than the others. For instance, inert atmosphere can stabilize better radical species, while atmospheres rich in water vapor can stabilize better ionic species (though hydrogen bonding and electrostatic forces). [3]

Radical sites can be detected easily in several ways, such as photoluminescence and Electron Paramagnetic Resonance Spectroscopy (EPR).[120-123] Radicals in silica can be generated both by irradiation, [124, 125] and by mechanical fracturing. [123, 126, 127] Concerning mechanical fracturing, the most common radical species observed are the silyl radical (≡$Si^{\bullet}$), generated by the homolytic cleavage between silicon and oxygen, and peroxyl and superoxide radicals (≡$SiOO^{\bullet}$ and ≡$Si^{+}O_2^{-\bullet}$ respectively), which are in most of the cases generated by the reaction of surface sites with O_2 during fracturing. Curiously, the siloxyl radical (≡$SiO^{\bullet}$), which is directly generated together with the silyl radical by the breakage of the Si–O bond is not detectable though EPR, because of the too long relaxation time, which does not allow the detection. [123, 126, 128, 129] Radical species are not stable, and they recombine to produce neutral features, such as silanols and siloxanes. This decay is detectable through EPR spectroscopy and it is dependent on the external environment in which the silica sample is stored. However, radicals can be persistent. Traces of radical species on milled quartzes are detected also even months and years after milling, regardless of the environment in which they are stored. [126, 130]

The distribution of radical and ions can be tuned by the fracturing external environment and can influence also the subsequent reconstruction pattern of the surface of silica, in particular the silanol/siloxane ratio and their distributions.

1.2.2.3 Generation of reactive oxygen species (ROS)

Radicals, as examined in Paragraph 1.2.2.2, can be present either on the surface of the silica particle (or in the bulk) or can be generated as free radicals in aqueous medium, reacting with target molecules. [131]

Silica particles can produce reactive oxygen species (ROS) when suspended in a biological medium. ROS production is related to negative outcomes and inflammation in the cells, because they promote oxidation of the tissues and of cellular membranes. ROS production is correlated with active species produced by fracturing, because surface radical species when contacted with H_2O_2 are prone to generate $HO^{\bullet}$ radicals. [131, 132] Moreover, H_2O_2 can be generated by neutral peroxyl bridges (≡Si–O–O–Si≡), generated by structural defects, in contact with water. It was observed in several cases that freshly fractured quartzes were able to produce more ROS than aged ones, probably because of the decay of active sites on the surface (*e.g.*, recombination of radical species). [132-134]
ROS are also generated by transition metal contaminants, quite common in industrial silicas, such as iron (Fe^{2+}). In aqueous environment Fe^{2+} is oxidized to Fe^{3+} by generating $HO^{\bullet}$ (Fenton reaction) or $O_2^{\bullet-}$ and $HO_2^{\bullet-}$. Quartzes enriched in iron produced more ROS than the others [135, 136] However, in several cases the correlation between the amount of ROS generated and the cellular damage was not observed. This discrepancy excluded the ability to generate ROS as the feature able to trigger membranolysis. However, it is possible to hypothesize that ROS have a role inside the cell, while the membranolysis remains related to the silanol distribution (see Paragraph 1.2.2.1). This was also supported by Rubio and co-workers, who observed that the silanol content did not impact on intracellular level of ROS. [137]

1.2.2.4 Surface charge in liquid dispersions

As already anticipated in Paragraph 1.2.2.2, surface charges in silica may be originated by the heterolytic mechanical fracturing of the Si–O bond (Figure 1.8), but also, by deprotonation of silanol groups when the particle is suspended in a liquid medium. [138]
Silanols are in fact considered weak monoprotic Brønsted acids and, according to the pH in which the particles are dispersed, they can be charged or neutrals, following the equilibrium:

$$-SiO^- + H_2O \rightleftarrows -\mathrm{SiOH} + \mathrm{OH}^-$$

This means that in a basic environment the silanols are for the most part dissociated, in the form of silanolates (≡SiO^-), while at acidic pH silanols are all protonated and neutrals (≡SiOH).
When silica is suspended in an aqueous environment, an electrical double layer is generated around the particle, according to the characteristics of the surface. The inner layer is formed directly on the surface and it is composed by species connected to the surface atoms through chemical interaction. The

external layer, instead, is composed by ions of the buffer medium, such as NaCl solution, PBS, HEPES connected by weak electrostatic forces. The nature and the strength of the forces is dependent on the type of buffer used. [139]
The difference of potential between the double electric layer and the medium in which the particle is dispersed is called zeta (ζ) potential, and it depends on the pH of the solution and its ionic strength. [140, 141]
The surface charge and the ζ potential are quite important parameters when it comes to interaction between silica surface and biomembranes. Charges can change the protein corona adsorbed on the surface and can selectively interact with some endogenous proteins. [56, 142, 143]
Recently, Pavan and co-workers observed that titration of silanols using zeta potential can be useful for testing the silanol heterogeneity. However, they found that the membranolytic potential of the panel of quartzes analyzed did not parallel the ζ potential values and plot, so other parameters must be taken into account to determine the membranolytic potential of silica particles. [144]

1.3 Surface reconstruction of fractured silica surfaces.

Silicosis and other pathologies are normally related to crystalline silica particles of micrometric size inhaled in industrial settings. The crystalline paradigm for the explanation of silica toxicity was the most reliable among all the studies performed from the 60s, [145, 146] and was also adopted by IARC both in 1997 and in 2012. [48, 49] The theory was that only respirable crystalline particles (median size 4.5 μm of Ø) were able to cause silicosis and other adverse outcomes. Accordingly, no direct evidence of adverse pathological outcomes was observed for amorphous silica of any kind. This is the reason why IARC only included quartz and cristobalite in Group 1 as carcinogenic to human. However, this model cannot be applied on all the quartzes known. In fact, workers are exposed to micrometric quartz dusts mechanically grinded and fractured, and rarely respirable quartz not subjected to mechanical alteration was analyzed. Turci and co-workers proved that when a high purity quartz in respirable size and not subjected to mechanical fracturing was put in contact with red blood cells (RBC) and liposomes no membranolytic activity was observed. Similarly, the interaction between the same quartz and THP-1 macrophages did not elicit any cellular adverse effect. [98]
Specifically, a quartz crystal with intact surfaces was not able to trigger membranolysis and cell toxicity towards human macrophages. The same synthetic intact quartz, when subjected to mechanical fracturing (ball milling), became membranolytic and inflammogenic. This led to the conclusion that

crystallinity is a necessary but not sufficient key property to trigger the pathogenic pathway of silica particles. In Figure 1.9 are reported electron micrographs of synthetic quartz before and after ball milling. The surfaces of quartz before milling are smooth (Figure 1.9, A and B) and the crystallinity is observed up until the outermost surface atomic layer. When the same quartz is fractured (Figure 1.9, C and D), the surfaces are more irregular, with loss of long-range order crystal planes and conchoidal fractures (some of them highlighted in white).

Surfaces of fractured quartz have quite different properties than intact quartz, both morphologically and chemically. The two major characteristics are the irregular conchoidal fractures [147] and an external quasi-amorphous layer, called Beilby layer, in which the long range order of the crystal planes is strongly perturbed. [148-150]

This morphological and crystallographic change is reflected also on the chemical features observed on the surface. This is the concept of surface reconstruction. In fact, when crystalline silica is fractured, the not-so-covalent Si–O bond is broken and several types of defective species are generated, such as ions and radicals, (Paragraph 1.2.2.2), neutral species, such as silanols, siloxanes and silanones (Figure 1.10A).

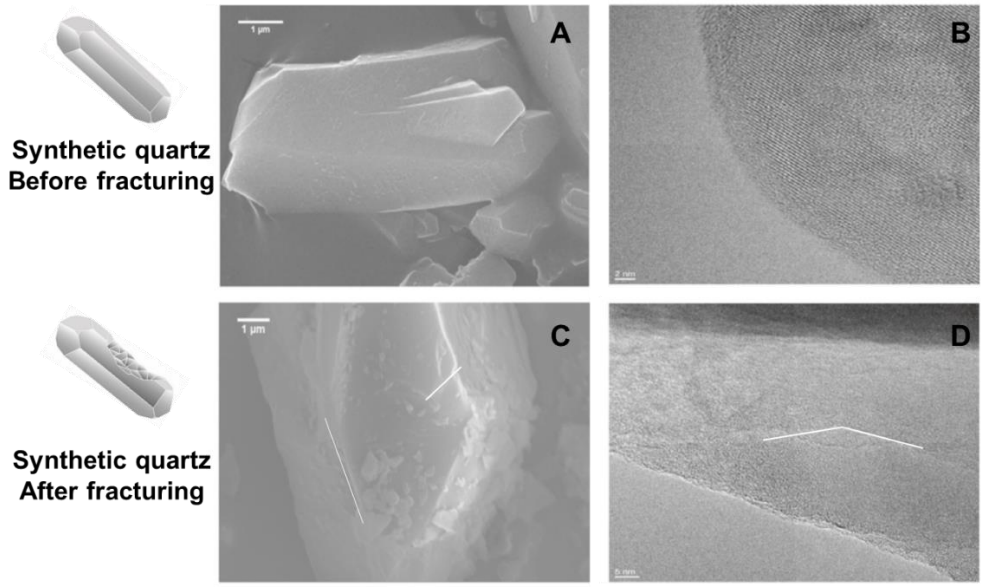

Figure 1.9: A synthetic quartz observed before fracturing with (A) Scanning Electron Microscopy (SEM) and (B) Transmission Electron Microscopy (TEM). The same quartz observed after fracturing with SEM and TEM (C and D respectively). Reproduced and adapted from [98].

These active sites, once exposed to the external environment for the first time are highly reactive [3, 105] and tend to recombine between each other in

more stable species or to react with the molecules present in the external environment, such as $H_2O_{(vap)}$, and O_2. This surface reconstruction leads an instable defective surface to a more stable one, mostly composed by neutral features, such as siloxanes and silanols.

For example, vicinal silyl and siloxyl sites (both radicals and ions) can reconstruct in several types of siloxanes, which can be classified in rings (MR, Figure 1.10B), according to how many silicon atoms compose the last ring exposed to the surface. [151] Normally, the structure of quartz is composed by 6-Membered Rings (see Paragraph 1.1.1.1), but when the surface is fractured the defects formed tend to reconstruct in a disordered way, because of their casual distributions. Membered Rings, their abundance and their alteration due to fracturing, can be detected experimentally through several techniques, such as Raman, IR spectroscopy and NMR. [89, 152-155] Also silanones (>Si=O) are unstable active sites and reconstruct in siloxanes, but they are normally quite rare to detect on silica, because of their lability. [3, 156, 157].

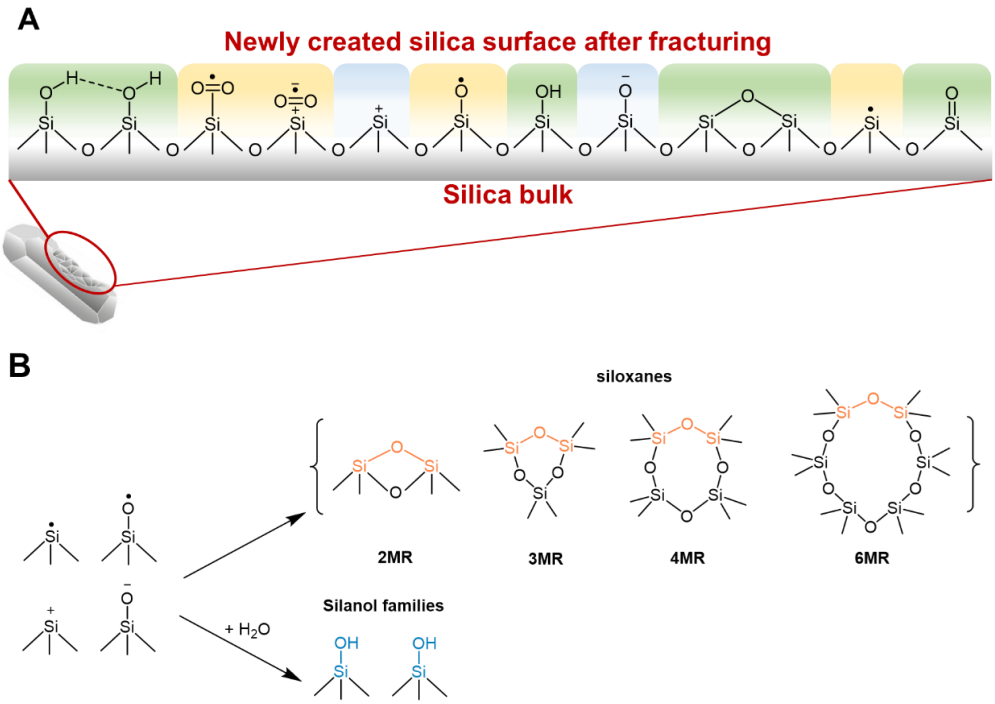

Figure 1.10: (A) heterogeneity of quartz surface after fracturing. (B) possible outcomes of the surface reconstruction of the most common surface-active sites generated on the surface after quartz fracturing.

The most important aspect of the surface reconstruction is the generation of silanol families. As shown in Figure 1.10B, silanols are generated by the reaction between the active sites with H_2O. Fractured silica is mostly

hydrophilic, and it tends to react with water molecules, in the vapor phase. Several computational studies concluded that the fractured surface reacts with water exothermically till the reaching of the full hydroxylation. Nevertheless, even if this reconstruction is favored, the kinetics of reaction can be variable. [158-160] Details of the reaction are reported in Figure 1.11. The reactions reported in Figure 1.11 show some of the possible pathways to obtain surface silanols from surface active sites. These reaction pathways are crucial for the surface reconstruction of silica surface because determinant for the distribution of surface silanols. Figure 1.11c details a particular pathway of formation of surface silanols. 3MRs are in fact unstable strained rings which tend to open and react with molecules in the external environment, forming specific arrangements of surface silanols. [18, 89]

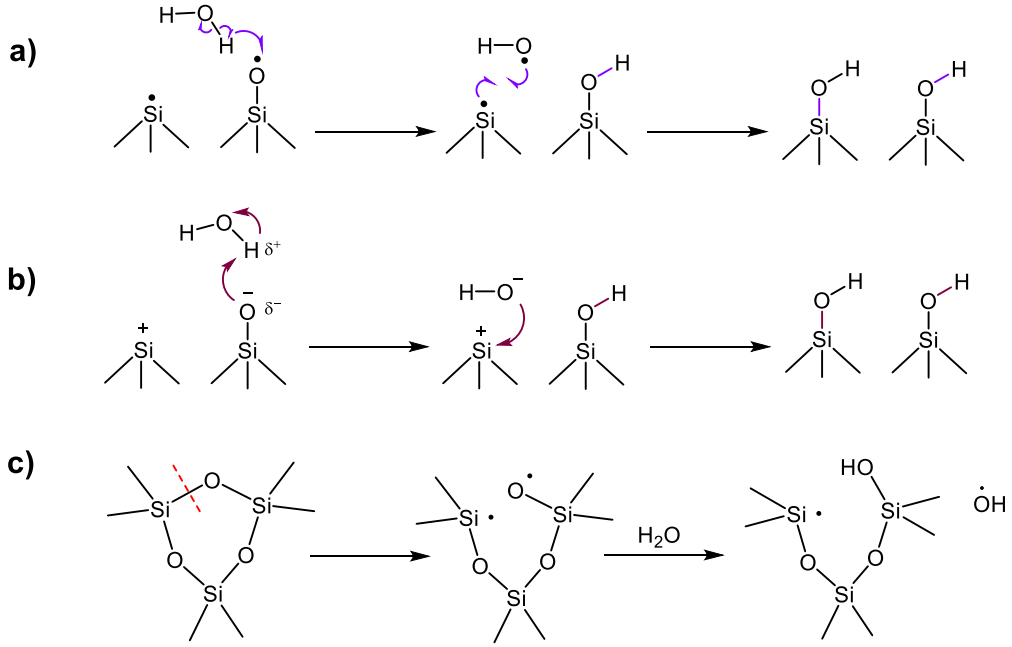

Figure 1.11: formation of surface silanols. (a) via radical pathway; (b) via ionic pathway; (c) via opening of strained rings in presence of water.

The distribution of geminal, vicinal, H-bonded, weakly interacting and isolated silanols (see Paragraph 1.2.2.1 and Figure 1.7) can vary according to two main factors.

The first is the mechanism of fracturing, while the second is the fracturing environment, and will be detailed in the following paragraphs.

1.3.1 Details of the mechanism of fracturing.

The fracturing of RCS, as already introduced in the previous chapters, is quite common in industrial settings, and it is considered the principal cause of all

the silicosis cases reported in literature. In the previous section was elucidated that quartz particles of micrometric size before fracturing, with their surfaces intact and smooth, are not able to trigger the membranolysis of several types of cells (Figure 1.9). [98]
As a result, the real reason for the membranolysis is the disorder generated on the surface after the fracturing, and the surface reconstruction that occurs during and immediately after milling to stabilize the active sites on the surface into more stable features.
Fracturing is a process of size reduction which can be reproduced also in a laboratory scale. Quartz lattice does not possess preferential cleavage planes. The breakage causes curving fractured surfaces typical of an amorphous material, called conchoidal fractures. In these fractures, the crystallographic order is lost, and they are covered by an amorphous layer (Beilby layer).
Several types of fracturing mechanisms exist, related to the different types of milling machines. The most common in the laboratory settings, which are able to comminute the size of the silica particles in the respirable range, are the planetary ball mill and the vibratory ball mill. (Figure 1.12A)

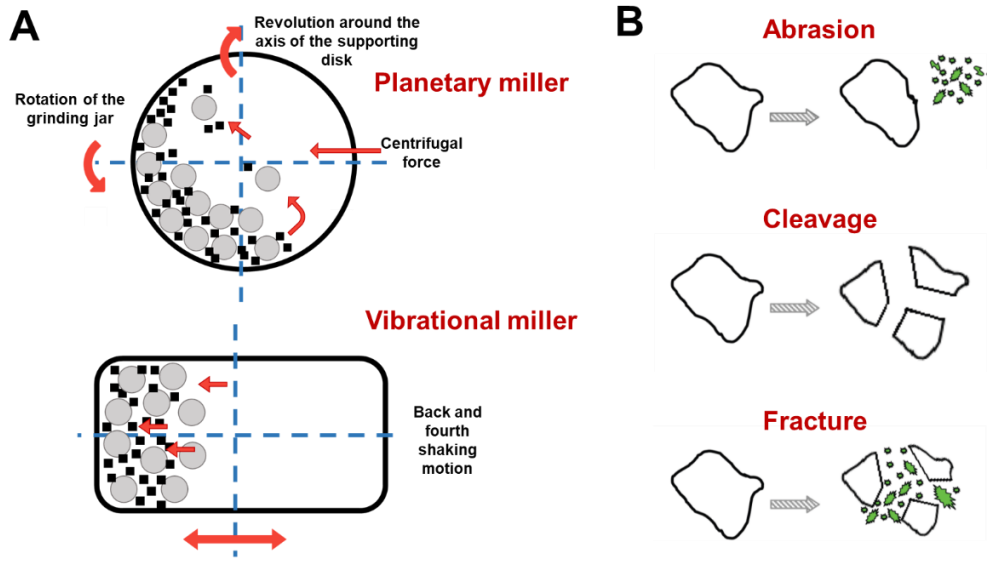

Figure 1.12: (A) Two types of ball mill commonly used in laboratory scale. Grey balls are the milling balls. Black dots are the particles of the milled material. Red arrows represent the principal milling movements observed. (B) principal mechanisms of the particle rupture. In green very small pieces of the same material. Reproduced from [161].

In both cases, the material before comminution is closed inside a vial called milling jar. Inside the milling jar, and together with the material, are present some spheres of different sizes called milling balls (in grey, Figure 1.12A). The

kinetic energy is transmitted to the mill body and then transferred to the grinding medium (jars and milling balls) and from them to the material. [161] The planetary mill is characterized by the typical orbital revolution of the jars containing the milling balls and the material. A strong part of their mechanism of action is the friction between the material and the milling balls. Two movements at the same time are executed, around the axis of the mill and around themselves (revolution and rotation). This gives rise to a complex centrifugal force which is able to mitigate the friction stress which is very high in this set up. The vibratory ball mill, on the other hand, is characterized by the same jar arrangement, but instead of rotating, it swings back and forth very quickly. This is a mill characterized by an impact-like fracturing more than a friction-like fracturing, and the energy applied is proportional to the amplitude of vibration and to the vibration frequencies.

Mathematical models [162-164] concluded that the most energetic between the two is by far the planetary ball mill, but it is important to say that it was also calculated that a big part of the energy applied (around the 80%) is wasted in heat. [165] The details about the milling set up will be further explored in Chapter 2.

Silica in laboratory settings is usually fractured in these two mills. A vibrational mill is characterized by the cleavage of the particles (Figure 1.12B) because of the impact-like fracturing, while the planetary ball mill is mostly characterized by the fracturing of the particle, which is the combination of cleavage and abrasion, with both the creation of very small particles (in green) alongside with bigger particles (in white). Obviously, the action is not exclusive, and every type of mill does a combination of the three, depending on the operating conditions and the type of material being ground. [166]

Another factor that influences the fracturing of silica, apart from the milling movements, which affect the predominant type of breakage (Figure 1.12B), is the temperature of milling. During the milling operation, heat is generated, and the temperature may influence the milling result, because it can induce phase transformations of the material. This is proportional with the energy of milling, the properties of the milled material and the milling media. [167] During the collisions, the material is subjected to microscopic temperature pulses from 50 to 500°C higher than the overall temperature inside the jar. These local peaks of temperature can induce transformation on the material phase (amorphization) and in the material surface (dehydration), effects quite peculiar of this type of mechanochemistry. [168, 169] The last but not the least important condition to take into account concerning the milling process is the environment. In fact, gases present in the milling environment during and immediately after fracturing are crucial in controlling the generation of different active sites (see Paragraph 1.2.2.2). For example, dry

environments, such as vacuum, argon or helium, can stabilize better dehydroxylated / radical-rich surfaces, while water-rich environments stabilize ion-rich surfaces and extended patterns of surface silanols. This means that by varying the milling environment it is possible to vary the surface reconstruction of silica particles, favoring the stability of some features at the expense of others.
Considering the variability of the quartz hazard, observed in the past decades [77, 95, 97], it can be assumed that the generation and the stabilization of the species in the process of surface reconstruction is crucial for the ability of quartz surface to interact with cellular membranes. Among all the surface features analyzed until now, recently nearly free silanols, a silanol family which falls under the weakly interaction silanols, was selected as the critical feature that, generated after fracturing, is able to trigger the membranolysis. (See Paragraph 1.2.2.1 and ref [109])

1.4 The role of nearly free silanols in the membranolytic activity of silica particles.

As introduced in Paragraph 1.3, after the generation of the active sites, these features can reconstruct either in siloxane bridges (≡Si–O–Si≡, generating different types of strained/unstrained rings) or in surface silanols (≡Si–OH). The heterogeneity of the surface generated after fracturing, however, does not naturally promote an ordered distribution of siloxanes and silanols. [170] Silanols, generally more reactive than siloxanes, because of their ability to engage hydrogen bonds, can in fact form different patterns, dependent on the structural disorganization, degree of hydration of the surface and intersilanol distances. [171, 172] Early studies proposed the role of silanols in the toxicity of silica, but the hypothesis was for long time not fully explored because other paradigms were investigated in the toxicity of quartz, such as crystallinity, metal impurities and generation of ROS. [173, 174] The interesting aspect is that the toxic activity is not related with the total silanol density, [137, 175] but to a specific silanol pattern able to damage biomembranes and trigger membranolysis. [95]
Recently, Pavan and co-workers identified a specific family of surface silanols, called nearly free silanols (NFS), to be the exact molecular moiety able to initiate the toxicity of silica particles, by triggering the membranolysis of the phagolysosomes in the alveolar macrophages. [109]
As shown in Figure 1.13A, when quartz is subjected to mechanical fracturing, undergoes a morphological alteration of the size and of the surface. The alteration provoked by fracturing is apparent in the measure of the

percentage of membranolytic activity. Quartz before fracturing is not membranolytic, while the same quartz after fracturing is highly membranolytic. In the study, Pavan and co-workers challenged the hypothesis that the alteration of the membranolytic activity observed is related to the presence on the surface of fractured quartz of nearly free silanols (NFS).

Silanol families can be detected through infrared spectroscopy (IR), and they are distinguished by their intersilanol distances. The vibrations and the bending modes of the Si–OH group are influenced by the silanol surroundings. As a consequence, the vibrational band of isolated silanols is different than the ones of H-bonded silanols (Figure 1.13). As shown in Figure 1.13B, the presence of the nearly free silanol peak, which falls in the range of the weakly interacting silanols (indicated with the red band), is clearly absent in the surface silanol profile of non-milled quartz of synthetic origin, but it is visible when the same quartz is fractured (peak at 2758 cm^{-1}).

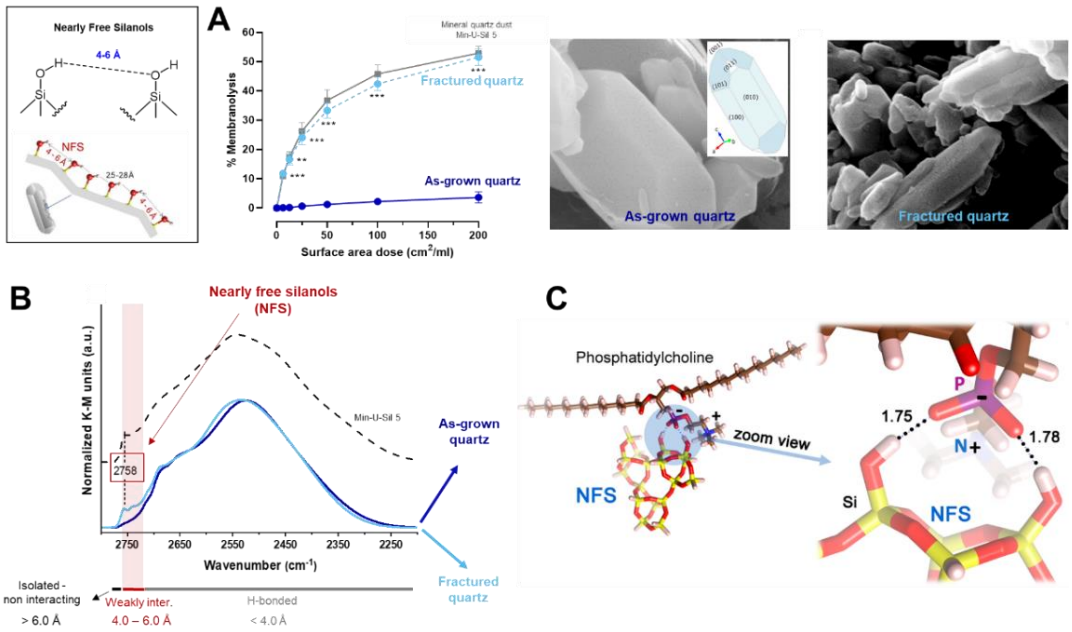

Figure 1.13: (A) different membranolytic activity of a quartz before and after fracturing and the relative morphology; (B) detection of NFS with IR spectroscopy; (C) cluster model of NFS interacting with phosphatidilcholine. Reproduced from [109]

This paradigm was validated both in high purity model quartz (*i.e.,* synthetic quartz), in industrial quartz and in amorphous silica, such as pyrolytic and vitreous silica. The presence of NFS in amorphous silica is related probably to their origin and to the degree of hydroxylation of their surfaces, but it is

strongly related to the disorder present on the surface, related to their natural disorder in the organization of the [SiO_4] units. However, amorphous silicas, even if rich in NFS, are characterized by a low bio persistence in the body, because they are generally more soluble than crystalline silica and they are cleared from the lung through dissolution and macrophage removal. [91, 176] They remain inflammatory *in vitro* and *in vivo*, but for a short period of time, not enough to initiate silicosis. [177, 178]

In Figure 1.13C, a computational study of the interaction between NFS and phosphatidylcholine show that NFS can interact with cellular membranes at a molecular level. In fact, as it is visible in the interaction with phosphatidylcholine, which is the major component of cellular membranes, NFS have the best geometry to interact with the phosphate group of the phosphatidylcholine head. Pavan and co-workers pointed out that "the same type of interaction could not occur with isolated silanols that can only make one single interaction, almost half as strong as that for the NFS pair. The clamping of the NFS may stiffen the membrane, making it more prone to breaking due to these coupling points, which would impair its natural flexibility". [109] This study validated the hypothesis that the toxicity of silica can be reconducted to the interaction of cellular membranes with a specific surface feature and highlights the importance of surface chemistry to elucidate molecular dynamics.

1.5 Objectives and outline of the work.

Even if the principal molecular mechanism that initiate silica toxicity has been elucidated, a number of open questions about the molecular dynamics of fractured RCS and their interaction with biomembranes is still unanswered. In this work, we shed light on some key aspects about the transformations and interaction of crystalline silica induced during and after mechanical fracturing.
The three questions that we challenged are graphically summarized in Figure 1.14.

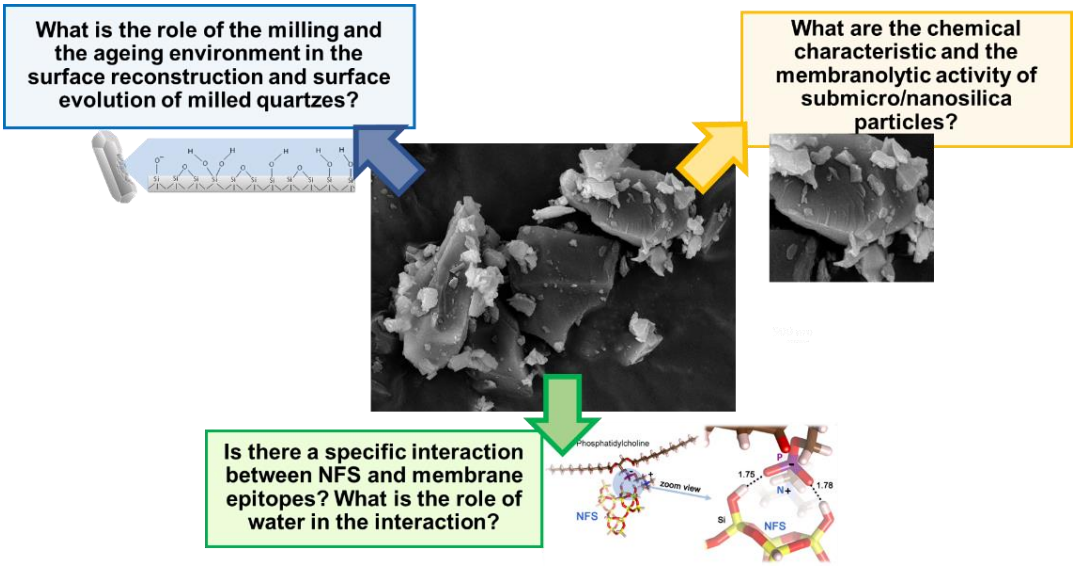

Figure 1.14: Objectives of the work.

To answer the above questions, we designed the following experimental approaches:

i. How does the milling environment modulate the surface reconstruction of quartz? As surface sites are responsible for the onset of surface reconstruction, we searched for a correlation between the different milling environments and the different potency of milled quartz to interact with biomembranes. We operated by ball milling highly pure model quartzes (of synthetic and mineral origin) in different external environments, and we analyzed whether the surface properties of the milled material were changed. We challenged the hypothesis that milling quartz in different molecular environments, by varying the concentration of O_2 and water vapor, can generate different active sites. The abundance and reactivity of

active sites during and immediately after fracturing was analyzed by solid state EPR spectroscopy which has been extensively used in the past to characterize the radical species that are formed on quartz upon milling. After milling, the reactivity of the surface towards model cell membranes (red blood cells) was investigated to check the membranolytic potential of the ball milled particles. Furthermore, milled quartzes were exposed to different ageing environments, composed by different amount of O_2 and water vapor, to check the possible alteration of membranolytic activity occurring up to one year after ball milling. At the best of our knowledge, this work represents the first attempt to systematically investigate how the variation of the environment during and after fracturing can alter the reactivity of quartz surface. The results obtained represent an advance in the still controversial generation of the molecular moieties that are responsible for crystalline silica detrimental interaction with biological molecules and membranes.

ii. What are the physicochemical characteristic and the toxicological impact of the nanometric fraction of fractured quartz? As mentioned in Paragraph 1.2.1.2, during the fracturing process, the reduction of the size of the particles is not homogeneous, and often a nanometric fraction of particles is generated and detected by electron microscopies. These particles usually strongly adhere on the surface of micrometric ones. The chemical characteristics and the toxicological impact of this nanofraction is unknown. With the aim of assessing a feasible route in the study of a nanofractured quartz, a top-down approach was optimized by ball milling of a synthetic quartz down to a nanometric size. Nanometric quartz samples were characterized by bulk techniques, and their disaggregation behavior in liquid suspensions and toward membranes was assessed. This study provided a new feasible route for the top-down preparation of nanometric quartz in short time and in good amount, and allows us to define, for the first time, the physicochemical properties of a nanometric quartz particle with properties comparable with the nanometric fraction of an industrial quartz dust.

iii. The interaction between nearly free silanols and biomembranes is specific? What is the role of water, ubiquitous in the body, in this interaction? Nearly free silanols have been acknowledged as the critical molecular moiety able to interact with molecular membranes and to initiate membranolysis. Nevertheless, the details of this interaction are still under investigation. In this part of the work, we challenged the hypothesis that the NFS-biomembrane interaction is

specific and occurs between NFS and certain membrane epitopes. Hence, we investigated the interaction between silica particles, both crystalline and amorphous, and phospholipids vesicles abundant in the lung environment and principal components of cellular membranes. At the best of our knowledge, this is the first work in which the different interactions of phospholipid vesicles were related with the presence of NFS on silica surface. A second aspect of this part of the work was the investigation of the role of interfacial water in the interaction between silica particles and biomembranes. We challenged here the hypothesis that water can play a role in the specific interaction between NFS and the phospholipid heads of biomembranes. Thus, the same silica particles and the phospholipids used for the first work were contacted in ultrapure water, and the behavior of interfacial water during the interaction analyzed with Sum-Frequency Generation Vibrational Spectroscopy. The aim was to establish a correlation between the behavior of water at the interface and the degree of the perturbation of the biomembrane during and after the interaction with the particle. This work represents the first attempt of the investigation of silica particle ad biomembranes by the interfacial water point of view.

1.6 Bibliography

1. McNaught, A.D. and A. Wilkinson, *Compendium of chemical terminology*. Vol. 1669. 1997: Blackwell Science Oxford.
2. Harrison, W.A., *IS SILICON DIOXIDE COVALENT OR IONIC?**Research sponsored by NSF Grant DMR77-21384*, in *The Physics of SiO2 and its Interfaces*, S.T. Pantelides, Editor. 1978, Pergamon. p. 105-110.
3. Rimola, A., et al., *Silica surface features and their role in the adsorption of biomolecules: computational modeling and experiments.* Chemical reviews, 2013. **113**(6): p. 4216-4313.
4. Guthrie, G.D. and P.J. Heaney, *Mineralogical characteristics of silica polymorphs in relation to their biological activities.* Scandinavian Journal of Work, Environment & Health, 1995. **21**: p. 5-8.
5. Luo, S.-N., et al., *Examining crystallographic orientation dependence of hardness of silica stishovite.* Physica B: Condensed Matter, 2007. **399**(2): p. 138-142.
6. Keskar, N.R. and J.R. Chelikowsky, *Structural properties of nine silica polymorphs.* Physical Review B, 1992. **46**(1): p. 1.
7. Akhavan, A.C. *Overview of Silica Polymorphs. The Quartz Page.* 2014; Available from: http://www.quartzpage.de/gen_mod.html.
8. Warheit, D.B., et al., *Pulmonary bioassay studies with nanoscale and fine-quartz particles in rats: toxicity is not dependent upon particle size but on surface characteristics.* Toxicological sciences, 2007. **95**(1): p. 270-280.
9. Pastero, L., et al., *Synthesis of α-quartz with controlled properties for the investigation of the molecular determinants in silica toxicology.* Crystal Growth & Design, 2016. **16**(4): p. 2394-2403.
10. Higgins, J.B., *Silica zeolites and clathrasils*, in *Silica*. 2018, De Gruyter. p. 507-544.
11. Tosheva, L. and V.P. Valtchev, *Nanozeolites: synthesis, crystallization mechanism, and applications.* Chemistry of materials, 2005. **17**(10): p. 2494-2513.
12. Napierska, D., et al., *The nanosilica hazard: another variable entity.* Particle and fibre toxicology, 2010. **7**(1): p. 1-32.
13. Fort, M., *Robert S. Anderson, Suzanne P. Anderson, Geomorphology. The mechanics and chemistry of landscapes. Cambridge University Press, Cambridge, 2010.* Géomorphologie: relief, processus, environnement, 2011. **17**(4): p. 427-428.
14. Dolino, G., *The α-inc-β transitions of quartz: a century of research on displacive phase transitions.* Phase Transitions: A Multinational Journal, 1990. **21**(1): p. 59-72.

15. Th, D., et al., *Polymorphism in silica studied in the local density and generalized-gradient approximations.* Journal of Physics: Condensed Matter, 1999. **11**(19): p. 3833.
16. Johnson, S.E., et al., *The quartz α↔β phase transition: Does it drive damage and reaction in continental crust?* Earth and Planetary Science Letters, 2021. **553**: p. 116622.
17. Nesse, W.D., *Introduction to mineralogy*. 2012: Oxford Univ. Press.
18. Brinker, C.J., K.S. Butler, and S.H. Garofalini, *Are nearly free silanols a unifying structural determinant of silica particle toxicity?* Proceedings of the National Academy of Sciences, 2020. **117**(48): p. 30006-30008.
19. Perkins, D., *Mineralogy. Free texbook for College - Level mineralogy Courses*. Second edition ed.
20. Niosh, C., *Health effects of occupational exposure to respirable crystalline silica.* National Institute for Occupational Safety and Health (NIOSH), 2002. **129**.
21. Hoy, R.F. and D.C. Chambers, *Silica-related diseases in the modern world.* Allergy, 2020. **75**(11): p. 2805-2817.
22. (ISO), I.O.f.S., *Air quality—Particle size fractionation definitions for health-related sampling.*, in *ISO*
No. 7708:1995., I.O.f.S. (ISO), Editor. 1995, ISO: Geneva.
23. M., R.S.J., *Guidance Document on the Determination of Particle Size Distribution, Fibre Length and Diameter Distribution of Chemical Substances*, in *JRC23287*, E. EN, Editor. 2002, European Commission.
24. Donaldson, K. and A. Seaton, *A short history of the toxicology of inhaled particles.* Particle and fibre toxicology, 2012. **9**(1): p. 1-12.
25. Leung, C.C., I.T.S. Yu, and W. Chen, *Silicosis.* The Lancet, 2012. **379**(9830): p. 2008-2018.
26. Rosen, G., *The history of miners' diseases: a medical and social interpretation*. 1943: Schuman's.
27. Thomas, C.R. and T.R. Kelley, *A brief review of silicosis in the United States.* Environmental health insights, 2010. **4**: p. EHI. S4628.
28. Greenberg, M.I., J. Waksman, and J. Curtis, *Silicosis: a review.* Disease-a-month, 2007. **53**(8): p. 394-416.
29. Mossman, B.T. and A. Churg, *Mechanisms in the pathogenesis of asbestosis and silicosis.* American journal of respiratory and critical care medicine, 1998. **157**(5): p. 1666-1680.
30. *Global, regional, and national age-sex specific all-cause and cause-specific mortality for 240 causes of death, 1990-2013: a systematic analysis for the Global Burden of Disease Study 2013.* Lancet, 2015. **385**(9963): p. 117-71.

31. Wagner, G.R., *Asbestosis and silicosis.* The Lancet, 1997. **349**(9061): p. 1311-1315.
32. Mazurek, J.M. and M.D. Attfield, *Silicosis mortality among young adults in the United States, 1968–2004.* American journal of industrial medicine, 2008. **51**(8): p. 568-578.
33. Organization, W.H., *Hazard Prevention and control in the work environment -- airborne dust*, in *WHO, WHO/SDE/OEH/99.14*. 1999: Geneva.
34. Steenland, K. and E. Ward, *Silica: a lung carcinogen.* CA: a cancer journal for clinicians, 2014. **64**(1): p. 63-69.
35. Nouh, M.S., *Is the Desert Lung Syndrome (Nonoccupational Dust Pneumoconiosis) a Variant of Pulmonary Alveolar Microlithiasis?* Respiration, 1989. **55**(2): p. 122-126.
36. Griffin, D.W., *Atmospheric movement of microorganisms in clouds of desert dust and implications for human health.* Clinical microbiology reviews, 2007. **20**(3): p. 459-477.
37. *Diseases associated with exposure to silica and nonfibrous silicate minerals. Silicosis and Silicate Disease Committee.* Arch Pathol Lab Med, 1988. **112**(7): p. 673-720.
38. Cohen, R.A., A. Patel, and F.H. Green. *Lung disease caused by exposure to coal mine and silica dust*. in *Seminars in respiratory and critical care medicine*. 2008. © Thieme Medical Publishers.
39. Pérez-Alonso, A., et al., *Outbreak of silicosis in Spanish quartz conglomerate workers.* Int J Occup Environ Health, 2014. **20**(1): p. 26-32.
40. Kramer, M.R., et al., *Artificial stone silicosis: disease resurgence among artificial stone workers.* Chest, 2012. **142**(2): p. 419-424.
41. Tustin, A.W., et al., *An outbreak of work-related asthma and silicosis at a US countertop manufacturing and fabrication facility.* American Journal of Industrial Medicine, 2022. **65**(1): p. 12-19.
42. Krefft, S., J. Wolff, and C. Rose, *Silicosis: an update and guide for clinicians.* Clinics in Chest Medicine, 2020. **41**(4): p. 709-722.
43. Leso, V., et al., *Artificial stone associated silicosis: a systematic review.* International journal of environmental research and public health, 2019. **16**(4): p. 568.
44. Hoy, R.F., et al., *Current global perspectives on silicosis—Convergence of old and newly emergent hazards.* Respirology, 2022.
45. Vida, S., et al., *Occupational Exposure to Silica and Lung Cancer: Pooled Analysis of Two Case-Control Studies in Montreal, CanadaOccupational Exposure to Silica and Lung Cancer.* Cancer epidemiology, biomarkers & prevention, 2010. **19**(6): p. 1602-1611.

46. Pelucchi, C., et al., *Occupational silica exposure and lung cancer risk: a review of epidemiological studies 1996–2005.* Annals of Oncology, 2006. **17**(7): p. 1039-1050.
47. Pairon, J., et al., *Silica and lung cancer: a controversial issue.* European Respiratory Journal, 1991. **4**(6): p. 730-744.
48. IARC, *Silica dust, crystalline, in the form of quartz or cristobalite*, in *Arsenic, Metals, Fibres and Dusts*. 2012, International Agency for Research on Cancer.
49. IARC, *Silica, some silicates, coal dust and para-aramid fibrils*. Vol. 68. 1997: World Health Organization.
50. Shtraichman, O., et al., *Outbreak of autoimmune disease in silicosis linked to artificial stone.* Occupational medicine, 2015. **65**(6): p. 444-450.
51. Parks, C.G., K. Conrad, and G.S. Cooper, *Occupational exposure to crystalline silica and autoimmune disease.* Environmental health perspectives, 1999. **107**(suppl 5): p. 793-802.
52. Steenland, K. and D.F. Goldsmith, *Silica exposure and autoimmune diseases.* American journal of industrial medicine, 1995. **28**(5): p. 603-608.
53. Iannello, S., et al., *Rheumatoid syndrome associated with lung interstitial disorder in a dental technician exposed to ceramic silica dust. A case report and critical literature review.* Clinical rheumatology, 2002. **21**(1): p. 76-81.
54. Dagenais, M., A. Skeldon, and M. Saleh, *The inflammasome: in memory of Dr. Jurg Tschopp.* Cell Death & Differentiation, 2012. **19**(1): p. 5-12.
55. Martinon, F., A. Mayor, and J. Tschopp, *The inflammasomes: guardians of the body.* Annual review of immunology, 2009. **27**: p. 229-265.
56. Lundqvist, M., et al., *Nanoparticle size and surface properties determine the protein corona with possible implications for biological impacts.* Proceedings of the National Academy of Sciences, 2008. **105**(38): p. 14265-14270.
57. Monopoli, M.P., et al., *Physical− chemical aspects of protein corona: relevance to in vitro and in vivo biological impacts of nanoparticles.* Journal of the American Chemical Society, 2011. **133**(8): p. 2525-2534.
58. Gun'Ko, V.M., et al., *Competitive adsorption of macromolecules and real-time dynamics of Vroman-like effects.* Physical Chemistry Chemical Physics, 2011. **13**(10): p. 4476-4485.
59. Casals, E., et al., *Time evolution of the nanoparticle protein corona.* ACS nano, 2010. **4**(7): p. 3623-3632.

60. Wang, F., et al., *The biomolecular corona is retained during nanoparticle uptake and protects the cells from the damage induced by cationic nanoparticles until degraded in the lysosomes.* Nanomedicine: Nanotechnology, Biology and Medicine, 2013. **9**(8): p. 1159-1168.
61. Pollard, K.M., *Silica, silicosis, and autoimmunity.* Frontiers in immunology, 2016. **7**: p. 97.
62. NADLER, S. and S. GOLDFISCHER, *The intracellular release of lysosomal contents in macrophages that have ingested silica.* Journal of Histochemistry & Cytochemistry, 1970. **18**(5): p. 368-371.
63. Leinardi, R., et al., *Cytotoxicity of fractured quartz on THP-1 human macrophages: role of the membranolytic activity of quartz and phagolysosome destabilization.* Archives of Toxicology, 2020. **94**(9): p. 2981-2995.
64. Kawasaki, H., *A mechanistic review of silica-induced inhalation toxicity.* Inhalation toxicology, 2015. **27**(8): p. 363-377.
65. Razzaque, M.S., et al., *Silica-induced inflammatory mediators and pulmonary fibrosis.* Fibrogenesis: Cellular and Molecular Basis, 2005: p. 199-210.
66. Castranova, V., *Signaling pathways controlling the production of inflammatory mediators in response to crystalline silica exposure: role of reactive oxygen/nitrogen species.* Free radical biology and medicine, 2004. **37**(7): p. 916-925.
67. Øvrevik, J., et al., *Activation of proinflammatory responses in cells of the airway mucosa by particulate matter: oxidant-and non-oxidant-mediated triggering mechanisms.* Biomolecules, 2015. **5**(3): p. 1399-1440.
68. Cassel, S.L., et al., *The Nalp3 inflammasome is essential for the development of silicosis.* Proceedings of the National Academy of Sciences, 2008. **105**(26): p. 9035-9040.
69. Mariathasan, S., et al., *Differential activation of the inflammasome by caspase-1 adaptors ASC and Ipaf.* Nature, 2004. **430**(6996): p. 213-218.
70. Gross, O., et al., *The inflammasome: an integrated view.* Immunological reviews, 2011. **243**(1): p. 136-151.
71. Dostert, C., et al., *Innate immune activation through Nalp3 inflammasome sensing of asbestos and silica.* Science, 2008. **320**(5876): p. 674-677.
72. Summerton, J., et al., *The mechanism of hemolysis by silica and its bearing on silicosis.* Experimental and Molecular Pathology, 1977. **26**(1): p. 113-128.

73. Oberdörster, G., C. Cox, and R. Gelein, *Intratracheal instillation versus intratracheal inhalation of tracer particles for measuring lung clearance function.* Experimental lung research, 1997. **23**(1): p. 17-34.
74. Hornung, V., et al., *Silica crystals and aluminum salts activate the NALP3 inflammasome through phagosomal destabilization.* Nature immunology, 2008. **9**(8): p. 847-856.
75. Iler, R.K. and R. Iler, *The chemistry of silica: solubility, polymerization, colloid and surface properties, and biochemistry.* 1979.
76. Driscoll, K.E., *The toxicology of crystalline silica studied in vitro.* Applied Occupational and Environmental Hygiene, 1995. **10**(12): p. 1118-1125.
77. Donaldson, K. and P.J. Borm, *The quartz hazard: a variable entity.* The Annals of occupational hygiene, 1998. **42**(5): p. 287-294.
78. Bruch, J., et al., *Variation of biological responses to different respirable quartz flours determined by a vector model.* International Journal of Hygiene and Environmental Health, 2004. **207**(3): p. 203-216.
79. Fubini, B., et al., *Relationship between the state of the surface of four commercial quartz flours and their biological activity in vitro and in vivo.* International Journal of Hygiene and Environmental Health, 2004. **207**(2): p. 89-104.
80. Cakmak, G.D., et al., *In vitro genotoxicity assessment of commercial quartz flours in comparison to standard DQ12 quartz.* International journal of hygiene and environmental health, 2004. **207**(2): p. 105-113.
81. Seiler, F., et al., *Different toxic, fibrogenic and mutagenic effects of four commercial quartz flours in the rat lung.* International journal of hygiene and environmental health, 2004. **207**(2): p. 115-124.
82. Cullen, R., et al., *Protection by iron against the toxic effects of quartz.* The Annals of Occupational Hygiene, 1997. **41**: p. 420-425.
83. Le Bouffant, L., H. Daniel, and J. Martin, *The therapeutic action of aluminium compounds on the development of experimental lesions produced by pure quartz or mixed dust.* Inhaled Particles, 1975. **4**: p. 389-401.
84. Begin, R., et al., *CT assessment of silicosis in exposed workers.* American Journal of Roentgenology, 1987. **148**(3): p. 509-514.
85. Martin, J.C., H. Daniel, and L. Le Bouffant, *Short-and long-term experimental study of the toxicity of coal-mine dust and of some of its constituents.* Inhaled particles, 1975. **4 Pt 1**: p. 361-371.
86. Vallyathan, V., et al., *Response of alveolar macrophages to in vitro exposure to freshly fractured versus aged silica dust: the ability of Prosil 28, an organosilane material, to coat silica and reduce its*

biological reactivity. Journal of Toxicology and Environmental Health, Part A Current Issues, 1991. **33**(3): p. 303-315.
87. Croissant, J.G., et al., *Synthetic amorphous silica nanoparticles: toxicity, biomedical and environmental implications.* Nature Reviews Materials, 2020. **5**(12): p. 886-909.
88. Di Cristo, L., et al., *Proinflammatory effects of pyrogenic and precipitated amorphous silica nanoparticles in innate immunity cells.* Toxicological Sciences, 2016. **150**(1): p. 40-53.
89. Zhang, H., et al., *Processing pathway dependence of amorphous silica nanoparticle toxicity: colloidal vs pyrolytic.* Journal of the American Chemical Society, 2012. **134**(38): p. 15790-15804.
90. Sandberg, W.J., et al., *Comparison of non-crystalline silica nanoparticles in IL-1β release from macrophages.* Particle and fibre toxicology, 2012. **9**(1): p. 1-13.
91. Arts, J.H., et al., *Five-day inhalation toxicity study of three types of synthetic amorphous silicas in Wistar rats and post-exposure evaluations for up to 3 months.* Food and chemical toxicology, 2007. **45**(10): p. 1856-1867.
92. Napierska, D., et al., *The nanosilica hazard: another variable entity.* Particle and fibre toxicology, 2010. **7**(1): p. 39.
93. Marques Da Silva, V., et al., *Pulmonary Toxicity of Silica Linked to Its Micro- or Nanometric Particle Size and Crystal Structure: A Review.* Nanomaterials, 2022. **12**(14): p. 2392.
94. Fubini, B., et al., *Physicochemical properties of crystalline silica dusts and their possible implication in various biological responses.* Scandinavian journal of work, environment & health, 1995: p. 9-14.
95. Pavan, C. and B. Fubini, *Unveiling the variability of "quartz hazard" in light of recent toxicological findings.* Chemical Research in Toxicology, 2017. **30**(1): p. 469-485.
96. Catalano, F., et al., *Effect of Silica Surface Properties on the Formation of Multilayer or Submonolayer Protein Hard Corona: Albumin Adsorption on Pyrolytic and Colloidal SiO2 Nanoparticles.* The Journal of Physical Chemistry C, 2015. **119**(47): p. 26493-26505.
97. FUBINI, B., *Surface Chemistery and Quartz Hazard.* The Annals of Occupational Hygiene, 1998. **42**(8): p. 521-530.
98. Turci, F., et al., *Revisiting the paradigm of silica pathogenicity with synthetic quartz crystals: the role of crystallinity and surface disorder.* Particle and Fibre Toxicology, 2016. **13**(1): p. 32.
99. Wiessner, J.H., et al., *Effect of particle size on quartz-induced hemolysis and on lung inflammation and fibrosis.* Experimental lung research, 1989. **15**(6): p. 801-812.

100. Rabolli, V., et al., *Influence of size, surface area and microporosity on the in vitro cytotoxic activity of amorphous silica nanoparticles in different cell types.* Nanotoxicology, 2010. **4**(3): p. 307-318.
101. Benesi, H.A. and B.H.C. Winquist, *Surface Acidity of Solid Catalysts*, in *Advances in Catalysis*, D.D. Eley, H. Pines, and P.B. Weisz, Editors. 1979, Academic Press. p. 97-182.
102. Davydov, V.Y., *Adsorption on silica surfaces.* SURFACTANT SCIENCE SERIES, 2000: p. 63-118.
103. Schuster, P., G. Zundel, and C. Sandorfy, *The hydrogen bond: recent developments in theory and experiments.* 1976.
104. Rimola, A., et al., *Does Silica Surface Catalyse Peptide Bond Formation? New Insights from First-Principles Calculations.* ChemPhysChem, 2006. **7**(1): p. 157-163.
105. Rimola, A. and P. Ugliengo, *A quantum mechanical study of the reactivity of (Si O) 2-defective silica surfaces.* The Journal of chemical physics, 2008. **128**(20): p. 204702.
106. Rimola, A., et al., *How Does Silica Catalyze the Amide Bond Formation under Dry Conditions? Role of Specific Surface Silanol Pairs.* ACS Catalysis, 2018. **8**(5): p. 4558-4568.
107. Kobayashi, T., J.A. DiVerdi, and G.E. Maciel, *Silica Gel Surface: Molecular Dynamics of Surface Silanols.* The Journal of Physical Chemistry C, 2008. **112**(11): p. 4315-4326.
108. El Samrout, O., et al., *Emergence of Order in Origin-of-Life Scenarios on Mineral Surfaces: Polyglycine Chains on Silica.* Langmuir, 2022. **38**(50): p. 15516-15525.
109. Pavan, C., et al., *Nearly free surface silanols are the critical molecular moieties that initiate the toxicity of silica particles.* Proceedings of the National Academy of Sciences, 2020. **117**(45): p. 27836-27846.
110. Maciel, G.E., *Probing Hydrogen Bonding and the Local Environment of Silanols on Silica Surfaces via Nuclear Spin Cross Polarization Dynamics.* Journal of the American Chemical Society, 1996. **118**(2): p. 401-406.
111. Bolis, V., et al., *Hydrophilic and hydrophobic sites on dehydrated crystalline and amorphous silicas.* Journal of the Chemical Society, Faraday Transactions, 1991. **87**(3): p. 497-505.
112. Pandurangi, R.S., et al., *Surface and bulk infrared modes of crystalline and amorphous silica particles: a study of the relation of surface structure to cytotoxicity of respirable silica.* Environmental Health Perspectives, 1990. **86**: p. 327-336.
113. Hemenway, D.R., et al., *What is the relationship between hemolytic potential and fibrogenicity of mineral dusts?* Archives of

Environmental Health: An International Journal, 1993. **48**(5): p. 343-347.
114. Murach, J. and R. Brückner, *Preparation and structure-sensitive investigations on silica glass fibers.* Journal of non-crystalline solids, 1997. **211**(3): p. 250-261.
115. Catlow, C. and A. Cormack, *Computer modelling of silicates.* International Reviews in Physical Chemistry, 1987. **6**(3): p. 227-250.
116. Murashov, V., *Ab initio cluster calculations of silica surface sites.* Journal of molecular structure, 2003. **650**(1-3): p. 141-157.
117. Murashov, V.V. and E. Demchuk, *Surface sites and unrelaxed surface energies of tetrahedral silica polymorphs and silicate.* Surface science, 2005. **595**(1-3): p. 6-19.
118. Murashov, V.V. and E. Demchuk, *A comparative study of unrelaxed surfaces on quartz and kaolinite, using the periodic density functional theory.* The Journal of Physical Chemistry B, 2005. **109**(21): p. 10835-10841.
119. Murashov, V.V., *Reconstruction of pristine and hydrolyzed quartz surfaces.* The Journal of Physical Chemistry B, 2005. **109**(9): p. 4144-4151.
120. Skuja, L., *The origin of the intrinsic 1.9 eV luminescence band in glassy SiO2.* Journal of Non-Crystalline Solids, 1994. **179**: p. 51-69.
121. Vaccaro, L., et al., *Luminescence of the surface nonbridging oxygen hole center in silica: Spectral and decay properties.* Physical review B, 2008. **78**(7): p. 075421.
122. Stapelbroek, M., et al., *Oxygen-associated trapped-hole centers in high-purity fused silicas.* Journal of Non-Crystalline Solids, 1979. **32**(1-3): p. 313-326.
123. Fubini, B., et al., *Mechanically induced defects in quartz and their impact on pathogenicity.* Solid State Ionics, 1989. **32**: p. 334-343.
124. Griscom, D., *Defects in amorphous insulators.* Journal of Non-Crystalline Solids, 1978. **31**(1-2): p. 241-266.
125. Griscom, D.L. and E.J. Friebele, *Fundamental defect centers in glass: $^{29}\mathrm{Si}$ hyperfine structure of the nonbridging oxygen hole center and the peroxy radical in a-Si${\mathrm{O}}_{2}$.* Physical Review B, 1981. **24**(8): p. 4896-4898.
126. Fubini, B., et al., *The formation of oxygen reactive radicals at the surface of the crushed quartz dusts as a possible cause of silica pathogenicity*, in *Effects of mineral dusts on cells*. 1989, Springer. p. 205-214.

127. Fukuchi, T., *A mechanism of the formation of E' and peroxy centers in natural deformed quartz.* Applied radiation and isotopes, 1996. **47**(11-12): p. 1509-1521.
128. Giordano, L., et al., *Optical and EPR properties of point defects at a crystalline silica surface: Ab initio embedded-cluster calculations.* Physical Review B, 2007. **75**(2): p. 024109.
129. Skuja, L., H. Hosono, and M. Hirano. *Laser-induced color centers in silica*. in *Laser-Induced Damage in Optical Materials: 2000*. 2001. SPIE.
130. Hasegawa, M., T. Ogata, and M. Sato, *Mechano-radicals produced from ground quartz and quartz glass.* Powder Technology, 1995. **85**(3): p. 269-274.
131. Fubini, B. and A. Hubbard, *Reactive oxygen species (ROS) and reactive nitrogen species (RNS) generation by silica in inflammation and fibrosis.* Free Radical Biology and Medicine, 2003. **34**(12): p. 1507-1516.
132. Shi, X., et al., *Generation of reactive oxygen species by quartz particles and its implication for cellular damage.* Applied Occupational and Environmental Hygiene, 1995. **10**(12): p. 1138-1144.
133. Castranova, V., *Generation of oxygen radicals and mechanisms of injury prevention.* Environmental health perspectives, 1994. **102**(suppl 10): p. 65-68.
134. Shi, X., N. Dalai, and V. Vallyathan, *ESR evidence for the hydroxyl radical formation in aqueous suspension of quartz particles and its possible significance to lipid peroxidation in silicosis.* Journal of toxicology and environmental health, 1988. **25**(2): p. 237-245.
135. Castranova, V., et al., *Augmentation of pulmonary reactions to quartz inhalation by trace amounts of iron-containing particles.* Environmental health perspectives, 1997. **105**(suppl 5): p. 1319-1324.
136. Fenoglio, I., et al., *The role of mechanochemistry in the pulmonary toxicity caused by particulate minerals.* Journal of Materials Synthesis and Processing, 2000. **8**: p. 145-153.
137. Rubio, L., et al., *Safer-by-design flame-sprayed silicon dioxide nanoparticles: the role of silanol content on ROS generation, surface activity and cytotoxicity.* Particle and fibre toxicology, 2019. **16**: p. 1-15.
138. Papirer, E., *Surface Charge and Zeta Potential: Silica in Mixtures and Water of Electrochemistry, Technical University of of Physical Chemistry, Abo Akademi*, in *Adsorption on Silica Surfaces*. 2000, CRC Press. p. 363-388.
139. Marucco, A., et al., *Possible chemical source of discrepancy between in vitro and in vivo tests in nanotoxicology caused by strong adsorption*

of buffer components. Chemical research in toxicology, 2015. **28**(1): p. 87-91.
140. Kumar, A. and C.K. Dixit, *Methods for characterization of nanoparticles*, in *Advances in nanomedicine for the delivery of therapeutic nucleic acids*. 2017, Elsevier. p. 43-58.
141. Lyklema, J., *Solid-Liquid Interfaces, Fundamentals of Interface and Colloid Science*. 1995, Academic Press, San Diego, CA.
142. Kozin, F., et al., *Silica-induced membranolysis: a study of different structural forms of crystalline and amorphous silica and the effects of protein adsorption.* Journal of Colloid and Interface Science, 1982. **88**(2): p. 326-337.
143. Braakhuis, H.M., et al., *Physicochemical characteristics of nanomaterials that affect pulmonary inflammation.* Particle and fibre toxicology, 2014. **11**(1): p. 1-25.
144. Pavan, C., et al., *Z potential evidences silanol heterogeneity induced by metal contaminants at the quartz surface: Implications in membrane damage.* Colloids and Surfaces B: Biointerfaces, 2017. **157**: p. 449-455.
145. Vigliani, E. and B. Pernis, *An immunological approach to silicosis.* Journal of Occupational and Environmental Medicine, 1959. **1**(6): p. 319-328.
146. Ziskind, M., R.N. Jones, and H. Weill, *Silicosis.* American review of respiratory disease, 1976. **113**(5): p. 643-665.
147. Margolis, S.V. and D.H. Krinsley, *Processes of formation and environmental occurrence of microfeatures on detrital quartz grains.* American Journal of Science, 1974. **274**(5): p. 449-464.
148. Finch, G.I., *The Beilby Layer on Non-Metals.* Nature, 1936. **138**(3502): p. 1010-1010.
149. Glasson, D.R., *Vacuum balance studies of milled material and mechanochemical reactions.* Thermochimica Acta, 1981. **51**(1): p. 45-52.
150. Jones, R.C. and G. Uehara, *Amorphous coatings on mineral surfaces.* Soil Science Society of America Journal, 1973. **37**(5): p. 792-798.
151. Ferrari, A.M., et al., *Reactions of silica strained rings: an experimental and ab-initio study.* Surface science, 1995. **323**(1-2): p. 151-162.
152. Brinker, C., et al., *NMR confirmation of strained "defects" in amorphous silica.* Journal of non-crystalline solids, 1988. **99**(2-3): p. 418-428.
153. Brinker, C.J., et al., *Surface structure and chemistry of high surface area silica gels.* Journal of Non-Crystalline Solids, 1990. **120**(1-3): p. 26-33.

154. Morrow, B. and I. Cody, *Infrared studies of reactions on oxide surfaces. 5. Lewis acid sites on dehydroxylated silica.* The Journal of Physical Chemistry, 1976. **80**(18): p. 1995-1998.
155. Boccuzzi, F., et al., *Infrared study of surface modes on silica.* The Journal of Physical Chemistry, 1978. **82**(11): p. 1298-1303.
156. Bobyshev, A. and V. Radtsig, *Silanone groups on the surface of mechanically activated silicon dioxide.* Kinet. Catal.(Engl. Transl.);(United States), 1988. **29**(3).
157. Kudo, T. and S. Nagase, *Theoretical study of silanone. Thermodynamic and kinetic stability.* The Journal of Physical Chemistry, 1984. **88**(13): p. 2833-2840.
158. Rignanese, G.-M., J.-C. Charlier, and X. Gonze, *First-principles molecular-dynamics investigation of the hydration mechanisms of the (0001) α-quartz surface.* Physical Chemistry Chemical Physics, 2004. **6**(8): p. 1920-1925.
159. de Leeuw, N.H., F.M. Higgins, and S.C. Parker, *Modeling the surface structure and stability of α-quartz.* The Journal of Physical Chemistry B, 1999. **103**(8): p. 1270-1277.
160. Rignanese, G.-M., et al., *First-principles molecular-dynamics study of the (0001) α− q u a r t z surface.* Physical Review B, 2000. **61**(19): p. 13250.
161. Gorrasi, G. and A. Sorrentino, *Mechanical milling as a technology to produce structural and functional bio-nanocomposites.* Green Chemistry, 2015. **17**(5): p. 2610-2625.
162. Mishra, B., *A review of computer simulation of tumbling mills by the discrete element method: Part II—Practical applications.* International Journal of Mineral Processing, 2003. **71**(1-4): p. 95-112.
163. Mishra, B., *A review of computer simulation of tumbling mills by the discrete element method: part I—contact mechanics.* International journal of mineral processing, 2003. **71**(1-4): p. 73-93.
164. Burmeister, C.F. and A. Kwade, *Process engineering with planetary ball mills.* Chemical Society Reviews, 2013. **42**(18): p. 7660-7667.
165. Avolio, R., et al., *A multitechnique approach to assess the effect of ball milling on cellulose.* Carbohydrate Polymers, 2012. **87**(1): p. 265-273.
166. Boldyrev, V.V. and K. Tkáčová, *Mechanochemistry of Solids: Past, Present, and Prospects.* Journal of Materials Synthesis and Processing, 2000. **8**(3): p. 121-132.
167. Mei, Q. and K. Lu, *Melting and superheating of crystalline solids: From bulk to nanocrystals.* Progress in Materials Science, 2007. **52**(8): p. 1175-1262.

168. Suryanarayana, C., *Mechanical alloying and milling.* Progress in materials science, 2001. **46**(1-2): p. 1-184.
169. Joardar, J., S. Pabi, and B. Murty, *Estimation of entrapped powder temperature during mechanical alloying.* Scripta Materialia, 2004. **50**(9): p. 1199-1202.
170. Dempster, P. and P. Ritchie, *Surface of finely-ground silica.* Nature, 1952. **169**(4300): p. 538-539.
171. Schrader, A.M., et al., *Surface chemical heterogeneity modulates silica surface hydration.* Proceedings of the National Academy of Sciences, 2018. **115**(12): p. 2890-2895.
172. Burneau, A. and J. Gallas, *Hydroxyl groups on silica surfaces*. 1998, Wiley New York. p. 145-312.
173. Nash, T., A. Allison, and J. Harington, *Physico-chemical properties of silica in relation to its toxicity.* Nature, 1966. **210**(5033): p. 259-261.
174. Nolan, R., et al., *Quartz hemolysis as related to its surface functionalities.* Environmental research, 1981. **26**(2): p. 503-520.
175. Pavan, C., et al., *In search of the chemical basis of the hemolytic potential of silicas.* Chemical research in toxicology, 2013. **26**(8): p. 1188-1198.
176. Roelofs, F. and W. Vogelsberger, *Dissolution kinetics of synthetic amorphous silica in biological-like media and its theoretical description.* The Journal of Physical Chemistry B, 2004. **108**(31): p. 11308-11316.
177. Sun, B., et al., *Reduction of acute inflammatory effects of fumed silica nanoparticles in the lung by adjusting silanol display through calcination and metal doping.* ACS nano, 2015. **9**(9): p. 9357-9372.
178. Ghiazza, M., et al., *Does vitreous silica contradict the toxicity of the crystalline silica paradigm?* Chemical research in toxicology, 2010. **23**(3): p. 620-629.

CHAPTER 2 - Ball milling optimization and tuning of the particle size of fractured quartz

2.1 Background.

As previously reported (see Introduction), the variability of silica toxicity can be related to a series of morphological and surface characteristics, which are modulated during the processing of mineral quartz and quartzite into commercial products.[1, 2] A determinant role is often played by comminution of quartz particles, which widens the variability of quartz features, because of the disorder induced by this process, both in term of surface characteristics and particle size. [3, 4] Tuning the comminution of quartz particles can be difficult, because it is important to control many factors: the particle size of the material before milling and the quantity to load inside the jar, [5] the diameter of the milling balls and their number, the material of the milling balls, [6, 7] the energy applied [8, 9] and the time of comminution [10]. Some of them are reported in Figure 2.1.

The categories of ball mill used for lab scale grinding processes are the planetary ball mill and the vibratory ball mill. The planetary mill is characterized by a friction-like fracturing, with only a small part of the size reduction of the material provoked by the neat impact of the milling balls with the material. The comminution derives from the abrasion of the material which is trapped between the milling balls and the walls of the jar because of the centrifugal movement. The vibratory mill follows the opposite principle, favoring an impact-like fracturing more than an abrasion type of comminution (Paragraph 1.3.1). [11, 12] Moreover, the material and the number/mass of milling balls are important because they are strictly correlated with the size of the loaded material inside the jar. Milling balls too big are unable to comminute small particles because the impacts are not effective, while balls

too small have an insufficient energy to comminute particles because of their low mass. [13-15]

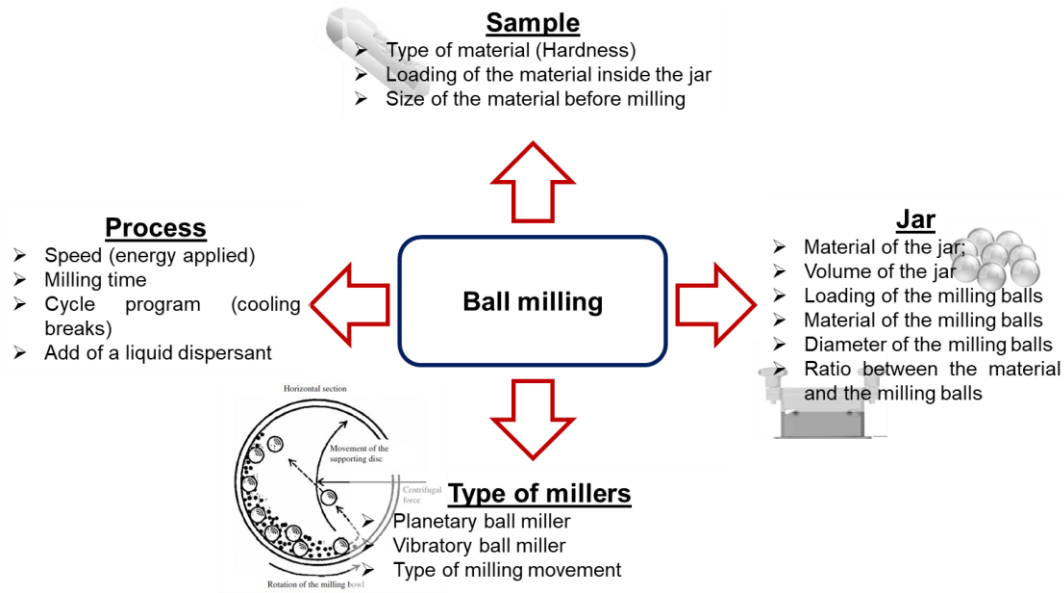

Figure 2.1: Summary of the parameters involved in the ball milling process.

Moreover, adding a liquid dispersant to the comminution process can have several advantages. The most important are: i. the avoidance of the caking of the material on the jar wall, cause of different distribution of the size and ii. the lowering of the thermal transfer from the milling ball to the material. [16, 17] This allows a finer and a more homogenous comminution, even though the comminution process follows a different reactive pathway.

The comminution usually provokes strain, stress and amorphization of the particles. Macroscopic crystallographic differences can be observed with X-Ray Powder Diffraction, and a quantitative analysis through the modeling of the diffractogram can be done to assess the alteration of the crystalline material and the generation of an amorphous phase.

In this section several milling procedures are described in order to obtain quartz in different size for different applications. The tuning of the milling conditions is crucial to obtain the desired size for the material. The result of the comminution was characterized by XRPD, EMs and BET. Quartzes characterized in this chapter will be used for different studies in the following chapters of this Thesis.

2.2 Materials and Methods.

2.2.1 Quartz particles

Crystalline silica particles involved in this study are both from a synthetic and mineral origin.

As-grown quartz crystals (gQ) were synthesized by hydrothermal synthesis following a procedure previously reported in literature with minor modifications.[18] A 25% (w/w) sodium metasilicate pentahydrate aqueous solution was polymerized through bubbling CO_2 until gel formation (pH ∼11) (acidifying agent H_2CO_3). Growth runs were performed in polytetrafluoroethylene liner sealed into steel autoclaves at 210 °C and autogenic pressure for 72h. The crystallinity of each synthetic lot was verified by X-ray powder diffraction (XRPD) analysis, and the morphology verified by Field Emission Scanning Electron Microscopy (FESEM) analysis.

Mineral quartz of natural origin and high purity (Madagascar quartz, mQ) was kindly provided by prof. Bice Fubini. The physicochemical properties of this particular quartz were already analyzed by the research group in previous papers.[19]

2.2.2 Ball milling

2.2.2.1 Micrometric comminution (Respirable size)

Two ball milling apparatuses were employed for the comminution of quartz down to a micrometric size.

1. Vibratory ball mill (MM200, Retsch) with agate jars (10ml), was loaded with 500 mg of gQ and two agate balls of Ø 7 mm, at 27 Hz for 6 hours. [20]
2. Planetary ball mill (Pulverisette 6, Fritsch) in ZrO_2 jars: 1.5g of micrometric quartz (gQ or mQ) were loaded in a ZrO_2 jar of 45 ml and 41g of ZrO_2 balls of 5 mm of diameter and ball milled for 1h at different milling energies (ranging from 150 rpm to 450 rpm) according to the desired size of the particles.

2.2.2.2 Nanometric comminution.

To perform a nanometric comminution, gQ was selected. A finely fractured quartz precursor (gQ-f3) was prepared from gQ (1.5 g) with a planetary ball mill (Pulverisette 6; Fritsch) in a ZrO_2 jar (45 ml) with 41 g of ZrO_2 balls (with a diameter of 5 mm), at 450 rpm for 1 hour and a pause of 1 minute every 20 minutes. gQ-f3 was then used as such for the preparation of the nanoquartz.

Nanoquartz samples (gQ-n1, gQ-n2 and gQ-n3) were obtained by milling gQ-f3 (1.5 g) in the same mill and jar described above. Smaller ZrO_2 balls (diameter = 2 mm, total mass = 41 g), and 12 ml of ultrapure water, filtered through a 0.22 µm filter, were used to obtain the nanoquartz. Milling parameters used to prepare nanoquartz are reported in Table 2.2. After milling, the quartz suspension was washed with water and dried overnight in an oven at 70 °C. After milling, gQ-n3 was sedimented for 24 hours. The supernatant containing the suspended particles was recovered and dried in the oven. [21]

2.2.3 XRPD analysis

Qualitative XRD diffractograms were recorded with a Rigaku Miniflex Diffractometer with a Cu-Kα radiation at 15 mA and 40 kV, a scan speed of 10 deg min^{-1} and a step width of 0.01 degrees.
Quantitative XRPD investigation was carried out on dry samples, using a PW3050/60 X'Pert Powder X-Ray Diffractometer (Malvern Panalytical, USA), in a spinner configuration to eliminate possible preferential orientation of the powder (1 rotation/s). Diffractograms were collected between 5°- 120° (2θ), using a Cu-Kα radiation at 45 kV and 40 mA, a step size of 0.015°, a time per step of 0.7 s, and a scan speed of 0.0106°/s. The Rietveld refinement of the measured diffraction patterns was performed with Materials Analysis Using Diffraction (MAUD) software. The instrumental function was determined using LaB_6 NIST standard (660b). [22, 23]

2.2.4 Analysis of the Specific Surface Area (SSA)

Specific Surface Area of quartz obtained after milling was evaluated by measuring Kr physisorption at −196 °C and applying the Brunauer, Emmett, and Teller (BET) method using ASAP 2020 apparatus (Micromeritics, Norcross, GA, USA). Before analysis, samples were outgassed at 150°C for 2h to remove physiosorbed molecules.

2.2.5 Morphology analysis

The morphology of quartz after mechanical stress was checked with Scanning Electron Microscopy: the analyses were performed with a Tescan S9000G FIB-FESEM/EBSD/TOF-SIMS, using the secondary electron (SE) and back scattered electron (BSE) detector. The emitting source was operated at accelerating voltage of 5 keV for high resolution imaging. EDS analysis (Energy Dispersive X-ray Spectroscopy) was generally performed on single particle or portions of the sample.

2.3 Results and discussion

2.3.1 Optimization of ball milling protocol for respirable size comminution

The quartz of synthetic origin (gQ), whose synthesis was already optimized and reported previously by our research group, was used to define the ball milling protocol that is required to obtain a quartz dust in respirable size range. Figure 2.2 reported about the morphology of the as-prepared synthetic gQ crystals. The SEM micrographs were taken at increasing magnification to representatively describe the morphology and the well-grown crystal faces of synthetic quartz crystals. In general, gQ is characterized by large crystals with flat and well-defined surfaces, that are formed by the termination of individual crystal planes. The size of the crystals is around 20-30 µm, and larger polycrystalline particles of hundreds of µm in size are often evidenced. [18, 20]

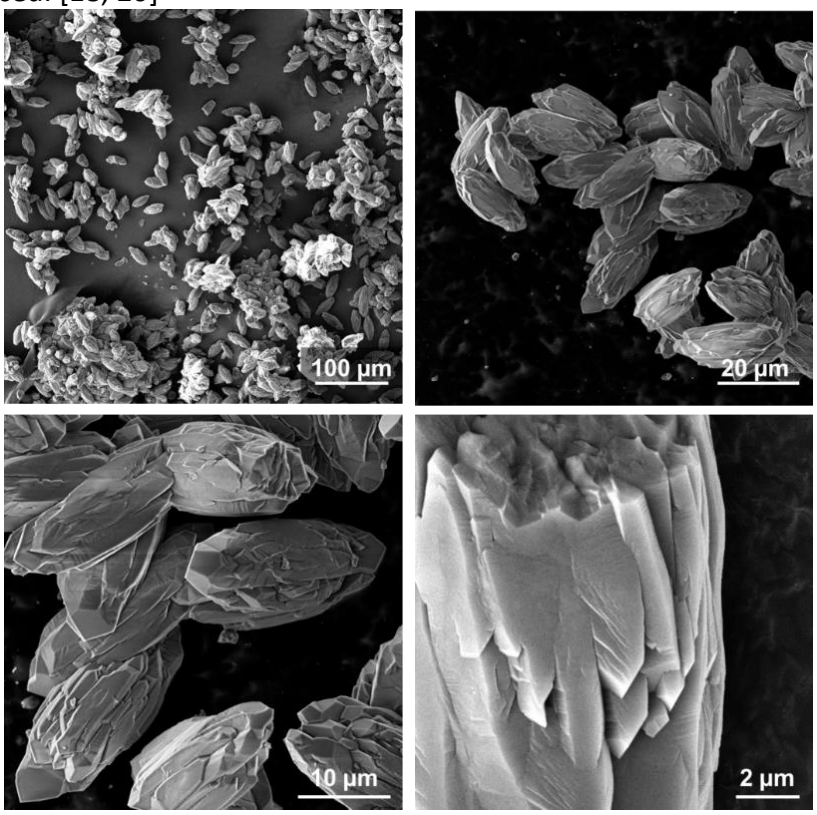

Figure 2.2: FE-SEM micrographs of gQ at different magnifications.

As gQ represents a well-grown quartz with large crystals, a ball milling process is a necessary step to conveniently reduce the size of the particles down to respirable size range and obtain a sample that can be significantly

uses in toxicological assessments of quartz. An optimized milling procedure used was already published by some of us and it is reported in Table 2.1 (line1).[19, 20]

In previous works, agate was chosen as the milling material because it avoids possible contamination of the material by foreign metal impurities. Agate is composed of the most part by SiO_2, and the presence of ions that might interfere with the properties of quartz should be negligible. However, one of the major downsides of the use of agate as milling material is its hardness. In fact, agate is a cryptocrystalline variety of quartz. For this reason, its hardness is reported to be around 6.5-7 on the Mohs hardness scale[25], and a density of 2.6 g/cm^3, similar to quartz [26]. In general, it is recommended to use a milling material harder than the milled material, to avoid contamination but also excessive abrasion and consumption of the milling balls and jar.

Table 2.1: summary of the milling conditions applied on synthetic quartz.

gQ	name	ball mill	material	time	speed	ball size (mm)	ball number (u) – weight (g)	jar size (mL)	load (g)	SSA (m^2/g)
1	gQ-f	vibratory	SiO_2 (agate)	6h	27 Hz	7	2 u – 0.9g	10	0.5	3.9
2	gQ-f1	planetary	ZrO_2	1h	150 rpm	5	~100 u - 41 g	45	1.5	1.3
3	gQ-f2	planetary	ZrO_2	1h	250 rpm	5	~100 u - 41 g	45	1.5	3.8
4	gQ-f3	planetary	ZrO_2	1h	450 rpm	5	~100 u - 41 g	45	1.5	10.7

Moreover, similar hardness between the two materials normally leads to a less efficient reduction of particle size. In fact, a lower energy is transferred to the material to be milled and the milling limit (*i.e.*, the size limit beyond which the reduction of the size obtained by a longer milling time is negligible) is higher. Previous agate milling protocol required in fact a six hour milling time to produce a considerable increase of Specific Surface Area (SSA) in quartz (Table 2.1, line1). This milling procedure produced particles with size around 4-6 µm, irregular surfaces and spikes and SSA of ca. 4 m^2/g. Conchoidal fractures are visible and are highlighted by arrows in Figure 2.3. As anticipated, these features are typical of quartz, related to its structure and chemical bonds, and are representative of the morphological disorder induced by ball milling on quartz. The relatively high SSA, together with the morphology, makes gQ-f a suitable proxy for a quartz dust of respirable size. However, the long milling time and the possible contamination by the milling jar prompted us to achieve an equivalent result with an optimized protocol.

The morphology of gQ-f once ball milled is checked by FESEM (Figure 2.3).

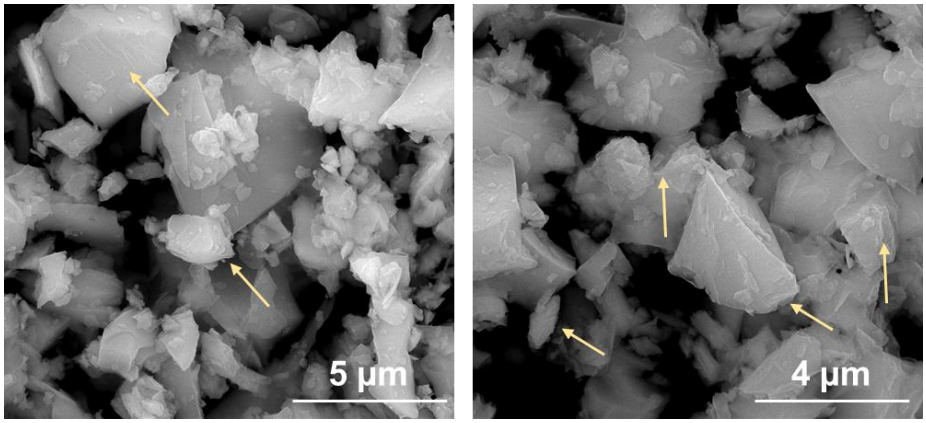

Figure 2.3: FESEM micrographs of gQ after milling 6 hours in the vibratory mill.

In order to do this, a new ball milling set up was chosen.
The comminution was carried out in a planetary mill with ZrO_2 jar and balls. The use of a planetary mill allowed to take advantage of a more energetic comminution mechanism. In fact, planetary ball mill has a specific mill power that ranges between 9000 to 36000 W/kg, which is higher than the 4500 W/kg that can be achieved with a vibratory ball mill. [11, 27] Moreover, the larger volume of the jar allowed us to increase the batch size and the load of milling balls. The diameter of the milling balls was also decreased from 7 mm to 5 mm, while the number of the balls was increased (41g, that equals to ca. 100 ZrO_2 balls). Nonetheless, the density of ZrO_2 is 5.7 g/cm^3, almost three time higher than SiO_2 and the energetic of the quartz-ball impacts is increased, despite the lower ball volume. The energetic of the impact is increased also because of the major hardness of ZrO_2 with respect of agate (8 on the Mohs scale, 1200 (HV) on the Vickers scale). The higher energies due to the planetary motion and to the higher density and hardness of ZrO_2 and the higher number of collisions generated by the larger amount of balls per unit mass of quartz produced a higher fragmentation of the quartz crystals per time unit. With this in mind, the new of the milling protocol in this new set up was optimized (Table 2.1, lines 2-3-4).
In the optimization attempts performed in the planetary ball mill set up, all the parameters were kept the same except for the milling speed. The milling time was set up at one hour to significantly reduce the extent of the process. The results of the comminutions are reported in Figure 2.4.
SEM micrographs pointed out the change of morphology when the rotation speed increased. Synthetic quartz fractured at 150 rpm (here called gQ-f1) has a morphology characterized by particles of several micrometers, with some smaller particles. As in the gQ milled in the vibratory mill (Table 2.1, line 1), conchoidal fractures typical of crystalline silica when fractured are present. When milled at 250 rpm, gQ-f2 morphologically was very similar to

the previous one, but the decrease in size is highlighted from the measurement of the SSA (Table 2.1, line 2 and 3). While the gQ-f1 has a SSA of 1.3 m^2/g, the gQ-f2 is around 3.8 m^2/g, a SSA value compatible with a quartz of respirable size.

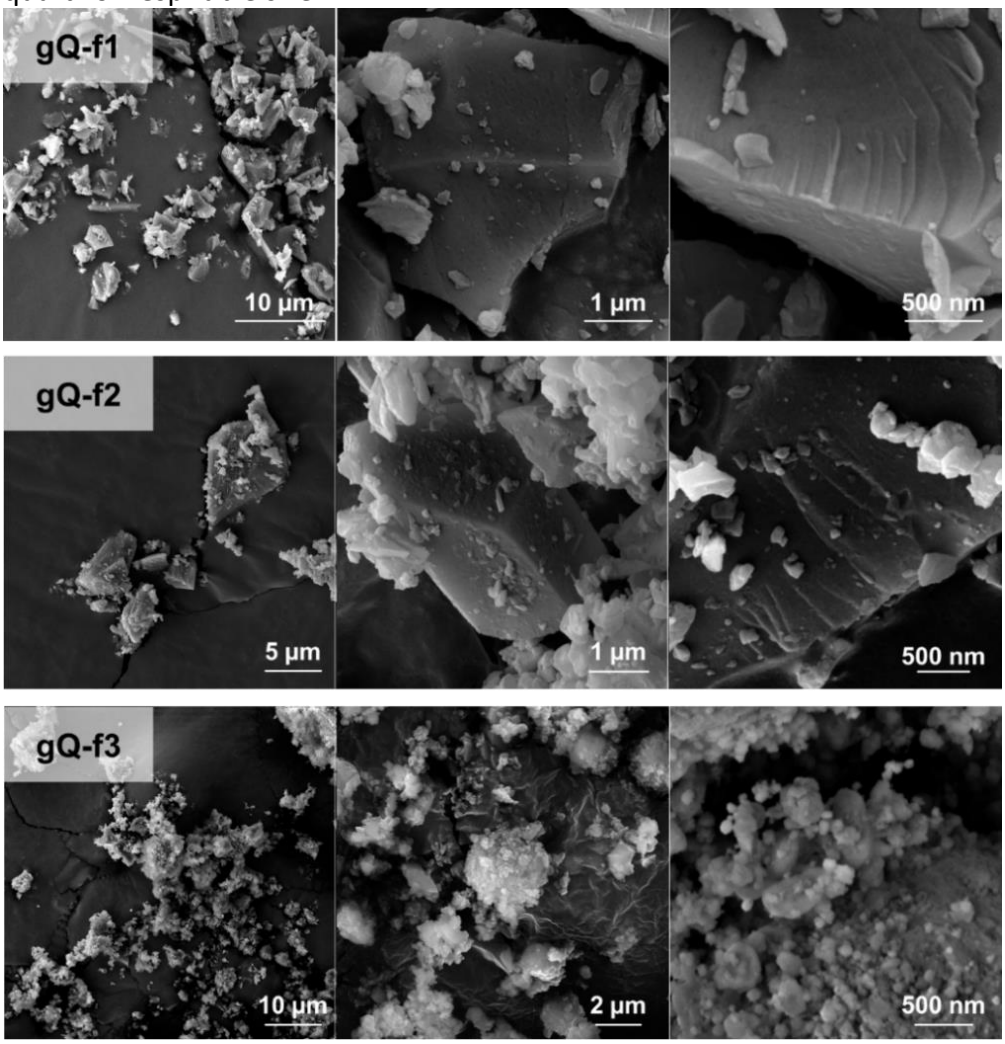

Figure 2.4: FESEM micrographs of gQ milled in a planetary ball mill in three different milling rotational speed at low and high magnification.

A drastic change in morphology was observed with gQ-f3 (milled for 1 hour at 450 rpm). The significant rise in rotational speed created a morphology less recognizable than the other two. In this sample there are some micrometric particles completely covered by a large amount of submicrometric and nanometric particles which are not recognizable with the usual crystalline features of quartz. Moreover, no conchoidal fractures are visible. It is quite difficult to say if the agglomerates of particles are one micrometric particle covered by nanometric ones or a full agglomerate of submicro / nanometric

particles. With this sample a considerable rise in SSA is attained (Table 2.1, line4), which locate this milled quartz above the normal respirable size ones, placing it in the submicrometric-nanometric range. In order to better characterize the newly milled samples, X-Ray Powder Diffraction (XRPD) was performed to examine the retention of quartz crystallinity. In Figure 2.5A are reported the diffractograms of the quartzes, showing no significant difference between the crystalline structure of the samples, at least for the gQ-f1 and gQ-f2. In the gQ-f3, a slight reduction of the crystallographic peaks was observed, phenomenon strongly related to the reduction of the size of the particles (Figure 2.5B). [28]

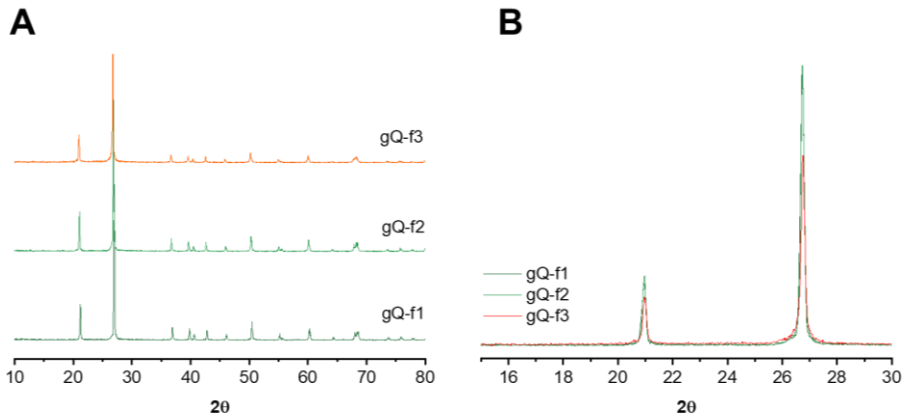

Figure 2.5: XRPD diffractograms of synthetic quartzes milled in a planetary ball mill. (A) 10-80° region diffractograms of the three milled quartzes (gQ-f1, gQ-f2 and gQ-f3). (B) magnification of the 15-30° region to highlight the height differences of the peaks between the gQ-f1 and gQ-f2 with respect of gQ-f3.

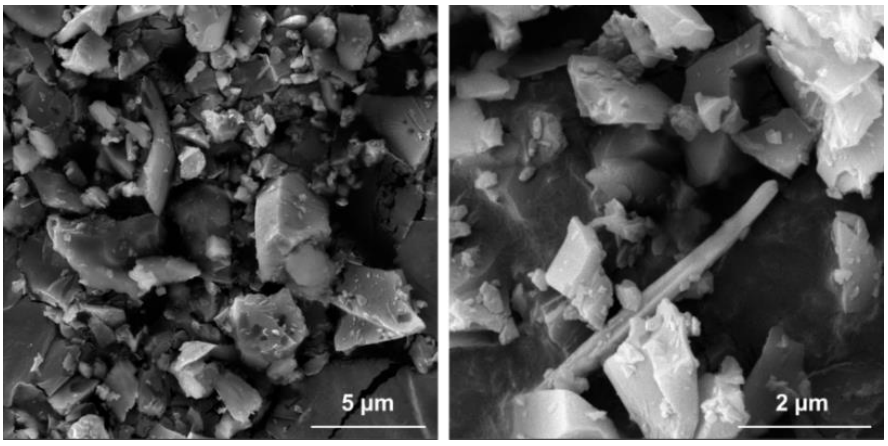

Figure 2.6: FESEM micrographs of a respirable quartz of industrial origin (Min-U-Sil5) used as reference for a fractured quartz of respirable size.

XRPD essentially confirmed the morphological evaluation made with SEM. Finally, the analysis of the SSA was the crucial parameter to choose between the gQ-f1 and f2. The gQ milled in vibratory mill, in fact, has a SSA of 3.9 m^2/g, which is comparable with the one of gQ-f2 (3.8 m^2/g) (Table 2.1, lines 1 and 3).
Fractured quartzes were compared to an industrial quartz of mineral origin and of respirable size used as reference (Min-u-sil5). In fact, Min-U-sil5 (Figure 2.6) show a morphology comparable with gQ-f1/f2, but the SSA of Min-u-sil5 is comparable with the gQ-f2 (4.1 m^2/g). For these reasons, gQ-f2 is the most valid candidate among the three samples milled with the planetary mill.

2.3.2 Application of the optimized protocol on highly pure mineral quartz (Madagascar quartz)

Highly pure mineral quartz (mQ) was subjected to a similar milling protocol. However, mQ crystals are of centimetric measure. Thus, to be reduced on a respirable size they need to be pre milled down to a uniform powder. The procedure is already reported in previous literature. [20, 29] This powder has a specific surface area of 0.3 m^2/g, compatible with the one of gQ, and can be subjected to the ball milling to obtain a respirable size quartz. The same protocol as gQ in the planetary ball mill was applied for mQ. (Table 2.1, line 3) Fractured mineral quartz, here called mQ-f, has a morphology similar to gQ-f2 and Min-U-Sil5 (Figure 2.4 and Figure 2.6, respectively) and the SSA value is 3.9 m^2/g, compatible with Min-u-sil5 used as industrial reference of a respirable crystalline silica particle.
Morphology of mQ is reported in Figure 2.7.

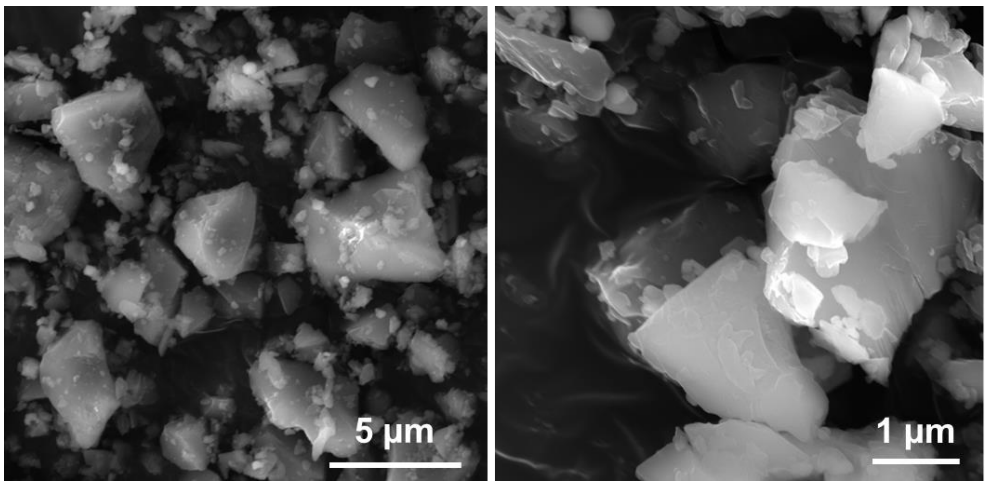

Figure 2.7: morphology check of mQ after fracturing down to a respirable size in the planetary ball mill.

2.3.3 *Optimization of the milling protocol to obtain quartz of nanometric size.*

In order to reduce the particle size of a synthetic quartz down to the nanometric size range, a different strategy was adopted. The use of the agate set up was excluded. In fact, as already said before, the hardness of agate is the same of quartz, and to conveniently reduce the particle size down to several nanometers a very long milling time should be required, considering that 6 hours are needed to obtain a respirable size and a SSA of 3-4 m^2/g.

Table 2.2: summary of the milling conditions for the obtainment of nanoquartz.

gQ		Milling step	time (h)	energy (rpm)	ball size (mm)	ball weight	jar size	load (g)	SSA (m^2/g)
1	**gQ-f3**	1st	1	450	5	41 g	45ml	1.5	10.7
2	**gQ-n1**	2nd	1	450 (wet)	2	41 g	45 ml	1.5	37
3	**gQ-n2**	2nd	1	550 (wet)	2	41 g	45 ml	1.5	45
4	**gQ-n3**	2nd	2	550 (wet)	2	41 g	45 ml	1.5	55

For this reason, the zirconia set up, together with the planetary ball mill, was selected and a two-step milling approach was adopted. Micrometric gQ crystals of synthetic origin (already described in Paragraph 2.3.1) were firstly milled for 1 h at 450 rpm, obtaining gQ-f3 (characterized in Paragraph 2.3.1). The sample (Table 2.2, line 1), which showed an SSA of 10 m^2/g and particles with irregular morphology and size, (Figure 2.4) wad used as the precursor material for the nanoquartz preparation.

A second milling step was applied to gQ-f3. In this case, the diameter of the milling balls was reduced, and a liquid dispersant was added. The reduction of the diameter of the milling balls from 5 mm to 2 mm was applied, but the total weight of the milling balls was maintained (Table 2.2). This means a higher number of balls and a higher number of hits. The reduction of the size of the balls in this case is coherent with the reduction of the size of the initial load of quartz, because gQ-f3 has a smaller particle size than gQ.

Regarding the liquid dispersant, useful to avoid the cacking of the material when very high energies are involved, water was selected, to minimize the alterations of the quartz surface properties and to avoid the etherification of the silanols (SiOH) that could occur when organic solvents, *e.g.*, methanol and ethanol, are used. [30] The wet step is consistent with industrial procedures used in conventional workplace applications (*i.e.,* wet cutting or polishing of quartz containing composites). This second wet-milling step induced a four-

to-six times increase in the SSA, with respect to gQ-f3 (Table 2.2). By increasing the rotational speed and the milling time the SSAs of the milled quartzes increased by up to 55 m^2/g in the following order: gQ-f3 < gQ-n1 < gQ-n2 < gQ-n3. Both the milling speed (gQ-n1 vs gQ-n2) and the milling time (gQ-n2 vs gQ-n3) strongly affected the efficiency of the comminution.

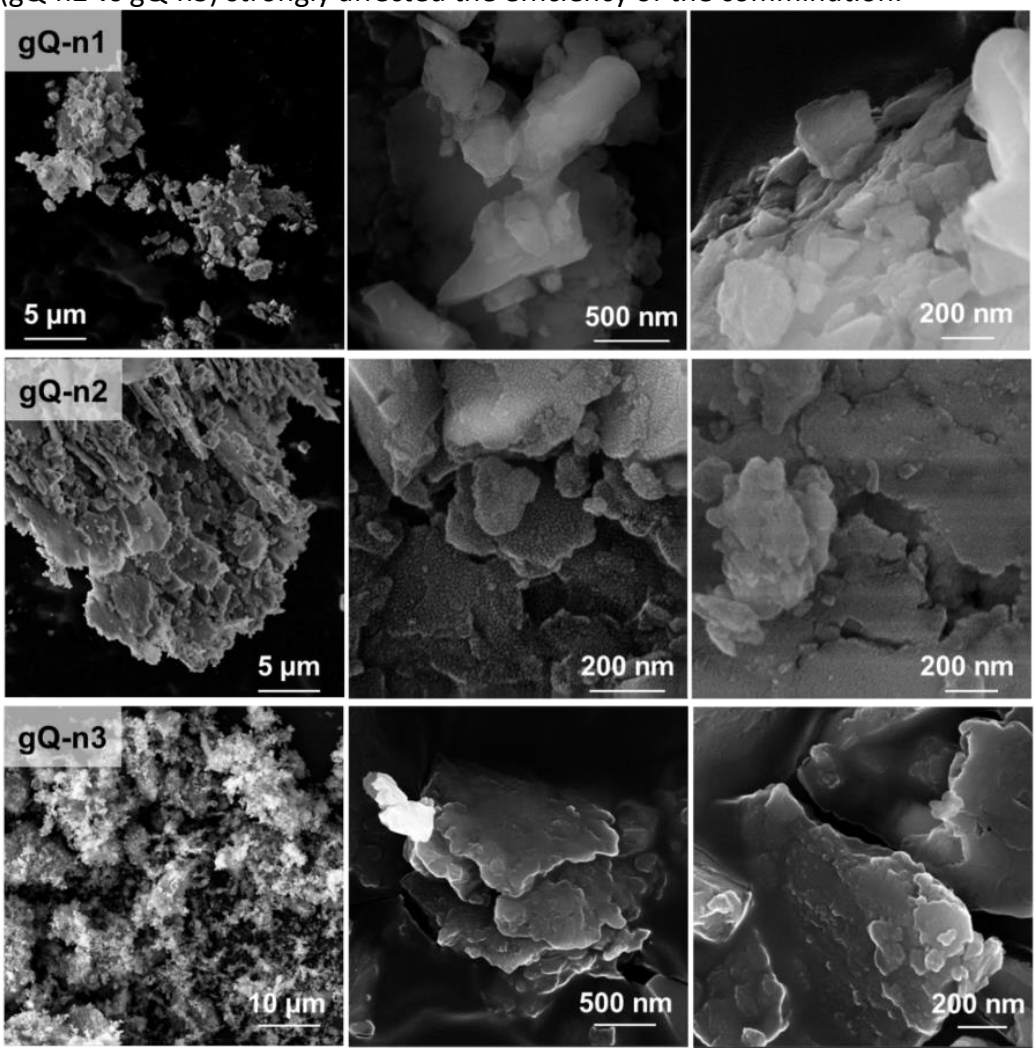

Figure 2.8: Morphology of the three nanometric quartzes at different magnifications.

The morphology of these nanometric quartzes is shown in Figure 2.8. The micrographs showed that the material is organized in micrometric lamellar clusters made up of nanometric and submicrometric particles. Some isolated submicrometric particles were detected in gQ-n1 but were no longer visible in gQ-n2 and gQ-n3. The morphology was completely different than the one observed for respirable quartzes and the level of strong agglomeration is highlighted by the morphology analysis.

2.3.4 *Crystallinity analysis of nanoquartzes*

The crystallinity of the samples was checked, because high-energy milling is in fact a procedure which may alter the crystalline habit of materials, due to thermal shocks occurring in the milling jar. Moreover, also micrometric quartz particles, when fractured, show an amorphous surface layer that coexists with the crystalline bulk. [31, 32] The crystallinity of gQ-f3 and the nanoquartz samples (gQ-n1, gQ-n2, and gQ-n3) was investigated by XRPD and Rietveld refinement of the diffractograms was carried out to quantify the average crystallite size and amorphous content. The results of the XRPD analyses are reported in Figure 2.9. All the nanoquartz samples showed diffraction peaks which belongs to the quartz diffraction pattern, with regard to pristine quartz (gQ) (Figure 2.9A). However, a drastic reduction in the intensity and broadening of the peaks were observed for the gQ-f3 and gQ-n samples. A broad signal centered at 25° (2θ range) (Figure 2.9B, highlighted with *) suggested the generation of an amorphous phase for the gQ-f3 and gQ-n samples. This is consistent with the partial amorphization of quartz due to ball milling already reported in past literature. [33]

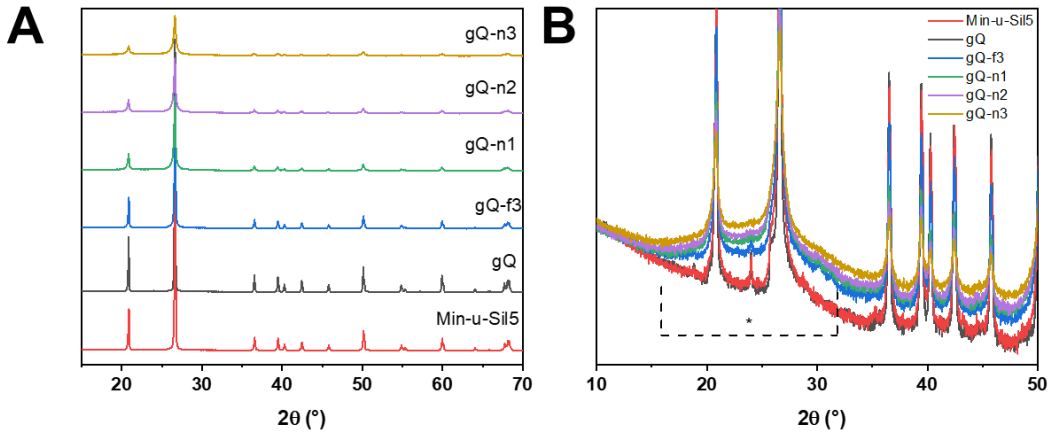

*Figure 2.9: (A) Crystallinity of the nanoquartz samples (gQ-n1, gQ-n2, and gQ-n3) compared with the as-grown micrometric quartz (gQ), the fine-fractured quartz (gQ-f3), and Min-uSil5. (B) Magnification of the diffractograms in the 10–50° region showing the amorphous broad signal, highlighted with *.*

Rietveld refinement was performed on the diffractograms of the gQ-n samples to obtain a more detailed description of the crystallite size and the amorphous phase. Very interestingly, all three gQ-ns showed a bimodal size distribution of the crystallite domains, which evidenced the presence of both submicrometric (ca. 800 nm) and nanometric (<100 nm) crystallites (Figure 2.10A) in variable proportions. This information gave rise to hypotheses about

the comminution mechanism. As a planetary milling mechanism promotes the formation of smaller particles by inducing the abrasion of the larger crystals, rather than fracturing them by inelastic collision, we speculated that the observed bimodal distribution of crystallite size may be due to this friction-like fracturing mechanism. This, as already explained in Paragraph 1.3.1 and 2.1, differs from other types of comminution apparatuses, such as the vibratory ball mill, which imparts rapid acceleration energy to the balls and sample particles and promotes fracturing mainly by inelastic collisions[12].

The increase in the content of the amorphous phase was quantified with this method and fully paralleled the increase in the intensity of the milling energetics (Figure 2.10B), from 27 to 40 wt.% for gQ-n1 and gQn-3, respectively. Along with the increase in the amorphous content, the relative weight of the submicrometric domains also progressively reduced from 16 to 6 wt.%, while the content of the nanometric domains was rather constant, ranging from 57 to 54 wt.% for gQ-n1 and gQ-n3, respectively. This suggested that the ball milling procedure adopted here was effective toward the submicrometric crystallite domains and generates nanometric crystallites. However, considering that the relative content in the nanometric domains appears constant or even slightly reduced by milling, we can then speculate that the generation of nanometric crystals might be followed by the conversion of these domains into amorphous particles, with a constant net result.

A

Sample	Quartz size domains (nm)	Nanoquartz size domains (nm)
gQ -n1	800	17.8
gQ-n2	800	15.9
gQ-n3	800	13.3

B

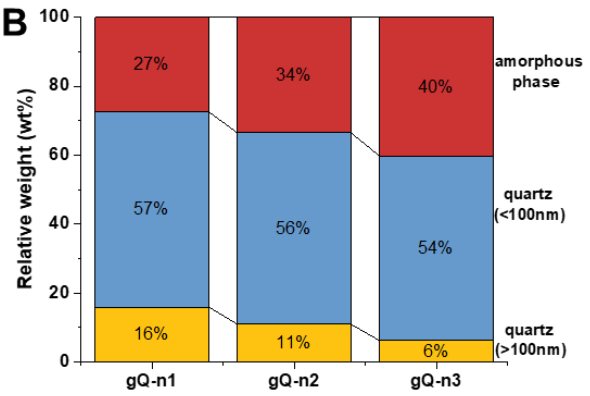

*Figure 2.10: Crystallite size domains (**A**) and relative weight (wt.%, (**B**)) of submicron (>100 nm), nano (<100 nm), and amorphous phases of gQ-n1, gQ-n2, and gQ-n3, calculated by Rietveld refinement of XRPD diffractograms.*

2.4 Main Achievements

The exploitation of mechanochemistry in the study of the alteration of the properties of quartz is a very common tool. We achieved in this chapter an almost complete modulation of this process, by variating milling apparatus, milling time and milling medium. Some predictable phenomena were observed by modifying the milling time or enhancing the energy applied during the comminution. Even if the most crucial milling parameter is considered the milling time by the literature, it was possible to reduce it to achieve a sample with the desired characteristics in shorter amount of time, by modifying other parameters (milling balls, milling medium). This modulation allowed to obtain the desired milled quartz, both micrometric or nanometric, and the bulk properties of the samples were successfully analyzed by Scanning Electron Microscopy and X-Ray Powder Diffraction. The modulation of the comminution of quartz was a crucial crossroad to obtain a model fractured quartz useful for studies described in the following chapters.

2.5 Bibliography

1. Donaldson, K. and P.J. Borm, *The quartz hazard: a variable entity.* The Annals of occupational hygiene, 1998. **42**(5): p. 287-294.
2. Schins, R.P., et al., *Surface modification of quartz inhibits toxicity, particle uptake, and oxidative DNA damage in human lung epithelial cells.* Chemical research in toxicology, 2002. **15**(9): p. 1166-1173.
3. Pavan, C. and B. Fubini, *Unveiling the variability of "quartz hazard" in light of recent toxicological findings.* Chemical Research in Toxicology, 2017. **30**(1): p. 469-485.
4. Rimola, A., et al., *Silica surface features and their role in the adsorption of biomolecules: computational modeling and experiments.* Chemical reviews, 2013. **113**(6): p. 4216-4313.
5. Sohoni, S., R. Sridhar, and G. Mandal, *The effect of grinding aids on the fine grinding of limestone, quartz and Portland cement clinker.* Powder technology, 1991. **67**(3): p. 277-286.
6. Burmeister, C.F. and A. Kwade, *Process engineering with planetary ball mills.* Chemical Society Reviews, 2013. **42**(18): p. 7660-7667.
7. Kabezya, K. and H. Motjotji, *The effect of ball size diameter on milling performance.* J. Mater. Sci. Eng, 2014. **4**(1): p. 1-3.
8. Mio, H., et al., *Optimum revolution and rotational directions and their speeds in planetary ball milling.* International Journal of Mineral Processing, 2004. **74**: p. S85-S92.
9. Mio, H., et al., *Effects of rotational direction and rotation-to-revolution speed ratio in planetary ball milling.* Materials Science and Engineering: A, 2002. **332**(1-2): p. 75-80.
10. Toozandehjani, M., et al., *Effect of milling time on the microstructure, physical and mechanical properties of Al-Al2O3 nanocomposite synthesized by ball milling and powder metallurgy.* Materials, 2017. **10**(11): p. 1232.
11. Gorrasi, G. and A. Sorrentino, *Mechanical milling as a technology to produce structural and functional bio-nanocomposites.* Green Chemistry, 2015. **17**(5): p. 2610-2625.
12. Piras, C.C., S. Fernández-Prieto, and W.M. De Borggraeve, *Ball milling: a green technology for the preparation and functionalisation of nanocellulose derivatives.* Nanoscale Advances, 2019. **1**(3): p. 937-947.
13. Suryanarayana, C., *Mechanical alloying and milling.* Progress in materials science, 2001. **46**(1-2): p. 1-184.

14. Shin, H., et al., *Effect of ball size and powder loading on the milling efficiency of a laboratory-scale wet ball mill.* Ceramics International, 2013. **39**(8): p. 8963-8968.
15. Anand, K., S. Varghese, and T. Kurian, *Effect of ball size on milling efficiency of zinc oxide dispersions.* Part. Sci. Technol, 2018. **36**(3): p. 308-311.
16. Hasegawa, M., et al., *The effect of liquid additives on dry ultrafine grinding of quartz.* Powder Technology, 2001. **114**(1-3): p. 145-151.
17. Hou, T.-H., C.-H. Su, and W.-L. Liu, *Parameters optimization of a nano-particle wet milling process using the Taguchi method, response surface method and genetic algorithm.* Powder technology, 2007. **173**(3): p. 153-162.
18. Pastero, L., et al., *Synthesis of α-quartz with controlled properties for the investigation of the molecular determinants in silica toxicology.* Crystal Growth & Design, 2016. **16**(4): p. 2394-2403.
19. Pavan, C., et al., *Nearly free surface silanols are the critical molecular moieties that initiate the toxicity of silica particles.* Proceedings of the National Academy of Sciences, 2020. **117**(45): p. 27836-27846.
20. Turci, F., et al., *Revisiting the paradigm of silica pathogenicity with synthetic quartz crystals: the role of crystallinity and surface disorder.* Particle and Fibre Toxicology, 2016. **13**(1): p. 32.
21. Bellomo, C., et al., *Top-Down Preparation of Nanoquartz for Toxicological Investigations.* International Journal of Molecular Sciences, 2022. **23**(23): p. 15425.
22. Young, R.A., *The rietveld method*. Vol. 5. 1993: International union of crystallography.
23. Lutterotti, L., *Total pattern fitting for the combined size–strain–stress–texture determination in thin film diffraction.* Nuclear Instruments and Methods in Physics Research Section B: Beam Interactions with Materials and Atoms, 2010. **268**(3-4): p. 334-340.
24. Smith, R.L. and G. Sandly, *An accurate method of determining the hardness of metals, with particular reference to those of a high degree of hardness.* Proceedings of the Institution of Mechanical Engineers, 1922. **102**(1): p. 623-641.
25. Mukherjee, S., *Applied mineralogy: applications in industry and environment*. 2012: Springer Science & Business Media.
26. FRITSH. *Explanation on hardness data*. Available from: https://www.fritsch-international.com/fileadmin/Redakteur/Produkte/Explanations_on_hardness_data.pdf.

27. Avolio, R., et al., *A multitechnique approach to assess the effect of ball milling on cellulose.* Carbohydrate Polymers, 2012. **87**(1): p. 265-273.
28. Poppe, L.J., et al., *A laboratory manual for X-ray powder diffraction.* US Geological Survey open-file report, 2001. **1**(041): p. 1-88.
29. Pavan, C., et al., *Nearly free surface silanols are the critical molecular moieties that initiate the toxicity of silica particles.* Proceedings of the National Academy of Sciences, 2020. **117**(45): p. 27836-27846.
30. Luo, T., et al., *Alkoxylation Reaction of Alcohol on Silica Surfaces Studied by Sum Frequency Vibrational Spectroscopy.* The Journal of Physical Chemistry C, 2021. **125**(16): p. 8638-8646.
31. Glasson, D.R., *Vacuum balance studies of milled material and mechanochemical reactions.* Thermochimica Acta, 1981. **51**(1): p. 45-52.
32. Finch, G.I., *The Beilby Layer on Non-Metals.* Nature, 1936. **138**(3502): p. 1010-1010.
33. Kohobhange, S., et al., *The effect of prolonged milling time on comminution of quartz.* Powder Technology, 2018. **330**: p. 266-274.

CHAPTER 3: surface reconstruction and ageing of milled quartz

3.1 Background.

Quartz subjected to mechanical fracturing has been studied for several decades, [1, 2] and, in recent years, it was proved that the act of fracturing is crucial in the rising of a toxic response. [3] Quartz of synthetic origin obtained by hydrothermal synthesis of respirable size was tested non membranolytic both *in vitro* and *in vivo*. When the same quartz was subjected to ball milling, was tested membranolytic *in vitro* and toxic *in vivo*. [3, 4] The study challenged the hypothesis that crystallinity is the crucial feature able to trigger the molecular initiating event (MIE) of the pathogenicity of quartz. Not all quartz samples proved to be membranolytic, and, on the other hand, some types of amorphous silicas were highly membranolytic and inflammogenic. Nearly free silanols (NFS), pairs of surface silanols sitting at a specific relative distance, were individuated as the specific feature able to trigger membranolysis. [4] The origin of the membranolytic activity and the formation of NFS is strongly linked to the fracturing of quartz crystals. The mechanical process applied on quartz crystals indeed causes the breakage of the polar-covalent bond between silicon and oxygen, creating new highly energetic surface sites. These sites, exposed for the first time, react with the molecules present in the external environment to produce more stable surface features. Since NFS that are generated during fracturing confer membranolytic activity to quartz, a molecular understanding of the surface reconstruction and rearrangement processes occurring to quartz during and after fracturing is highly envisaged.

It is largely held that the molecular external environment may influence the surface features that are generated on quartz surface during fracturing. (see Introduction, Paragraph 1.3), but a systematic study on the effect of different molecular environments on the surface reconstruction of quartz has never been carried out so far. Molecular oxygen (O_2) and water vapor (H_2O) are the two species that can react with surface active sites exposed during fracturing

and the opening of Si–O bonds. In particular, water vapor is able to interact with silica surface and generate silanol species. [5]

In this work, two quartz samples of synthetic and mineral origin and four milling environments were selected to challenge the hypothesis that different milling environments may lead to different surface reconstruction processes on quartz and this in turn may modulate the membranolytic potency of the dust. Beside investigation the effect of milling in different environments, some of the milled quartz dusts were stored in controlled ageing environments. Understanding the effect of the ageing environments on quartz dust reactivity is a key step in unveiling the molecular mechanisms of action of SiO_2 surfaces with biomolecules, membranes and tissue. It is indeed largely held that freshly milled quartz dust is more toxic than aged one. [2, 6] However, the origin of change in toxic potential has not be correlated to any of the chemical characteristic of the surface of silica yet. By storing selected quartz dusts in controlled ageing environments, it was possible to follow the evolution of their membranolytic activity with ageing time.

The two quartz samples were highly pure and were not previously milled nor crushed. Industrial quartz dust, commonly used for toxicological tests, is generally obtained by milling and is often contaminated by metal impurities (Fe or Al) or other minerals (*i.e.*, clays, silicates, alumina) that may contribute to the overall reactivity of the dust. Impurities and uncontrolled milling conditions create a highly heterogeneous dust, both in terms of surface chemistry and particle size distribution. Therefore, the use of industrial quartz dusts prevents the molecular understanding of the process involved and hampers the observation of causal correlation between quartz chemistry and biological effects.

The surface of quartz milled in the four different external environments was characterized by EPR spectroscopy, which is a very sensitive and immediate spectroscopic technique able to detect paramagnetic defects in solids. [7, 8] When the covalent bond between silicon and oxygen is broken, radicals or ions can be generated (Paragraphs 1.3 and 1.2.2.2). Radicals are paramagnetic species due to an unpaired electron, and they can be detected by means of EPR spectroscopy. A vast scientific literature exists on the characterization of quartz defect centers and unpaired electrons by means of EPR spectroscopy. [9, 10] In this work, we take advantage of the specific sensitivity of EPR to investigate the evolution of radical species upon changing the milling and ageing environments. The EPR data were discussed also at the light of the membranolytic activity of quartz dusts that were milled and aged in the different environments.

3.2 Materials and methods

3.2.1 Ball milling of gQ and mQ.

The milling protocol was already optimized in Chapter 2. Both quartzes were subjected to the planetary milling protocol (gQ-f2 and mQ-f) according to the milling conditions reported in Chapter 2.
Milling in inert atmosphere was performed opening and closing the milling jar inside an Argon filled glove box before and after milling (MBraun LABstar glove box supplied with pure 5.5 grade argon, <0.5 ppm O_2, <0.5 ppm H_2O).
Water vapor saturated atmosphere was artificially produced inside a glove bag filled with Argon and liquid water and after some cycles of degassing in order to exclude oxygen from the atmosphere of milling: the jar was charged with quartz inside the glove bag and sealed. After milling the jar was opened again inside the same glove bag. An analogous procedure was used for the milling in dry air, with a glove bag filled with dry air (SAPIO, 78% N_2, 21% O_2, 1% Ar). The concentration of water vapor inside the glove bag was checked before the closing of the glove bag with a hygrometer (ThermoPro TP157).

3.2.2 EPR spectroscopy.

Analyses of the radical species were performed with continuous wave electron paramagnetic resonance spectroscopy (CW-EPR), at 77 K. The analyses were performed in a Bruker ER035 M NMR gaussmeter with the power of 0.3 mW and a modulation of 2G. Central field at 3380 Gauss. Samples were weighed and inserted in a sealed EPR cell and degassed before analysis.

3.2.2.1 Treatment with probe molecules.

Selected mQ-f and gQ-f2 samples were sealed in an EPR cell inside the glove box and degassed under vacuum (residual pressure $1x10^{-4}$ mbar). Water vapor was firstly purified by three cycles of freeze-pump at 77K and then expanded in vacuum line in contact with quartz. Approximately 25 mbar of water vapor were used. Oxygen gas (SAPIO gas, Italy, purity 6.0) was contacted with quartz in the same way, without previous purifications (30 mbar). Carbon monoxide (CO, SAPIO gas, Italy, purity 99%) was contacted in the same way as oxygen, without further purifications (5 mbar). Every treatment was performed in a vacuum line separated from the EPR spectrometer. After every treatment, the cell was inserted in the spectrometer and analyzed.

3.2.2.2 Thermal treatments

–H_2O/–O_2 mQ-f and gQ-f2 were sealed in an EPR cell, connected to a vacuum line and degassed (residual pressure 1x10^{-4} mbar). The cell, connected to the vacuum line, is heated at 373, 473 and 673 K respectively, for 45 minutes. The heating cycles were subsequent on the same EPR cell.
For the heating process in an oxidative environment, –H_2O/–O_2 mQ-f and gQ-f2 were sealed in an EPR cell connected to a vacuum line and degassed (residual pressure 1x10^{-4} mbar). After degassing, 30 mbar of O_2 were expanded on the vacuum line and contacted with quartz inside the EPR cell. Then the cell was heated at 473 K for 45 minutes. After the heating treatment, the cell is degassed and the quartz analyzed.

3.2.3 Hemolysis assay.

RBCs were purified from sheep blood in Alsever's solution by centrifugation at 3,000 × g for 2 min (Rotina 380R; Hettich, MA) and washing three times with 0.9% NaCl. RBCs were suspended in 10 mM PBS at the final concentration of 5% by volume. Sheep RBCs were used because they showed a sensitivity to silica very similar to that of human RBCs. [11] Particles were dispersed in 10 mM PBS and sonicated 2 min in a bath just before testing. Serial dilutions of the starting particle dispersions (300 cm^2/ml) were performed according to the final surface area doses used for experiments. Dispersions were distributed in quadruplicate in a transparent 96-well plate (150 µL/well), and the RBC suspension was then added (75 µL/well). Negative and positive controls consisted of 10 mM PBS and 0.1% Triton-X 100 in PBS, respectively. The plate was incubated on a plate shaker at 37°C for 30 min, and then centrifuged at 216 × g for 5 min. Supernatants were transferred to a new plate (75 µL/well), and the absorbance of the hemoglobin released was determined at 540 nm on a UV/vis spectrophotometer (Ensight, Perkin-Elmer, Waltham, MA) using the software Kaleido 2.0 (Perkin-Elmer).

3.2.3.1 Treatment with liquid water.

An aliquot of –H_2O/–O_2 mQ-f was contacted with Ultrapure water (milliQ, 18.2 MΩ·cm (25°C)) and suspended for 30 minutes with the same initial dose of the hemolysis test (300 cm^2/ml). The suspension is then centrifuged for 10 minutes at 10,000 x g (Rotina 380R; Hettich, MA). The supernatant was discarded, and the pellet obtained is dried under vacuum and kept in inert atmosphere until the hemolysis assay.

3.2.3.2 *Treatment with hydrofluoric acid (HF).*

An aliquot of iQ-1 is suspended in a solution of HF (10% w/w) in water and kept there for 10, 20 and 30 minutes. After it, quartz is washed with abundant milliQ water and centrifuged for 10 minutes at 10,000 × g (Rotina 380R; Hettich, MA). The supernatant was discarded, and the pellet obtained subjected to hemolysis.

3.2.4 Infrared Spectroscopy

In brief, iQ-1, IR measurements were carried out in the diffuse reflectance mode, using a Spectra-Tech diffuse reflectance unit, equipped with an environmental chamber allowing the connection to a conventional vacuum line (residual pressure, ≤1 × 10^{-4} mbar), and to carry out *in situ* all desorption/adsorption experiments. The samples were analyzed in powder form, with ∼50 mg of silica sample. Spectra were collected with a Bruker Vector 22 FTIR spectrometer (Globar source, MCT detector; resolution, 2 cm^{-1}) averaging 128 scans for spectrum to obtain a good signal-to-noise ratio. iQ-1, before and after the treatment with HF, underwent an H/D isotopic exchange by adsorption/desorption of D_2O (Sigma-Aldrich; 99.90% D) in order to convert surface silanols (SiOH) in the SiOD form, to discriminate silanols directly exposed to the surface.
IR measurements were performed by prof. Lorenzo Mino's group.

3.3 Results and discussion

3.3.1 Ball milling in different external environments produces different chemical features on the surface of quartz.

Quartz of synthetic (gQ) and mineral origin (mQ) was subjected to the milling protocol optimized in Chapter 2, and the finely fractured samples gQ-f2 and mQ-f were used in this experimental part. The milling procedure was carried in four different molecular environments, summarized in Table 3.1.

Table 3.1: Description of the four molecular environments used to evaluate whether different surface chemistry is obtained during ball milling.

Sample	Milling environment	H_2O	O_2
-H_2O/-O_2	Argon (5.5 grade, O_2 < 0.5 ppm, H_2O < 0.5ppm)	NO	NO
-H_2O/+O_2	N_2 and O_2 mix (79%-21%) + H_2O (vap) RH%= 10% ‡	NO	YES
+H_2O/-O_2	Argon + H_2O (vap) RH%= 100%	YES	NO
+H_2O/+O_2	External air. N_2 and O_2 mix (79%-21%) + H_2O (vap) RH%= 30%	YES	YES

‡ RH%= relative humidity percentage measured at 25°C.

The aim was to modulate the concentration of the two active molecules present in the air (water vapor and oxygen) aiming to individuate an origin in the surface reconstruction process which initiate silica membranolytic activity.

3.3.1.1 Effect of the milling environment on the radical profile of milled quartz.

The radical profile of gQ-f2 and mQ-f was characterized by EPR spectroscopy, aiming to check the formation of defective sites and radical adducts induced by ball milling. For brevity, we reported here only the spectra of mQ-f because we obtained virtually identical spectra for gQ-f2.
In Figure 3.1 the EPR spectra of mQ-f milled in the four different external environments are reported. Radical species were formed under the four milling environments, albeit to a very different extent. The grey spectrum represents the EPR spectrum of pristine quartz (mQ) before ball milling and no significant signals were detected. Under the ($-H_2O/-O_2$) milling condition, which corresponds to the most inert environment that can be produced in our laboratory, the EPR spectrum of mQ-f is characterized by the predominance of the silyl radical ($Si^{\bullet}$, highlighted in red). This species is often reported in the literature as the E' center. [12] The silyl radical is generated by the homolytic fracturing of the covalent Si−O bond. Structurally, it is a Si atom with a dangling bond located in a sp^3 orbital. The signal has an axial geometry dominated by the $g_{\perp}$ component at 2.000. The $g_{//}$ component of the axial signal is not clearly visible because of the superimposition of other spectral lines [13, 14]. The siloxyl radical, $SiO^{\bullet}$, is EPR silent because of the degeneracy of the ground state, which implies a relaxation time too long for the detection of the signal. This consideration is only related to surface radicals which are formed during surface reconstruction of the milled crystals. Bulk siloxyl radicals have been in fact generated by irradiation and reported by Griscom and co-workers. [15-17]
Other two radical species could be observed in the EPR spectrum of $-H_2O/-O_2$ mQ-f and labeled in green and blue. Those signals as usually assigned to the surface bound superoxide radical ($Si^{+}O_2^{-\bullet}$) and to the peroxyl radical ($SiOO^{\bullet}$), respectively.
The formation of surface bound superoxide radical is generally described by the reduction of molecular oxygen from an electron donor center and the subsequent stabilization by a silyl cation ($\equiv Si^{+}$). [13]

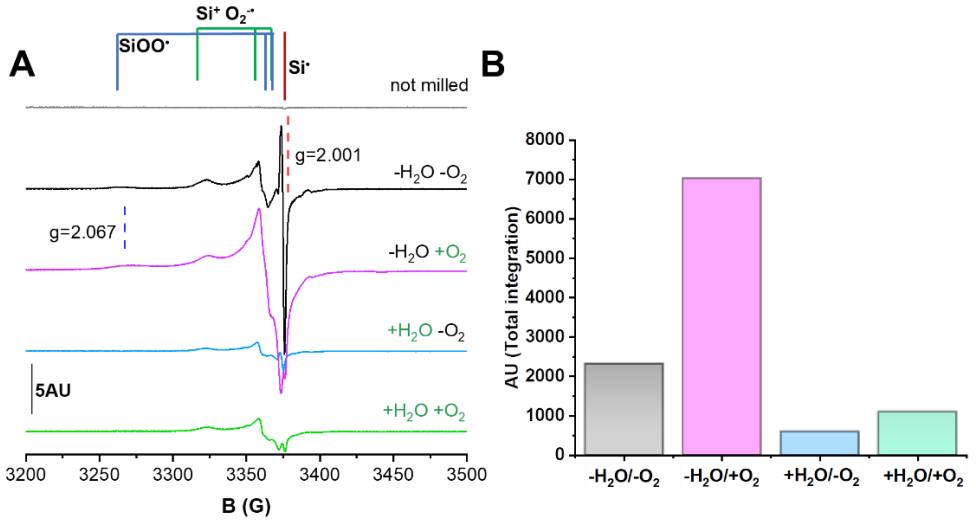

Figure 3.1: Radical profile of milled quartzes in the four different milling environments. (A) EPR spectra of the four mQ-f samples recorded at 77K. In grey the EPR spectrum of the same quartz before milling. The three radical species individuated has been assigned according to literature. In red, silyl radical ($Si^{\bullet}$, $g_{\perp}$= 2.000); in blue peroxyl radical ($SiOO^{\bullet}$, g_x=2.002, gy=2.007 and g_z= 2.067) and in green the surface-bound superoxide radical ($Si^{+}O_2^{-\bullet}$, g_x=2.002, gy=2.010 and g_z= 2.031).[18, 19] (B) Double-integrated values of the EPR spectra to define the amount of radical species in each sample. Signals were normalized according to the weight of the sample in the EPR cell.

This partially reduced radical species originates an intermolecular adduct, with the unpaired electron located in a non-bonding oxygen 2p-orbital. The generation of this radical in a $–H_2O/–O_2$ environment is difficult to hypothesize, because of the substantial absence of molecular oxygen in the environment. We observed here a limited yet detectable amount of this radical and we speculated that some structural or adsorbed residual oxygen must still be present in the milling environment.

The third species, labeled in blue, was assigned to the peroxyl radical (≡Si–O–O•). Peroxide species are strongly anisotropic in nature and exhibit the characteristic g_z = 2.067. The unpaired electron occupies a 2p orbital of oxygen, geometrically perpendicular to the projection plane of the silica surface. [16, 20] In an oxygen-rich environment, the generation of peroxide species in quartz is normally explained by the reaction of the silyl (Si•) and siloxyl (SiO•) radicals with molecular oxygen. The occurrence of the peroxyl radical in our oxygen-free environment can be explained by some structural reactions/rearrangements that may occur during ball milling. Under mechanic deformation, the generation of peroxyl linkages (≡Si–O–O–Si≡) are reported to be the consequence of the distortion of the quartz crystal lattice.

The Si−O homolytic cleavage of this species yields a peroxyl and a silyl radical, according to the following reaction [15, 21, 22]:

$$\equiv Si–O–O–Si\equiv \rightarrow \equiv Si–O–O^{\bullet} + {}^{\bullet}Si\equiv$$

Even if all silyl, peroxyl and surface bound superoxide are present in the EPR spectrum of $–H_2O/–O_2$ mQ-f, the predominance of the silyl radical is clear.
Different relative abundances of the three radical species are observed for the quartz milled in the presence of molecular oxygen ($–H_2O/+O_2$ mQ-f, Figure 3.1A). The oxygen-rich environment caused a dramatic change in the EPR spectrum, with the signal components due to the superoxide and the peroxyl radicals significantly more intense than the E' signal. This is coherent with the presence of oxygen in the environment, which favored the formation of oxygenated radical species. The intensity of the EPR spectrum (pink curve) suggests that molecular oxygen reacts with active sites generated by ball milling on the surface of quartz, by creating oxygen-centered radicals.
When water vapor was added to the milling environment ($+H_2O/–O_2$ and $+H_2O/+O_2$, blue and green spectra, respectively, in Figure 3.1A), the intensity of the radical profiles was lower than what was recorded for the first two milling environments. These data prove that the presence of water vapor in the milling environment dramatically affects the amount of radicals that occur on the quartz surface after milling. Water molecules likely interact with relatively stable radical sites on quartz surface and convert them into neutral species, specifically silanols. Transient radicals ($^{\bullet}OH$ and $H^{\bullet}$) are generally formed during this reaction and quickly annihilated. A possible set of surface radicals-water reactions is reported:

(1) $\equiv Si^{\bullet} + H_2O \rightarrow \equiv Si–OH + H^{\bullet}$
(2) $\equiv Si–O–O^{\bullet} + H_2O \rightarrow \equiv Si–OOH + {}^{\bullet}OH$
(3) $\equiv Si–O^{\bullet} + H_2O \rightarrow \equiv Si–OH + {}^{\bullet}OH$

The double-integrated values of the EPR spectra of all four milling environments are reported in Figure 3.2B. The comparative evaluation of these data highlights the strong increase of surface radicals that are generated when quartz is milled in the presence of oxygen ($–H_2O/+O_2$) due to the increased amount of $Si^{+}O_2^{-\bullet}$ and $SiOO^{\bullet}$ with respect to oxygen-free environment. Consistently with qualitative observations discussed above, the presence of water strongly reduced the amount of radical species also in the presence of oxygen ($+H_2O/+O_2$).
Overall, we were able to propose a molecular mechanism of radical generation that yields mainly E' centers (and the EPR silent $SiO^{\bullet}$) when milling is performed in an oxygen- and water-free environment. The presence of

oxygen dramatically increases the amount of radicals, specially favoring the generation of oxygen-centered radicals and the unveiling of EPR silent $SiO^{\bullet}$. Water vapor, also in the combination with oxygen, strongly reduced the overall amount of radical species by reacting with them and forming surface silanols. The larger amount of radicals that were generated in water-free with respect to water-rich environments is consistent with the homolytic cleavage of the Si−O bond, that is energetically favored by non-polar environments, such as Ar or O_2. Furthermore, our data clearly indicate that the vast majority of the radical species observed are surface species and the reactivity of oxygen and water towards those species is very different in nature. To further elucidate the different reaction mechanisms of quartz surface, the $–H_2O/–O_2$ mQ-f was reacted with probe molecules and heated at different temperatures.

3.3.2 Radical species on milled quartz exhibit different reactivity

Among the milled quartz samples, the $–H_2O/–O_2$ mQ-f and gQ-f2 were chosen to investigate the reactivity of the radical species evidenced in the previous paragraph. We selected the quartz milled in the inert environment ($–H_2O/–O_2$) assuming that its radical species are the most reactive, out of the four conditions. The assumption is reasonable because the surface of the $–H_2O/–O_2$ quartz is not affected by reactive molecules that were removed from the milling environment, and the radicals observed were fundamentally generated by homolytic cleavage of SiO bonds. In the next paragraphs, $–H_2O/–O_2$ quartz is exposed to water vapor (Paragraph 3.3.2.1), to molecular oxygen (Paragraph 3.3.2.2), to CO (Paragraph 3.3.2.3) and finally to thermal treatments (Paragraph 3.3.2.4). It is worth noting that the species reactivity assessment was performed within 24-48 hours following the milling procedure.

3.3.2.1 Reactivity of milled quartz towards molecular water

In Figure 3.2A, $–H_2O/–O_2$ mQ-f was treated with 25 mbar of water vapor. Water vapor reacted immediately with superoxide and peroxyl species, and a complete suppression of their signals was observed. Silyl radical was still present but the intensity was strongly reduced compared to the spectrum before the exposure to water. This suggests a lower reactivity or a lower accessibility from the surface of the E' centers with respect to oxygen-centered radicals. This is consistent with previous findings on the radical profile of quartzes analyzed months after milling.[23][9]. Silyl radicals are generally the most stable active sites of fractured silica surfaces, and they are visible also on quartz samples that were milled months or years before the

EPR analysis. To explain the stability of these other ways transient species, it is speculated that a certain amount of silyl radicals in this quartz is probably hosted in subsurface layers and in the grain borders of the material. [9, 18]
In panel A and A' is reported the degassed spectrum of $–H_2O/–O_2$ mQ-f. The drastic change in shape above described is then irreversible, because after degassing the initial shape of the spectrum before treatment is not restored. We can hypothesize that the reactions occurring on the surface of silica are the following and involve the generation of surface silanols or hydroperoxides:

1. $\equiv Si^{\bullet} + H_2O \rightarrow \equiv Si—OH + H^{\bullet}$
2. $\equiv Si—O—O^{\bullet} + H_2O \rightarrow \equiv Si—OOH + OH^{\bullet}$
3. $\equiv Si^{+}\ O_2^{-\bullet} + H_2O \rightarrow Si—OH + HO_2^{\bullet}$

The radicals ($H^{\bullet}$, $OH^{\bullet}$ and $HO_2^{\bullet}$) that are generated by the reactions are not detectable likely due to the too short halftime. Indeed, small radical species rapidly recombine with surface reactive sites on silica or with each other to generate non-radical molecules that can easily degassed (H_2, H_2O, H_2O_2). This is in good agreement with computational studies, which observed that a cleaved surface of quartz is able to exothermally react with water vapor. [5, 24, 25] Another interesting aspect that can be discussed from Figure 3.2A' regards the different reactivity of the radical species detected on the $–H_2O/–O_2$ and on the $+H_2O/–O_2$, *i.e.,* the quartz directly milled with water vapor (Figure 3.1A, blue spectrum). While surface bound superoxide radical in $–H_2O/–O_2$ immediately reacted when exposed to water, in $+H_2O/–O_2$ a modest but evident amount of surface bound superoxide radical is retained after milling. This suggests a different reactivity of the surface itself according to the milling environment. A further proof of the different reactivity of surfaces generated in different milling environments is observed when $–H_2O/+O_2$ is exposed to water vapor (Figure 3.2C). The exposure to water of this sample milled in an oxygen-rich environment did not alter the shape of the EPR signal. We can assume that the oxygenated radicals generated in the $–H_2O/+O_2$ are more stable than the radicals of the sample milled in the water- and oxygen-free environment ($–H_2O/–O_2$ mQ-f).
Furthermore, when $–H_2O/–O_2$ mQ-f was exposed to water vapor for a 50-day timespan (Figure 3.2B-B'), a strong reduction of the overall intensity of the spectrum was observed with respect to the $–H_2O/–O_2$ mQ-f aged in an non-reactive environment, which radical population was virtually superimposable with the non-aged $–H_2O/–O_2$ mQ-f. Our data support the hypothesis that most of the radical species are located on the surface, and their reactivity or accessibility is modulated by the milling environment.

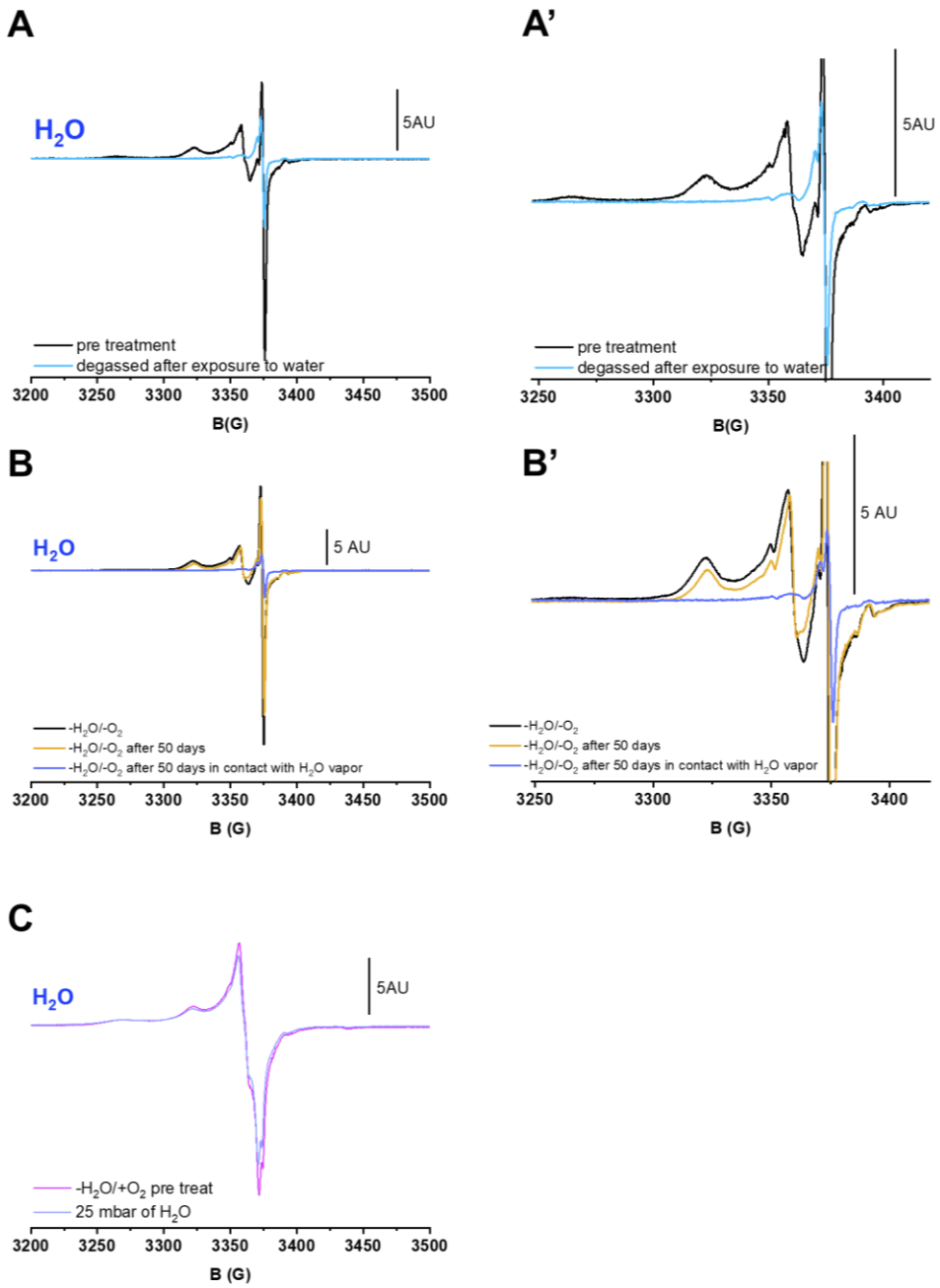

Figure 3.2: mQ-f exposed to water vapor. All spectra recorded at 77K. (A-A') –H_2O/–O_2 before and after exposure to H_2O vapor, 25 mbar, and subsequent degassing (B-B') –H_2O/–O_2 mQ-f radical profile after 24 hours, after 50 days kept in an Ar environment and after 50 days exposed to water vapor. (C) –H_2O/+O_2 exposed immediately after milling to H_2O vapor (25 mbar). (A' and B' are the magnification of the respective spectra.)

3.3.2.2 Reactivity of milled quartz towards molecular oxygen

The same experimental set up was employed to test the interaction between $–H_2O/–O_2$ mQ-f and molecular oxygen (Figure 3.3A and B). Molecular oxygen, directly allowed in the evacuated EPR cell (residual pressure < 10^{-4} mbar) with a p_{O_2}≈30 mbar, strongly interacts with oxygenated species, both $SiOO^{\bullet}$ and $Si^{+}O_2^{-\bullet}$, virtually suppressing their signals (see magnification inset, Figure 3.3A). On the contrary the signal from silyl radical (E' centers) remains largely unchanged. The apparent increase of the EPR intensity of E' centers is in fact due to the O_2 adsorbed on the surface of quartz at 77K and was already documented by Costa and co-workers. [26]

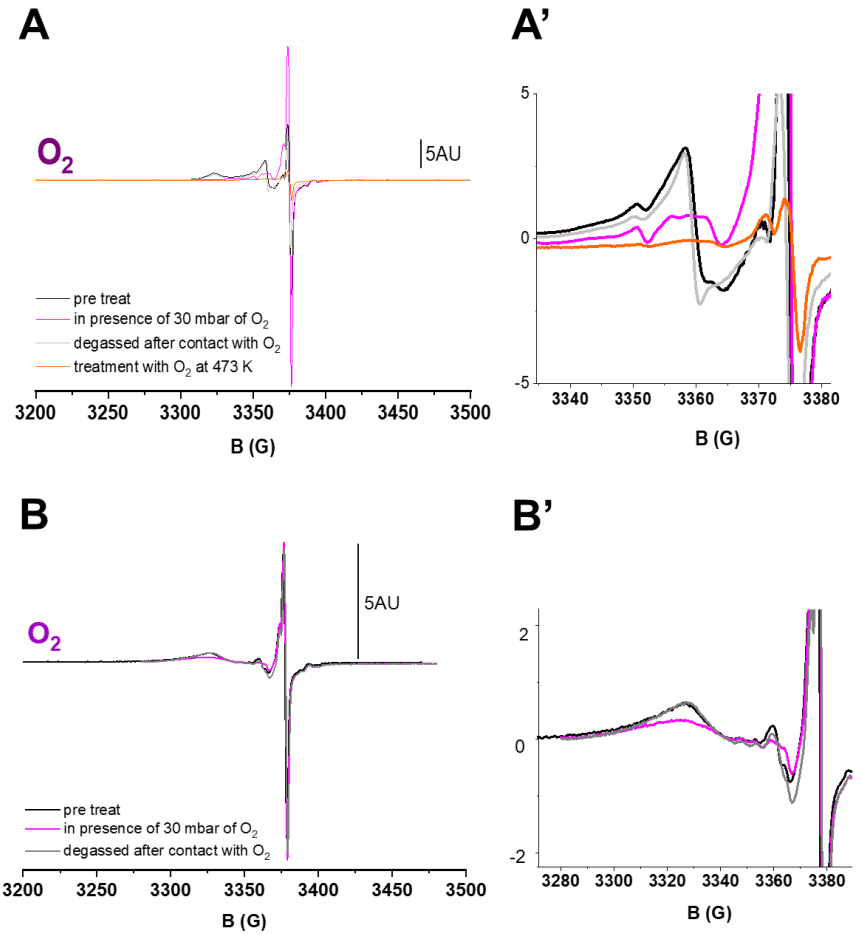

Figure 3.3: $–H_2O/–O_2$ mQ-f exposed to molecular oxygen. (A-A') $–H_2O/–O_2$ in presence of molecular oxygen at 77K and subsequent degassing (at 77K). Treatment of $–H_2O/–O_2$ with 30 mbar of O_2 at 473K for 45 minutes. Before the analysis the cell was degassed under vacuum. (B-B') the same treatment with O_2 at RT.

Degassing the EPR cell up to residual $p_{O_2} < 10^{-4}$ mbar, the EPR signal of pristine material was restored, signaling a reversible interaction of oxygen with radical centers on quartz surface. The interaction must be prevalently magnetic in nature, with the electrons in the HOMO π* orbitals of O_2 broadening the EPR signal of the surface-accessible radicals of quartz. When oxygen is removed, the magnetic interaction is reverted, and the signal is restored. According to the kinetic-molecular theory of gases, this type of interaction is typically observed when molecular oxygen possesses a very low kinetic energy, for instance when the spectra are recorded at lower T (*e.g.*, 77K). Therefore, we were quite surprised to observe a reversible magnetic interaction between O_2 and quartz surface radicals at T ca. 300 K. (Figure 3.3B) However, some stronger interaction might be also taken into account. In fact, a closer look at the pristine and post-O_2 outgassed quartz reveals that the shape of the superimposed superoxide and peroxyl radical signal (inset in panel A) is changed after the interaction with O_2. We may explain such different spectral profile supposing that the interaction with oxygen was irreversible for the peroxyl radical and partially irreversible for the silyl radical. We can assume that, unlike water vapor, the reaction rate between radicals and molecular oxygen is slower, also due to the homonuclear nature of the molecule. Unlike water vapor, oxygen is able to physically, but not chemically, interact with surface sites.

To gain further evidence about the nature of reactivity of O_2 with quartz radicals, we repeated the interaction at high temperature (473K, Figure 3.3A, orange spectrum). Under these experimental conditions, the changes in intensity and shape of the radical species were irreversible after outgassing up to residual $p_{O_2} < 10^{-4}$ mbar. In parallel, we checked also that the irreversible changes were largely related to the reaction with O_2 at high temperature, as demonstrated by the comparison with heating in vacuum discussed below (see Figure 3.4B).

This experiment proved that O_2 may react with surface sites but shows a lower affinity for quartz than water vapor. Beside the surface nature of all the oxygenated species, our experiments allowed us to observed the ability of molecular oxygen to partially assist the reconstruction of the surface by producing peroxo bridges (≡Si–O–O–Si≡) or other diamagnetic species, as reported in literature. [18, 27] Interestingly, molecular oxygen did not increase the amount of oxygenated radical species on the surface of $–H_2O/–O_2$ mQ-f. This is apparently in contrast with the role of oxygen that was observed during milling (see Par. 3.3.1.1). The $–H_2O/+O_2$ mQ-f was indeed particularly rich in peroxyl and superoxide radicals (Figure 3.1A) and a similarly high level of oxygenated radicals could be expected to be observed

following the reaction of oxygen with $–H_2O/–O_2$ mQ-f. This discrepancy leads to two conclusions: i. the surface of $–H_2O/–O_2$ mQ-f undergoes to rearrangement reactions that lower the reactivity towards oxygen, with respect to the new surfaces that are exposed to the $+O_2$ environment during milling; ii. the hot spots, characterized by local temperature as high as hundreds of °C that occur during milling, generate a very energetic environment that facilitates the creation of paramagnetic oxygenated species.[18] However, at room temperature, a much stronger activity in recombining reactive radical species on quartz surface was elicited by molecular water and not by oxygen.

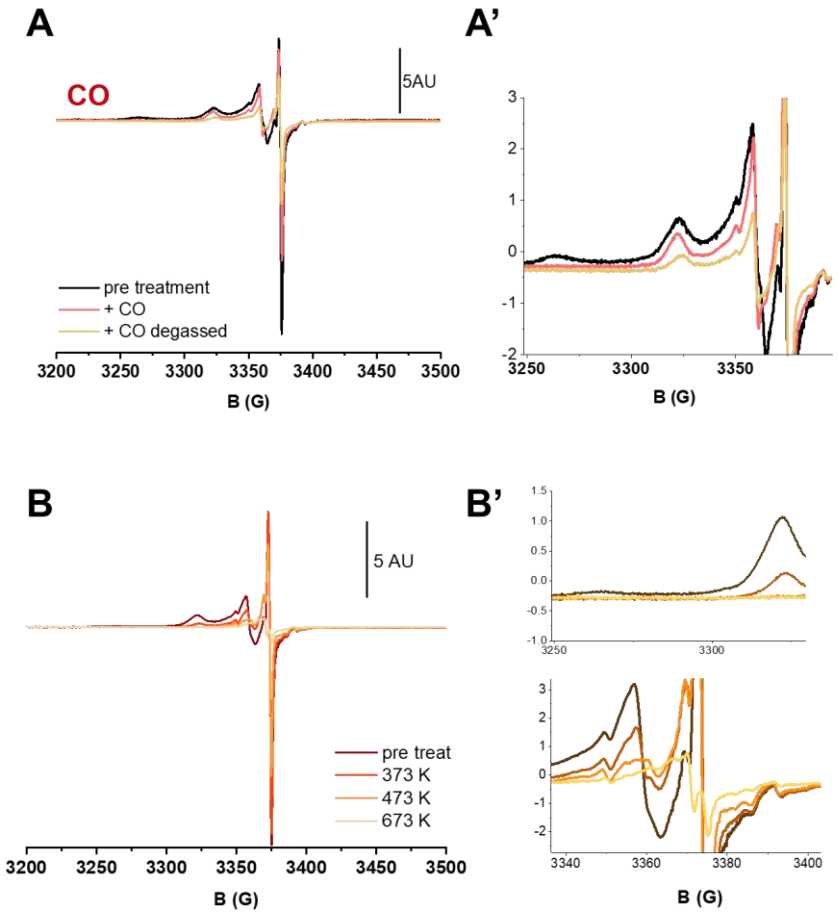

Figure 3.4: Other treatments of $–H_2O/–O_2$ mQ-f. All spectra taken at 77K. (A-A') $–H_2O/–O_2$ in presence of carbon monoxide (CO) and after degassing of CO. (B-B') Thermal treatments of $–H_2O/–O_2$ for 45 minutes at 373, 473 and 673 K.

3.3.2.3 Reactivity of milled quartz towards carbon oxide

Milled quartz ($-H_2O/-O_2$ mQ-f) was also contacted with carbon monoxide (CO) (Figure 3.4A). CO is a common IR probe molecule, [28] able to establish hydrogen bond with surface silanols. Furthermore, it is reactive towards radicals, and was used by Radtsig and co-workers to characterize the surface of quartz with EPR. [17, 29] It is considered a reducing agent, because of its ability to donate electrons. In our case, when CO was contacted with $-H_2O/-O_2$ mQ-f, an irreversible and complete suppression of the peroxyl radical occurred, together with a reduction of the amount of silyl radical and superoxide radical (Panel A'). The surface radicals of milled quartz proved to irreversibly react also with an electron donor, *e.g.*, CO.

3.3.2.4 Thermal annealing of milled quartz under vacuum

Figure 3.4B-B' reports the $-H_2O/-O_2$ mQ-f subjected to thermal treatments, with the aim of checking the thermal lability of the three radical species. The thermal treatment in vacuum (residual $p_{O2} < \approx 10^{-4}$ mbar) showed a different reactivity of the three species. Specifically, the peroxyl radical was completely annihilated at 373K, the $Si^{+}O_2^{-\bullet}$ at 473K, while the silyl radical was almost unaltered (Panel B'). At 673K the EPR spectrum was visibly simplified and exhibited the presence of a very low amount of silyl radical. From these data, we can speculate about the relative stability of quartz radicals as follows: $SiOO^{\bullet} < Si^{+}O_2^{-\bullet} < Si^{\bullet}$.

The relative low stability of oxygenated species in $-H_2O/-O_2$ mQ-f renders this sample suitable to investigate the first molecular events that happen when surface reconstruction takes place, right after milling. In fact, when oxygen and/or water are allowed during milling, the superoxide appears to be stabilized by the atmosphere and a limited radical reactivity is observed upon further addition of water vapor or oxygen.

3.3.3 External environment affects the reactivity of quartz surface towards membranolysis.

EPR spectroscopy proved that by changing the external environment during ball milling, we could modulate the distribution of radical active sites on the surface of quartz. The membranolytic activity of quartzes milled in different environments was hence measured to investigate whether such modulations translated into different silanol populations with specific membranolytic activities. The membranolytic activity of quartz resides in the exposure of some specific surface silanol families (NFS) that are able to cause the rupture of the cell membrane. To measure this activity, we used sheep red blood cells

(RBC) that are non-internalizing cells and limit the potentially membranolytic interaction with particles to the outer lipid bilayer of their cytoplasmatic membrane. Furthermore, the hemolytic test correlates well with the inflammatory activity of silica dust. [30]
The mQ-f quartz that was ball milled in the four molecular environments ($\pm H_2O/\pm O_2$) was contacted with RBC and the results reported in Figure 3.5A. For sake of brevity, the virtually identical results obtained for gQ-f2 are not reported.

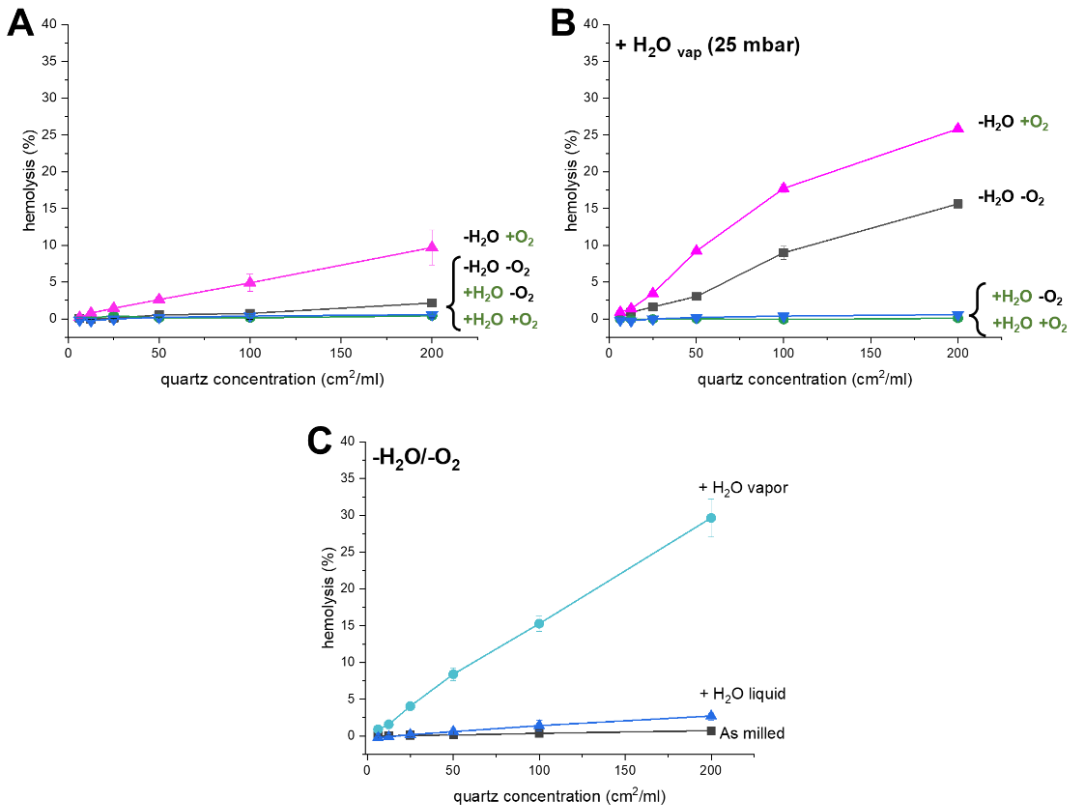

Figure 3.5: Membranolytic activity of mQ-f milled in four different milling environments. (A) hemolytic activity of mQ-f milled in the four different external environment. Hemolysis test was carried out in the first days after milling (24-48 hours) and the samples was not exposed to the external air environment to avoid interaction with O_2 and water vapor (except for $+O_2/+H_2O$ sample). The same results were obtained with gQ-f2 (B) Hemolytic activity of mQ-f milled in the four different environment after exclusive exposure to water vapor (25 mbar, around the 100% humidity). (C) Hemolytic activity of $-H_2O/-O_2$ as milled, exposed to water vapor and exposed to liquid water.

Under the four environmental conditions, $\pm H_2O/\pm O_2$ mQ-f samples were not hemolytic to a significative level (which is set to >5% with respect to the

positive control). Interstingly, as soon as the four $\pm H_2O/\pm O_2$ mQ-f samples were exposed to water vapor (ca. 25 mbar), the hemolytic activity of the samples milled in the water-free environments (*i.e.*, $-H_2O/-O_2$ and $-H_2O/+O_2$) significantly increased (Figure 3.5B). Conversely, the hemolytic activity of the samples milled in the water-rich environments ($+H_2O/-O_2$ and $+H_2O/+O_2$) was still negligible. We concluded that the absence/presence of water rather than oxygen is the determinant for generating quartz surfaces that exhibit membranolytic activity. We could speculate that mQ-f milled in water-free environment exposes reactive surface sites that can rapidly combine with molecular water to produce specific silanols that in turn confer membranolytic activity. Intriguingly, when quartz is milled in water-rich environment, such sites might not be present or accessible to water vapor. Our data suggest that the milling in water-rich environment can create more stable surfaces which do not react when the dust is exposure to water vapor after milling. The peculiar effect of water on the activation of milled quartz was straightforward yet not easy to understand, at the molecular level. In fact, the hemolysis test is carried out in an aqueous medium that preserves RBC integrity. To perform the hemolysis test, all quartz samples must be put in contact with liquid water. The suspension is produced by injecting water in an argon-sealed vial containing the pre-weighted quartz dust to be analyzed, thus we can exclude any unintentional contact with water vapor. This suggests that quartz surfaces must be sensitive to water molecules in vapor but not in liquid state.

To gain further information on the role of water phase in the onset of the hemolytic activity of quartz, we compared the activity of $-H_2O/-O_2$ milled quartz that was contacted with ultrapure liquid or vapor water, before measuring the hemolytic activity. We confirmed that liquid water did not produce any alteration of the hemolytic activity of quartz. Conversely, the $-H_2O/-O_2$ quartz sample exhibit a significant reactivity towards RBC membrane (Figure 3.5C). Even if a full explanation of this peculiar reactivity of the water-quartz system is not yet available, we concluded that only water in the form of vapor is able to modify the membranolytic activity of quartz surfaces, likely by assisting to the formation of new silanol families, in particular the NFS. [4]

3.3.4 Ageing environment can alter the membranolytic activity of milled quartz.

Ageing environment is the external environment in which the milled quartz is stored. In the previous paragraphs we analyzed how the alteration of the milling environment is able to create different kind of active sites (Paragraph 3.3.1.1), and how the newly created surfaces are not equally reactive towards RBC membranes (Paragraph 3.3.3). At this point, we wanted to observe if the

exposure to water vapor was able to further modulate the membranolytic activity of milled quartz with time. Among the milled samples we selected one water-free and one water-rich milled quartz (–H_2O/–O_2 and +H_2O/–O_2) and we stored them up to one year in two ageing environments (ae):

1. –aeH_2O: a glove box filled with Ar, RH% = 0, O_2 < 3 ppm;
2. +aeH_2O: a sealed container filled with water at $p_{H_2O} = p_{sat}$ at RT (100% humidity, $p_{H_2O} \approx 25$ mbar).

The membranolytic activity was checked at several time points to investigate the kintetics of the surface evolution and results are reported in Figure 3.6.

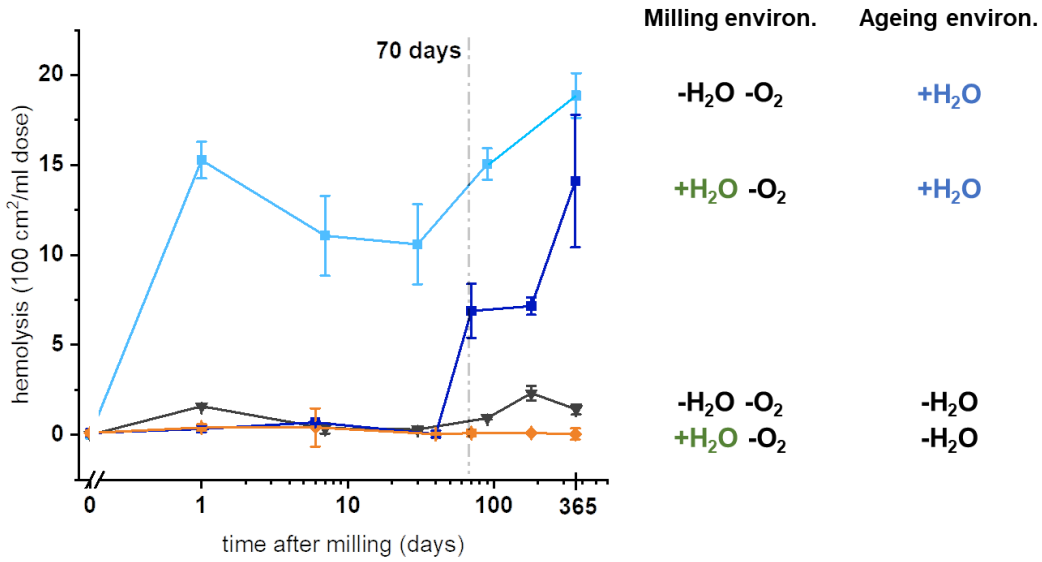

Figure 3.6: Membranolytic activity of –H_2O/–O_2 gQ-f2 and +H_2O/–O_2 gQ-f2 stored in different ageing environments. Milling and ageing environment reported on the right. The x-axis is reported in log_{10} to visually enhance the differences in activity. Experiments at different time points were repeated twice to confirm the results.

We previously described that –H_2O/–O_2 and +H_2O/–O_2 quartz had opposite behaviors when exposed to water vapor (+aeH_2O at t=1day, see previous paragraph). The –H_2O/–O_2 +aeH_2O became membranolytic right after the very first exposure to water (light blue line). Sample activity immediately reached a plateau, with non-relevant variations due to the various lots of sheep blood used over time. As expected, the quartz aged in water-free environment (–H_2O/–O_2 −aeH_2O) did not exhibit any relevant hemolytic activity up to 1 year (dark grey line). The kinetics of hemolytic activity of quartz milled in water-rich and aged in water-free environment (+H_2O/–O_2 −aeH_2O) also showed a negligible activity up to 1 year. Intriguingly, the

hemolytic activity of quartz milled and aged in water-rich environments (+H_2O/–O_2 +aeH_2O) was negligible up to 40 days. However, after that time point, the hemolytic activity of the sample increased steadily up to 15% after 1 year (dark blue line, Figure 3.6). This long-term experiment confirmed the crucial role of water vapor in altering the properties of milled quartz surfaces and pointed out that quartz milled in different external environments are stabilized differently, in a fashion that is related to the presence or absence of water vapor in the milling environment. Quartz milled in water-free environment immediately becomes hemolytic as soon as it is contacted by water vapor (and not liquid water). Once activated, quartz remains hemolytic for months after milling. Quartz milled in water-rich environment slowly react with water vapor and a moderate membranolytic activity is progressively acquired a few weeks after milling.

With this study we concluded that the milling environment and the milling process is crucial in defining the surface properties of the freshly milled quartz, but the prolonged exposure to water vapor can further activate fractured surfaces, even months after milling. Independently from the milling environment, quartz aged in water-free environment remains non-hemolytic for months after milling. The behavior of these two quartz samples is also in good accordance with their radical profiles (Figure 3.1A). The –H_2O/–O_2 is characterized by a strongly reactive surface, able to immediately interact with water vapor and oxygen, while the +H_2O/–O_2 presented a low amount of radical species, with a surface stabilized by the action of water vapor during milling, and not easily reactive toward water vapor (Paragraph 3.3.2.1). The reactivity of these two samples with water vapor after milling and the related activation towards red blood cells is thus strongly linked with the milling environment and to the surface sites generated and stabilized during milling.

3.3.5 Membranolytic activity of industrial quartz dusts is not influenced by mild ageing conditions.

In the previous paragraph the influence of the milling and ageing environments was analyzed on our model quartz samples (synthetic quartz, gQ, and highly pure mineral quartz, mQ). Water vapor emerged as the crucial molecule able to modify quartz surface and alter its activity towards cellular membranes. Starting from these grounds, we shifted our attention from model quartz to industrial quartz dust obtained by project partners. The aim of this investigation was to challenge the hypothesis that freshly fractured quartz dust is more toxic than aged dust [31]. The rationale behind this hypothesis derives from the observation that workers who are exposed to freshly fractured quartz dust (*e.g.,* mine workers or workers that cut, polish quartz-rich materials) are more subjected to silicosis than workers who use

aged quartz as a raw material. Nevertheless, among those latter a relevant number of cases of silicosis is also observed and the origin of this discrepancy remains unclear. We speculated that the surface reconstruction process could play a role in the onset of the toxic potency. For this purpose, two freshly fractured quartz dusts were aged in several environments up to 9 months and checked for their hemolytic activity. Table 3.2 reports the principal chemical characteristics of industrial quartz dusts.

Table 3.2: principal characteristics of industrial quartzes, here labeled as iQ-1 and iQ-2. Min-U-Sil5 is added for comparison.

Industrial sample	SSA (m^2/g)‡	Av. particle size in PBS (µm±SD)§	Hemolytic activity
iQ-1	4.4	1.23 ± 0.69	+++
iQ-2	6.3	1.49 ± 0.60	+++
Min-U-Sil5	5.0	2.04 ± 1.05	+++

‡provided by industrial partners. §measured by Dynamic Light Scattering in 10 mM PBS.

These industrial samples (iQ-1 and iQ-2) were fractured in two different industrial plants and sent to our laboratory two weeks after milling. The hemolytic activity was checked and both resulted highly active toward RBC, in good accordance with values reported by Min-U-Sil5, which was used here for comparison. It is worth noting that iQ-1 and iQ-2 were produced in a totally uncontrolled environment and with an industrial set up completely different from the lab-scale mill used in the previous paragraph. We can speculate that the mechanism of milling and the milling atmosphere were able to render the surface hemolytic.
The two industrial dusts have been then divided in 5 lots and stored in different ageing environments differing for their water content:

1. As milled - A non-controlled environment (lab air)
2. Zero p_{sat} (Argon glove box – p H_2O = 0 mbar)
3. Low p_{sat} (T= -20°C, p H_2O = 1.0 mbar)
4. Mid p_{sat} (T= RT, p H_2O = ca. 23-30 mbar)
5. High p_{sat} (T= 70°C, p H_2O = ca. 300 mbar)

Our hypothesis is that by modulating the amount of water vapor present in the ageing environment we get different surface reconstructions and in consequence variations of the activity toward cell membranes.
For each of the five ageing environments, the evolution of the hemolytic activity of the two industrial dusts at different time points is reported in

Figure 3.7. No significant differences were observed in the hemolytic activity of these dusts, which remained almost unaltered despite the different ageing conditions. These data led to the conclusion that quartz dusts, when subjected to mechanical fracturing in industrial settings, exposed a rather stable surface, due to some mechanical or environmental peculiarity of the process.

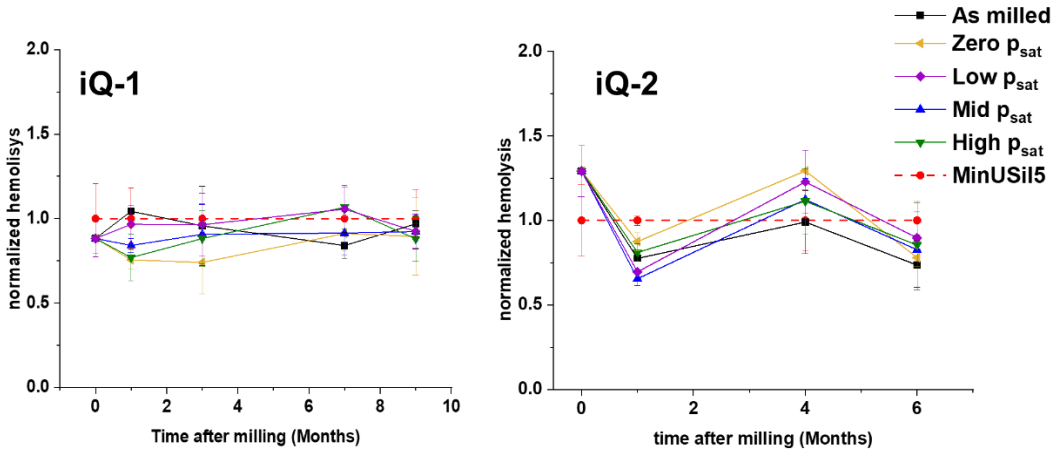

Figure 3.7: normalized hemolytic activity of iQ-1 and iQ-2 at different time points. The 100 cm^2/ml was selected for this kinetics and was normalized in comparison with the 100 cm^2/ml dose of Min-U-Sil5 (whom activity toward RBC is considered constant and was assigned the value 1). The normalization was necessary to avoid evident fluctuations of hemolytic activity due to different sheep blood lots. Every experiment was replicated twice to confirm the results.

It is worth noting that the chemical stability of the surface towards water does not imply an inert surface towards cell membrane. This is consistent with the NFS model proposed for these kind of interactions. Once NFS are formed on the silica surface, low-energetic processes such as the exposure to water vapor at RT cannot modify the structural arrangement of those silanol pairs.

3.3.6 Hydrofluoric acid (HF) can alter the membranolytic activity of iQ-1.

Industrial quartz dusts appeared to be not influenced by mild ageing environments because of the stability of the fractured surface obtained after the fracturing process. Harsher treatments were carried out to stimulate possible alteration of the quartz surface and in turn promote an inactivation of quartz dust. Aqueous solution of hydrofluoric acid (HF) was contacted with a suspension of iQ-1. After the contact, quartz was repeatedly washed, dried, and analyzed for hemolytic activity.

Results are reported in Figure 3.8. After 10 minutes of treatment with HF the hemolytic activity of iQ-1 was visibly reduced from 30% to 10%. No further reduction of the activity was induced by longer times of contact with HF (20 and 30 min). It is largely held that HF can dissolve outermost quartz surface layers and remove surface impurities and defects. [9, 30] In fact, HF can promote the dissolution of the outer layers, by dissolving firstly the amorphous layer which covers the surface of milled quartz. This process may also bring to the exposure of the underneath crystalline layers. [32-34] This data show that by removing the amorphous layer on the surface of milled quartz, the hemolytic activity decreases. This is consistent with the NFS occurrence in the quasi-amorphous layer generated during milling and imparting the membranolytic potential of crystalline silica dust.

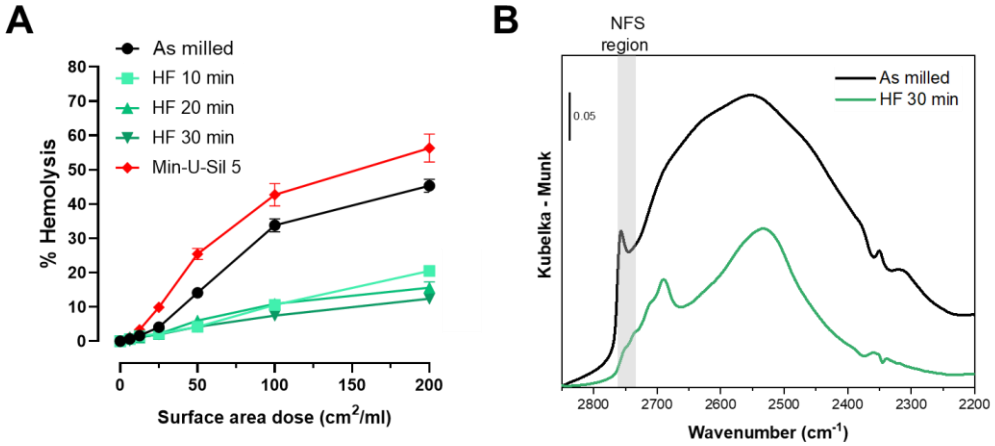

Figure 3.8: treatment of iQ-1 with HF. (A) Hemolytic activity of iQ-1 as milled (black curve) and after treatment with HF for 10, 20 and 30 minutes of treatment. Results are compared with Min-U-Sil5 membranolytic activity. (B) IR spectra of the silanol profile of iQ-1 as milled and after treatment with HF. Nearly free silanol band in grey to highlight the decrease in intensity of the peak.

To evidence the presence of NFS on iQ-1 surface, IR spectroscopy was carried out on iQ-1 before and after HF treatment (Figure 3.8B). The NFS band (2757 cm^{-1}) is clearly visible on the pristine iQ-1 sample and can be considered the causal molecular agent for the membranolytic activity of the sample (Paragraph 1.4). After HF treatment, the intensity of the NFS band is visibly decreased, consistently with the lower membranolytic activity observed. Furthermore, the silanol profile is also altered. The broad band due to several families of mutually interacting silanols with superimposed vibrational features and typically observed on milled quartz is replaced by two narrower bands at 2690 and 2530 cm^{-1}. These bands may signal that HF treatment lowered the number of interacting silanol families and can be reconducted to

a more order surface, typical of crystalline solids exposing unaltered portions of regular crystallographic planes. A similar OH profile was indeed observed for the synthetic quartz with as-grown surface, used in previous investigations. [3, 35] Still to investigate remains the fluorination degree of the surface of quartz. According to the IR analysis, only the alteration of surface silanols is observed, but further analyses need to be performed.
In conclusion, strong chemical treatments, such as HF dissolution, can alter the surface of milled quartz and modify the membranolytic potential of crystalline silica dusts. Such treatments are not industrially relevant but open up perspective for a possible approach to alter the silanol population on quartz and reduce or suppress its membranolytic activity and inflammogenic potential.

3.4 Main Achievements

The central core of this Chapter is the investigation of the different surface reconstruction pathways that can be obtained by modulating milling and ageing environment of quartz dust. When quartz is fractured, the Si–O bond breaks, generating active sites able to react with molecules that are present in the environment, such as molecular oxygen and water vapor. We challenged the hypothesis that by varying the molecules present in those environments, we could obtain different surface reconstruction pathways and finally quartz dust with different membranolytic activity. The reconstruction of the surface plays a crucial role in the activity of quartz particles towards biomembranes. In fact, quartz becomes membranolytic only when fractured, generating a specific silanol family called nearly free silanol (NFS). NFS are held responsible for the silica-induced lysis of biomembranes. [35, 36].
Starting from these grounds, we selected two model quartz samples, one of synthetic origin and one of mineral origin, and milled them in different environments, deprived of oxygen, water, or both. EPR spectroscopy was used to check the amount and the type of radical species generated during milling, and to verify if the surfaces obtained after milling were exposing different surface radical sites. We showed that molecular oxygen in the milling environment favor the formation of oxygen-centered radicals. Furthermore, water vapor visibly lowered the amount of radicals that are present on the surface, by favoring the recombination of active sites into neutral species (not detectable by EPR). Stability of radical species was also assessed, highlighting a different stability of radical species generated in different milling environments.

The membranolytic activity of these model quartzes fractured in different milling environments was also assessed (Figure 3.9), revealing that all four different environments generated inactive surfaces toward red blood cells.
Even if the membranolytic outcome is the same, the reactivity of the surfaces is different. Quartzes milled in water poor environments, once exposed to water vapor, immediately reacted with water vapor, possibly generating nearly free silanols (NFS), which interacted with RBC. Conversely, quartz milled in water-rich environments became membranolytic only after months of exposure to water vapor (slowly arrow, in Figure 3.9). The ageing in water-free environment did not alter the membranolytic activity at all. This part of the study confirmed the pivotal role of water vapor in the alteration of the surface reconstruction and in the creation of NFS.

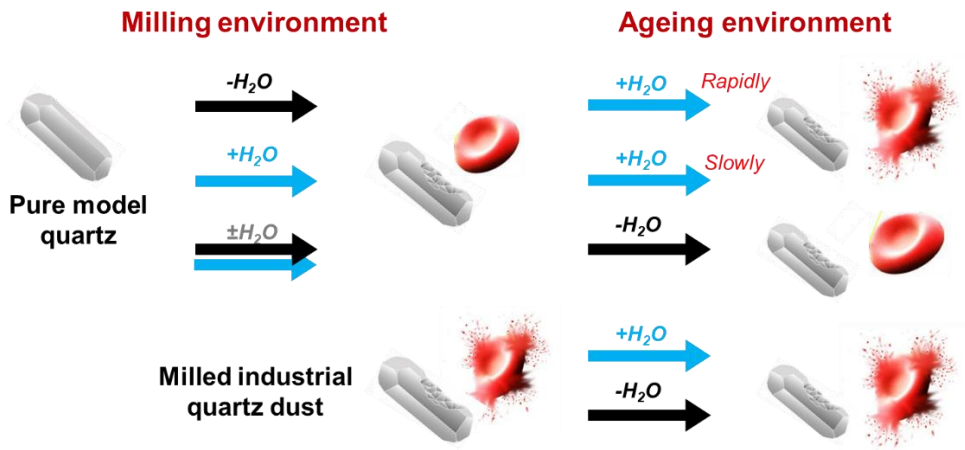

Figure 3.9: summary scheme of milling and ageing conditions applied on pure model quartzes and on industrial quartzes and their effect on membranolysis of RBC.

The study was then shifted from model quartzes to industrial quartz dusts. Two highly membranolytic quartz dusts freshly fractured in an uncontrolled industrial setting have been stored in five ageing environments with a variable concentration of water vapor (from 0 mbar to ~30 mbar of H_2O_{vap}). By far, no significative alteration of the membranolytic activity was observed. This is in good agreement with the system optimized with model quartzes, because water vapor activated fractured surfaces, but no deactivation was observed. Moreover, this is a sign of the stability of the surface of quartz dusts because a deactivation of the surface was not observed even months after milling. It is safe to say that when the surface of quartz reaches an energetic stability mild ageing conditions impart negligible changes on the distribution of active sites able to interact with biomembranes.
Conversely, strong chemical treatments, *e.g.*, HF leaching, are able to alter the surface activity of industrial quartz flours, and this alteration was also

paralleled by a modification of the silanol profile and the presence of NFS. Thus, we can conclude that the membranolytic potential of quartz dusts do not seem to spontaneously decline after milling.

3.5 Bibliography

1. IARC, *Silica dust, crystalline, in the form of quartz or cristobalite*, in *Arsenic, Metals, Fibres and Dusts*. 2012, International Agency for Research on Cancer.
2. IARC, *Silica, some silicates, coal dust and para-aramid fibrils*. Vol. 68. 1997: World Health Organization.
3. Turci, F., et al., *Revisiting the paradigm of silica pathogenicity with synthetic quartz crystals: the role of crystallinity and surface disorder.* Particle and Fibre Toxicology, 2016. **13**(1): p. 32.
4. Pavan, C., et al., *Nearly free surface silanols are the critical molecular moieties that initiate the toxicity of silica particles.* Proceedings of the National Academy of Sciences, 2020. **117**(45): p. 27836-27846.
5. Rimola, A., et al., *Silica surface features and their role in the adsorption of biomolecules: computational modeling and experiments.* Chemical reviews, 2013. **113**(6): p. 4216-4313.
6. Donaldson, K. and P.J. Borm, *The quartz hazard: a variable entity.* The Annals of occupational hygiene, 1998. **42**(5): p. 287-294.
7. Stoll, S. and D. Goldfarb, *EPR spectroscopy: fundamentals and methods*. 2018: John Wiley & Sons.
8. Roessler, M.M. and E. Salvadori, *Principles and applications of EPR spectroscopy in the chemical sciences.* Chemical Society Reviews, 2018. **47**(8): p. 2534-2553.
9. Fubini, B., et al., *Chemical functionalities at the silica surface determining its reactivity when inhaled. Formation and reactivity of surface radicals.* Toxicology and industrial health, 1990. **6**(6): p. 571-598.
10. Griscom, D.L., *Trapped-electron centers in pure and doped glassy silica: A review and synthesis.* Journal of Non-Crystalline Solids, 2011. **357**(8-9): p. 1945-1962.
11. Arienzo, R. and E. Bresciano, *Attivita litica di una silice amorfa submicronica su aritrociti di diverse specie animali.* Rcrss. Med. Sper, 1969. **16**: p. 135-141.
12. Arends, J., A. Dekker, and W. Perdok, *Color centers in quartz produced by crushing.* physica status solidi (b), 1963. **3**(12): p. 2275-2279.
13. Fubini, B., et al., *The formation of oxygen reactive radicals at the surface of the crushed quartz dusts as a possible cause of silica pathogenicity*, in *Effects of mineral dusts on cells*. 1989, Springer. p. 205-214.

14. Hochstrasser, G. and J. Antonini, *Surface states of pristine silica surfaces: I. ESR studies of Es' dangling bonds and of CO2− adsorbed radicals.* Surface Science, 1972. **32**(3): p. 644-664.
15. Stapelbroek, M., et al., *Oxygen-associated trapped-hole centers in high-purity fused silicas.* Journal of Non-Crystalline Solids, 1979. **32**(1-3): p. 313-326.
16. Griscom, D.L. and E.J. Friebele, *Fundamental defect centers in glass: $^{29}\mathrm{Si}$ hyperfine structure of the nonbridging oxygen hole center and the peroxy radical in a-Si${\mathrm{O}}_{2}$.* Physical Review B, 1981. **24**(8): p. 4896-4898.
17. Radtsig, V. and A. Bystrikov, *ESR STUDY OF CHEMICALLY ACTIVE-CENTERS ON THE SURFACE OF QUARTZ.* KINETICS AND CATALYSIS, 1978. **19**(3): p. 563-568.
18. Fubini, B., et al., *Mechanically induced defects in quartz and their impact on pathogenicity.* Solid State Ionics, 1989. **32**: p. 334-343.
19. He, H., et al., *An abiotic source of Archean hydrogen peroxide and oxygen that pre-dates oxygenic photosynthesis.* Nature communications, 2021. **12**(1): p. 1-9.
20. Edwards, A.H. and W.B. Fowler, *Theory of the peroxy-radical defect in a-Si${\mathrm{O}}_{2}$.* Physical Review B, 1982. **26**(12): p. 6649-6660.
21. Fukuchi, T., *A mechanism of the formation of E' and peroxy centers in natural deformed quartz.* Applied radiation and isotopes, 1996. **47**(11-12): p. 1509-1521.
22. Fukuchi, T., *Vacancy-associated type ESR centers observed in natural silica and their application to geology.* Applied Radiation and Isotopes, 1993. **44**(1-2): p. 179-184.
23. Turci, F., et al., *Revisiting the paradigm of silica pathogenicity with synthetic quartz crystals: The role of crystallinity and surface disorder.* Particle and Fibre Toxicology, 2016. **13**(1).
24. Rignanese, G.-M., J.-C. Charlier, and X. Gonze, *First-principles molecular-dynamics investigation of the hydration mechanisms of the (0001) α-quartz surface.* Physical Chemistry Chemical Physics, 2004. **6**(8): p. 1920-1925.
25. de Leeuw, N.H., F.M. Higgins, and S.C. Parker, *Modeling the surface structure and stability of α-quartz.* The Journal of Physical Chemistry B, 1999. **103**(8): p. 1270-1277.
26. Costa, D., et al., *A novel type of active site at the surface of crystalline SiO2 (a-quartz) and its possible impact on pathogenicity.* Canadian journal of chemistry, 1991. **69**(9): p. 1427-1434.

27. Radtsig, V., *456: 20 (1979) 1203.[l 5] IV Berestetskaya. AV Bystrikov, AN Streletskii and P. Yu. Butyagin.* Kinet. Katal, 1980. **121**: p. 1019.
28. Bonelli, B., et al., *Study of the surface acidity of TiO2/SiO2 catalysts by means of FTIR measurements of CO and NH3 adsorption.* Journal of Catalysis, 2007. **246**(2): p. 293-300.
29. Lednor, P.W. and P.C. Versloot, *Radical-anion chemistry of carbon monoxide.* Journal of the Chemical Society, Chemical Communications, 1983(6): p. 284-285.
30. Pavan, C., et al., *Why does the hemolytic activity of silica predict its pro-inflammatory activity?* Particle and fibre toxicology, 2014. **11**(1): p. 1-11.
31. Vallyathan, V., et al., *Response of alveolar macrophages to in vitro exposure to freshly fractured versus aged silica dust: the ability of Prosil 28, an organosilane material, to coat silica and reduce its biological reactivity.* Journal of Toxicology and Environmental Health, Part A Current Issues, 1991. **33**(3): p. 303-315.
32. Bell, W. and D. Zimmerman, *The effect of HF acid etching on the morphology of quartz inclusions for thermoluminescence dating.* Archaeometry, 1978. **20**(1): p. 63-65.
33. Kilday, M.V. and E.J. Prosen, *The enthalpy of solution of low quartz (α-quartz) in aqueous hydrofluoric acid.* Journal of Research of the National Bureau of Standards. Section A, Physics and Chemistry, 1973. **77**(2): p. 205.
34. Duval, M., et al., *Quantifying hydrofluoric acid etching of quartz and feldspar coarse grains based on weight loss estimates: implication for ESR and luminescence dating studies.* 2018.
35. Pastero, L., et al., *Synthesis of α-quartz with controlled properties for the investigation of the molecular determinants in silica toxicology.* Crystal Growth & Design, 2016. **16**(4): p. 2394-2403.
36. Turci, F., et al., *Revisiting the paradigm of silica pathogenicity with synthetic quartz crystals: the role of crystallinity and surface disorder.* Particle and fibre toxicology, 2015. **13**(1): p. 1-12.

CHAPTER 4: Physicochemical characteristics of fractured nanoquartz

4.1 Background

Fractured respirable silica particles of micrometric size are considered responsible for several pathologies, such as silicosis, lung cancer and autoimmune diseases. Industrial processing, such as milling, sandblasting, cutting and polishing induce the fracturing of crystalline silica particles down to a respirable size (aerodynamic diameter of ≤5µm). [1, 2] However, mechanical processes are not characterized by an homogeneous reduction of the size, meaning that there is not a complete control over the size of the generated particles. It is often observed on fractured quartz of industrial origin the presence, along with micrometric particles, of a fraction of submicrometric/nanometric particles, which in general adhere on the surface of the micrometric ones, probably because of electrostatic forces (Figure 4.1).[3, 4]

The presence of this nanofraction is visible with electron microscopies, but even if micrometric particles have been studied for decades until now, very little is known about this nanometric fraction. This lack of knowledge is related both to its physicochemical properties and to its toxicological impact on the overall toxicity of silica. One of the reasons of this lack of information is the negligible amount of the nanometric fraction on the overall dust. However, even if the quantity of the nanoparticles is low compared to the total weight of the dust, the nanometric particles can outnumber the micrometric ones, generating a nanomaterial according to the European Commission latest recommendation. [5] In the document, a material is considered a nanomaterial when >50% of the particles have a diameter smaller than 100 nm on a per number basis. Moreover, when the size of the

particles decreases, other factors increase, such as surface area and surface active sites. [6, 7]

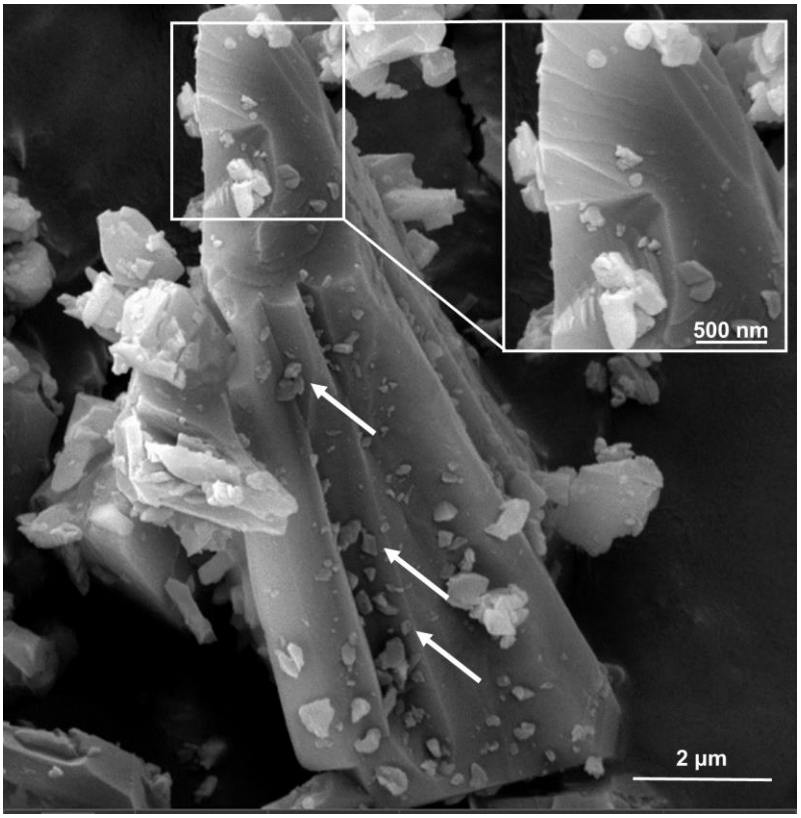

Figure 4.1: SEM micrograph of Min-U-Sil5. Nanometric particles (highlighted by the white arrows) adhere on the surface of the micrometric particle.

The reactivity of such small particles can be dramatically different than bigger ones. Auffan and co-workers [8] in their review proposed 30 nm as the size threshold in which a nanoparticle change its reactivity, because the atoms present on the surface drastically increase with respect of the bulk ones. This leads to an increase of the surface free energy that need to be compensated by crystallographic changes (lattice contraction and deformation, appearance of defects, etc.) with consequent increase of the surface reactivity. For these reasons it is not possible to exclude that nanometric crystalline silica particles are able to interact with the external environment differently than the micrometric ones, including the interaction with biomolecules. The French Agency of Food, Environmental and Occupational Health and Safety (ANSES) recently raised their concern about the possible role of nanosilica in the toxic activity of RCS. [9]

A recent review on the pulmonary toxicity of silica evidenced the general lack of a solid investigation on nanoquartz health effects. [10] This is due mostly to the difficulty in obtaining a quartz dust of nanometric size. In particular, the authors were able to find only one study on nanoscale and fine-quartz particles in rats. [11] Warheit and coworkers challenged the hypothesis that nanometric particles are more hazardous than micrometric particles of the same compound, but the study used a synthetic quartz prepared with a bottom-up approach. Generally, nanometric quartz particles are obtained by using a top-down approach, such as ball milling, drilling and polishing. As this nanoquartz was obtained through hydrothermal crystal growth, we can assume that the surface properties are not nearly as similar to the nanometric fraction of a fractured nanoquartz. As already anticipated in the introduction, in fact, synthetic quartz has an ordered surface far from a fractured surface rich of active sites and different silanol families, and it is not the crystallinity *per se* the feature able to trigger inflammation in the lung, but the nearly free silanols present on a disordered fractured surface. [12, 13]

Mischler and coworkers, on the other hand, were able to segregate the finest fraction of a commercial quartz flour using a multi-cyclone sampling array, but their approach relied on the availability of large quantities of quartz dust, which introduced uncertainties for the purity, crystallinity, and occurrence of the accessory mineral phases that are always present in natural samples.[14] For this reason, before analyzing real life quartz flours it is fundamental to resort to quartzes of high purity, to study the characteristics related to the material, without interference from secondary factors.

A few other studies tried to address the effect of size on the toxicity of crystalline silica, [15-17] but none of them detailed the production method or the physicochemical bulk and surface characteristics of the nanosilica.

For all these reasons, in this work a ball milling approach on a synthetic micrometric quartz was selected. [18] The use of a model synthetic quartz is due to the high purity of the sample and to its well documented chemical characteristics. The ball milling approach, on the other hand, was selected to be similar to the top-down industrial approaches on the manipulation of quartz. Obviously, the lab scale ball milling is not completely comparable with the industrial operations but can be considered the best approach to obtain a nanoscale quartz to study its properties.

For these reasons, a highly pure synthetic quartz in micrometric size, well-characterized in previous works, was ball milled in dry and wet conditions, incrementing the milling times and rotational speeds, to obtain a nanometric quartz. The production of the nanoquartz has been already reported in Paragraph 2.3.3. Particle and crystallite size distributions, crystalline/amorphous ratios, surface NFS numbers, and membranolytic

activities were measured for all the samples and compared with the pristine materials. Moreover, the agglomeration and deagglomeration mechanisms were investigated for the dispersion/separation behavior of quartz nanoparticles.

4.2 Materials and Methods

4.2.1 Synthetic quartz (gQ) synthesis and ball milling

This part was already detailed in Chapter 2.

4.2.2 Crystallinity

Crystallinity of nanometric particles was checked by High Resolution Transmission Electron Microscopy (HR-TEM) analysis of the particles dispersed and deposited on a Cu grid as described above. The instrument used was a Philips Tecnai G2 20 microscope, with a LaB_6 source, operating at 200 keV.

4.2.3 Particle dispersion and size analysis

Analysis of the hydrodynamic diameter of the particles was performed by Differential Centrifugal Sedimentation (DCS, DC24000, CPS Instruments, Inc.) to reveal differently sized subpopulation of particles in each sample. gQ-f3 and gQ-n suspensions (1 mg/ml) were bath sonicated for 15 minutes (35kHz, ELMASONIC S10H) and probe sonicated 3 minutes (35% amplitude, pulse 0.5 s, UP200S, Hielscher) right before the injection. For the DCS analysis, a gradient of sucrose between 2% and 8% was used, adding 0.1 ml of dodecane as stabilizer. The instrument was calibrated with a polyvinyl chloride latex standard with diameter of 0.263 μm before sample injection. Disc speed used during the analysis was 8000 rpm for gQ-ff and 11000 rpm for gQ-n samples. Analysis of the disaggregation behavior of the gQ-n samples was assessed by Dynamic Light Scattering (DLS) using a Zetasizer Nano ZS (Malvern Instruments, UK) instrument. To evaluate possible disaggregation of the nanoquartz particles in aqueous biological-relevant media, particles were dispersed in phosphate buffered saline (PBS, 10 mM, pH 7.4), artificial phagolysosome fluid (ALF, pH 4.5),[19] bovine serum albumin (BSA, 2.5mg/ml), and with surfactants. Triton X (TRX) and dioctyl sulfosuccinate sodium salt (AOT) were used at concentrations under their critical micellar concentration (CMC), respectively 0.16mM and 1 mM. gQ-n samples were suspended in the dispersing agent (1 mg/ml) and bath sonicated (FALC instruments) for 15 minutes. The suspension was diluted 1:10 with the corresponding dispersing agent, and probe sonicated (amplitude 30%, 40 W,

Sonoplus HD 3100, Bandelin) on ice for 5 minutes before the analysis. Moreover, an aliquot of gQ-n was filtered with cellulose acetate 220 nm-pores filter in ultrapure water and its size analyzed after sonication. PBS, AOT, TRX and BSA were purchased by Sigma Aldrich (Merck) without further purification. ALF components were also purchased by Sigma Aldrich and mixed in ultrapure water, and the pH checked after complete dissolution of all the salts.

4.2.4 IR spectroscopy

The FTIR spectra of the different quartz samples were recorded in transmission mode at beam temperature (b.t.; ca. 50 °C), using a Bruker INVENIO R spectrometer equipped with a DTGS detector at a resolution of 4 cm^{-1}. The number of scans was adjusted to 64 to obtain a good signal-to-noise ratio. The powders of the silica samples were pressed into self-supporting pellets and placed in an IR quartz cell equipped with CaF_2 windows. The cell was attached to a conventional vacuum line (residual pressure, ≤ 1 x 10^{-3} mbar) to perform in situ the adsorption-desorption experiments. To analyze only the surface silanols without interferences of the bulk species, the samples were submitted to a H/D isotopic exchange to convert the pristine SiOH into SiOD species by contact with heavy water vapors (D_2O, Sigma-Aldrich; 99.90% D). The detailed H/D isotopic exchange protocol has been previously described.[13, 20] Briefly, the samples were outgassed at b.t. for 120 min. Then, the samples were put in contact with D2O vapors at b.t. (ca. 20 mbar) for 15 seconds and subsequently outgassed for 1 minute. This step was repeated until spectral invariance. Finally, the samples were outgassed at b.t. for 120 minutes. The collected spectra of the different samples were normalized to both the intensity of the pattern in the 1720-2100 cm^{-1} region due to the bulk modes of silica and the SSA. This allowed, on one hand, to render differences in intensity independent of differences in the thickness of the pellets, and, on the other hand, to perform a comparative analysis of the intensity of surface species.
IR measurements were performed by prof. Lorenzo Mino's group.

4.2.5 Membranolysis assay

To assess the membranolytic activity of the particles, red blood cells (RBCs) were used as simple model of non-phagocytic cells, using a protocol described in the previous chapters. Samples were dispersed at the initial concentration of 6 mg/ml in 10mM PBS and bath sonicated for 15 minutes (FALC instruments), just before testing. Serial dilutions of the starting dispersion were performed according to the final doses used for experiments.

4.2.6 Statistical Analysis.

Statistical parameters, including the number of independent experiments and statistical significance, are reported in the figures and figure legends. Unless otherwise stated, data are mean ± s.d. (standard deviation) of three independent experiments. Normally distributed data were analyzed by two-way ANOVA followed by Tukey's post hoc test. A 95% confidence interval was used. Differences with $P < 0.05$ were considered statistically significant. Statistical analysis was performed with the GraphPad Prism 9 software.

4.3 Results and Discussion.

In Chapter 2, Paragraph 3.3 the ball milling protocol, the morphology and the XRD profile of the samples have been assessed, together with the possible comminution mechanism.
Three ultrafine samples of quartz have been generated by a two-step ball milling. The SSA and crystallinity, investigated in Chapter 2, are reported in Table 4.1.

Table 4.1: summary of the main characteristics of nanoquartzes generated by wet milling.

	Origin	SSA (m^2/g)	% of Crystallites (>100nm)*	% of crystallites (<100nm)*	% Amorphous*
gQ	synthesis	0.1			
gQ-f3	dry milled	10			
gQ-n1	wet milled‡	37	16	57	27
gQ-n2	wet milled‡	45	11	56	34
gQ-n3	wet milled‡	55	6	54	40

*calculated from XRPD diffractograms through Rietveld refinement.
‡obtained from gQ-f3

In this Chapter, the size, the agglomeration/aggregation dynamics, the behavior in biological media and the surface chemistry correlated with the membranolytic activity is investigated.

4.3.1 Size of the particles

The particle size distribution of the gQ-ns was assessed initially through Differential Centrifugal Sedimentation (DCS). The samples have been dispersed in ultrapure water and probe sonicated to obtain an homogeneous dispersion. The results are reported in Figure 4.2(A-B).
A marked reduction in the average size is visible and paralleled the milling energies applied during the ball milling in the following order: gQ-f3>gQ-n1≈gQ-n2>gQ-n3, with a modal hydrodynamic diameter of 1500, 600 and 400 nm, respectively (Figure 4.2A). The data are reported in Table 4.2.

The data analyzed on a per number basis (Figure 4.2B) show very clearly the size reduction provoked by ball milling and exhibit a great number of particles in the nanodomain.
However, the DCS data do not completely correlate with the XRPD data reported in Table 4.1. According to the Rietveld refinement, in fact, more than half of the gQ-ns are composed by crystallites smaller than 100 nm. Starting from these grounds, the expected size of the particles should have been smaller than the one obtained by DCS (Table 4.2). For this reason, a further investigation on the size of the particles has been performed.

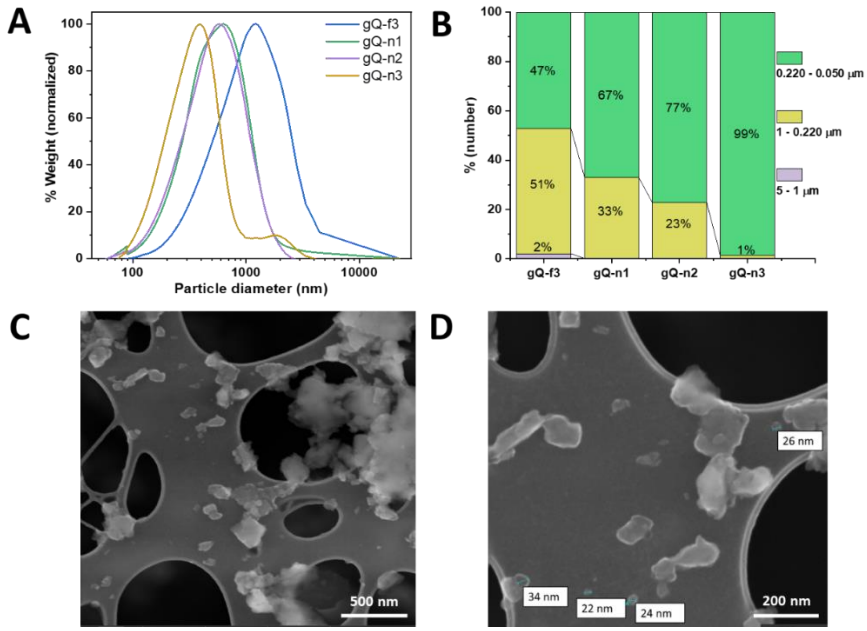

*Figure 4.2: Size distribution of the dry-milled quartz (gQ-f3) and nanoquartz samples (gQ-n1, gQ-n2, and gQ-n3) that were dispersed in water and probe-sonicated. (**A**) Size distribution of the four samples analyzed by DCS, expressed as relative wt.%. (**B**). Hydrodynamic size of the same samples expressed as relative intensity distribution. (**C**-**D**). FE-SEM micrographs of gQ-n3 dispersed in water, filtered and deposited on a Cu grid.*

Table 4.2: Particle size distribution (PSD) of the milled quartz samples that were dispersed in water, probe-sonicated, and measured by DCS, reported in normalized weight %.

	Peak (µm)	Range % (22-5.0 µm)	Range % (5.0-1.0 µm)	Range % (1.0–0.22 µm)	Range % (0.22–0.050 µm)
gQ-f3	1.45	23.1	46.37	24.75	1.17
gQ-n1	0.635	0.0	13.42	73.06	6.97
gQ-n2	0.574	0.0	12.27	76.44	10.49
gQ-n3	0.392	0.0	7.42	72.43	19.93

The nanoquartz samples, dispersed in water the same conditions, have been then analyzed with Electron Microscopies (EMs). In Figure 4.2 (C-D) are reported two FESEM micrographs of gQ-n3 dispersed in ultrapure water. FESEM analysis evidenced the presence of primary particles of a nanometric size (diameter of 20-40 nm), along with agglomerates of particles in the 200-400 nm range. This finding confirms the presence of very small primary particles, which have been hypothesized by XRPD modeling through Rietveld refinement, but could not be statistically detected by DCS. Even though the presence of primary isolated particles confirms the small size of these finely fractured samples, as was anticipated by the high SSA, it appears clear that only a very small part of the gQ-n samples deagglomerates when dispersed in water, even after probe sonication.

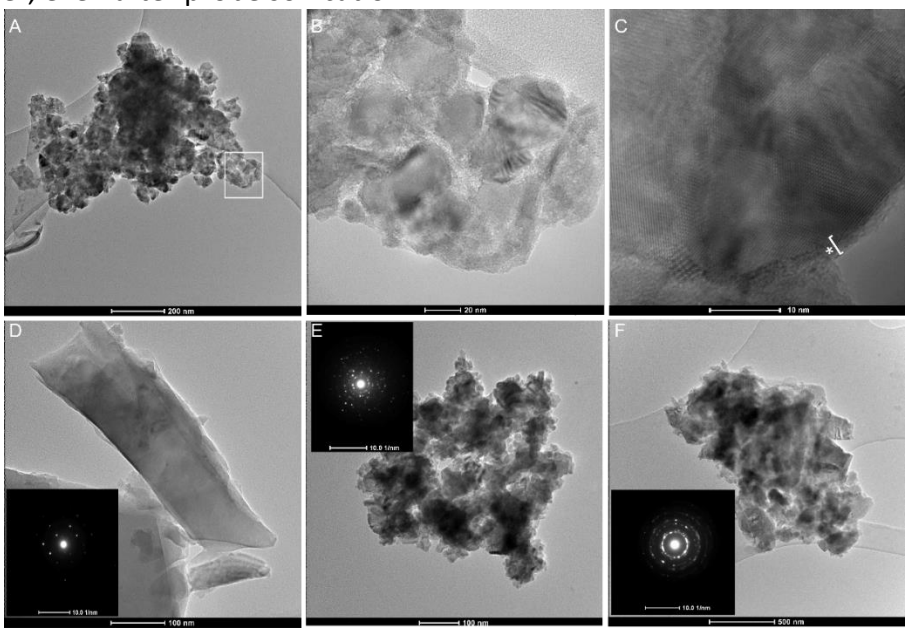

*Figure 4.3: Transmission Electron Microscopy (TEM) of gQ-n3 after dispersion in ultrapure water and probe sonication. Large agglomerates of 20-30 nm quartz nanoparticles are evidenced at low and high magnification (**A** and **B**). High-resolution image of a portion of the agglomerated quartz (**C**) highlights crystalline core, with several diffraction planes visible, and the amorphous external layer (highlighted by the asterisk) formed during high energy milling. A larger submicrometric highly crystalline quartz particle (**D**, SAED in the inset). Nanometric agglomerates of milled quartz at low magnification and their corresponding large-field SAED evidence multiple reflections and rings that indicate a nanometric size of the primary particles (**E** and **F**, SAED in the inset).*

Also TEM analysis showed a similar result, but allowed a deeper investigation. In fact, the analysis of gQ-n3 showed the presence of agglomerated nanoparticles (Figure 4.3, A-E-F) in the submicrometric range. However, the

magnifications in panel B and C show that the agglomerates are composed by very small particles, strongly held together by an amorphous layer. This detail is highlighted in Figure 4.3C, in which are visible the crystallographic fringes of the particles and the 5 nm amorphous layer which surrounds it (highlighted in Figure 4.3C by an asterisk). While this strong agglomeration is very clear with such small particles, seems to be less evident with larger submicrometric particles, in which the crystal lattice is more preserved (Figure 4.3D). When dense agglomerates of nanometric crystallites/ particles were subjected to the analysis (panels E and F, and their inset), multiple reflections and rings, due to the overlap of different oriented particles and relative lattice domains, were observed, confirming the nanometric size of gQ-n3 crystallites. Interestingly, also the distribution of the amorphous phase agrees with the literature. In fact, the most part of the amorphous phase can be considered on the surface of the smallest particles, forming the so called Beilby layer, which is an amorphous disordered layer which surrounds particles which preserve a crystalline core.[21, 22]

4.3.2 Deagglomeration behavior in liquid media.

Considering the clear tendency to agglomeration of the nanometric particles several attempts have been done to clarify their behavior in liquid media. The aim was to understand if the electrostatic forces which hold together the particles can be disrupted once the nanoquartz is dispersed in liquid media of different nature. To test the strength of interparticle forces that induces agglomeration of nanoquartz, particles were dispersed in presence of several surfactants, namely Triton X (TRX), dioctyl sulfosuccinate sodium salt (AOT), and simulated biological fluids (SBF), namely PBS pH 7.4, ALF pH 4.5, and bovine serum albumin (BSA). The hydrodynamic size was then assessed by DLS.

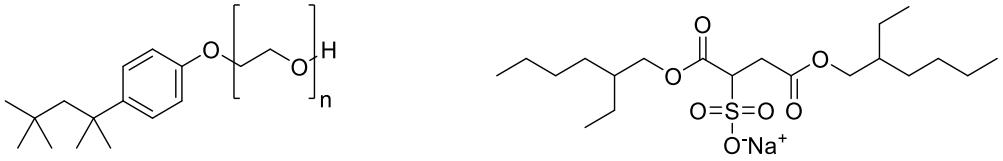

Triton-X (TRX) Dioctyl sulfosuccinate sodium salt (AOT)

Figure 4.4: chemical structure of Triton-X (TRX) and dioctyl sulfosuccinate sodium salt (AOT).

Surfactants play an important role in interfacial chemistry and are defined as chemical compounds able to decrease the surface tension or the interfacial tension between a liquid and a solid, and they generally are organic compounds (Figure 4.4). TRX and AOT, in particular, were selected for their

known ability to disperse other kinds of solid particles, such as carbon nanotubes and asbestos, and they are characterized by a different net charge. [23-25] TRX is in fact non-ionic, while AOT is an anionic salt.

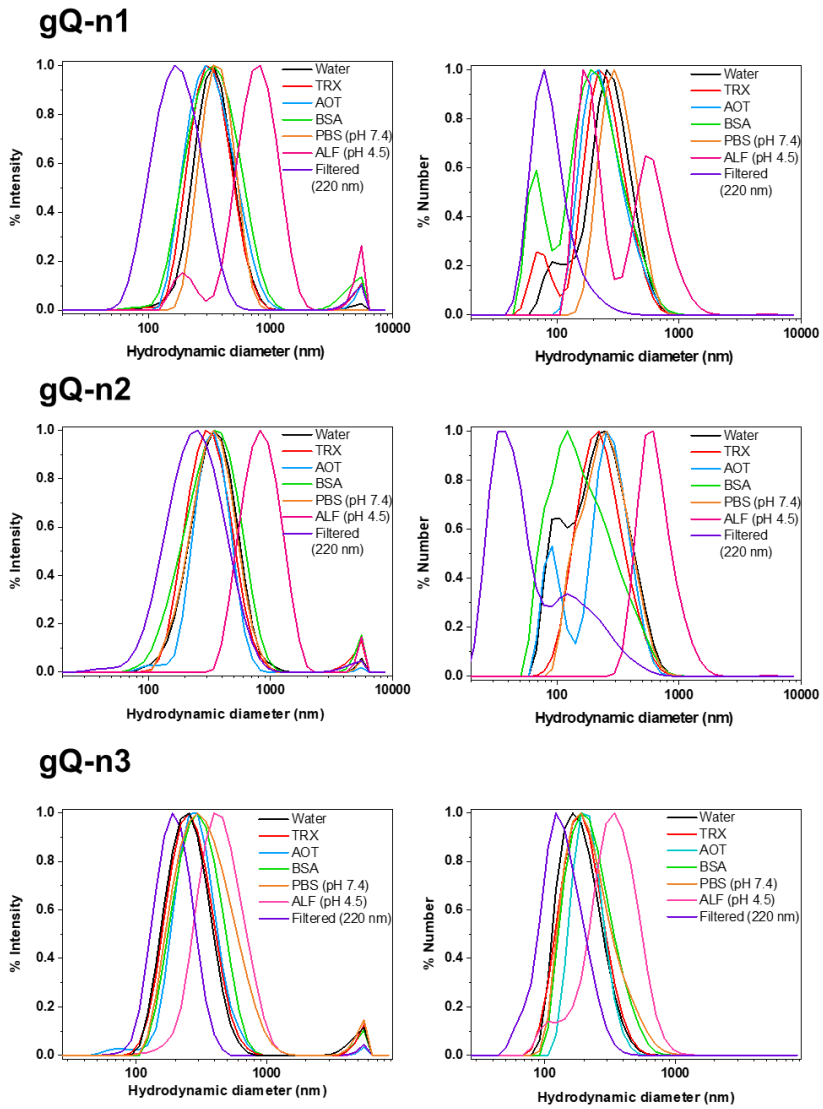

Figure 4.5: Hydrodynamic size distribution expressed as relative intensity distribution (on the left) and relative number distribution of particles (on the right) of gQ-n1, gQ-n2 and gQ-n3 dispersed in water and in different biologically relevant media i.e., Triton X (TRX), dioctyl sulfosuccinate sodium salt (AOT), bovine serum albumin (BSA), phosphate buffered saline (PBS, 10 mM, pH 7.4), artificial phagolysosome fluid (ALF, pH 4.5), and filtered through 220-nm pore size filter. The data are normalized.

Biological fluids, on the other hand, were selected according to their chemical characteristics and their occurrence and function in the pulmonary

environment. Phosphate Buffered Saline (PBS) is a buffer solution (pH ~ 7.4) commonly used in biological research. It is a water-based salt solution containing disodium hydrogen phosphate, and sodium chloride. The osmolarity and ion concentrations of the solutions match those of the human body and the buffer maintains a constant physiological pH. Bovine Serum albumin is reported to be the most common protein present on the lung lining fluid, contributing up to the 50% of the total protein concentration. [26] Finally, the Artificial Lysosomal Fluid (ALF) is representative of the more acidic environment in the lung, and its pH is acid with respect to other dispersions (such as PBS, which is at a physiological pH of 7.4).[19]

The results of these deagglomeration attempts are reported in Figure 4.5 and in Table 4.3. In general, neither surfactants or SBFs were able to deagglomerate nanoquartzes. TRX, AOT and BSA profile is overlapped on the one recorded in water (curves in black). PBS and ALF promoted on the contrary a further agglomeration of the particles (orange and pink curves). It is particularly visible the effect of the pH in the agglomeration of the particles, because it is already reported in literature that an acidic environment decreases the quartz negative surface charge and the degree of electrostatic repulsion among the particles, because an acidic pH promotes the protonation of silanol sites and reduced the electrostatic repulsion between negative charges.[27]

The only relevant attempt of deagglomeration succeeded by using a mechanical cutoff filter with pores of 220 nm and the size distribution of gQ-ns shifted toward lower hydrodynamic diameters. A smaller particle size distribution was accompanied by a significant weight loss for the sample. (Figure 4.5, purple curves).

Table 4.3: Particle size distribution of one of the nanoquartzes (gQ-n3) dispersed in biologically relevant media measured by DLS.

Medium‡	**Z-Average (nm) ± s.d. ***	**Peak (nm) ± s.d.* - Intensity**	**Peak (nm) ± s.d.* Number**
H_2O	276.2 ± 16.1	264.8 ± 14.0	198.3 ± 6.6
H_2O + TRX	280.4 ± 13.9	274.8 ± 20.7	199.0 ± 14.8
H_2O + AOT	298 ± 4.5	274.8 ± 52.9	175.9 ± 81.3
H_2O + BSA	321.6 ± 6.7	315.7 ± 16.4	238.0 ± 7.0
PBS	330.9 ± 3.2	366.9 ± 33.4	243.0 ± 2.0
ALF	435.0 ± 26.9	470.0 ± 48.8	345.2 ± 62.9
Filtered (220 nm-pores)	246.8 ± 20.7	203.0 ± 10.7	144.2 ± 19.5

*standard deviation (s.d.) calculated on two independent experiments.

‡the suspensions were probe sonicated before the DLS analysis.

Even though the presence of primary isolated particles confirms the small size of these finely fractured samples, as was anticipated by the high SSA and

observed with electron microscopies, only a very small part of the gQ-ns can be deagglomerated, suggesting that strong electrostatic interactions occur also in biological media and keep the particles agglomerated together. This suggests that the nanometric particles that adhere to the larger particles in industrial quartz dusts are easily segregated in physiological media, discouraging the idea that a big amount of the nanometric fraction can be deagglomerated after dust inhalation.

4.3.3 Nanoquartz shows NFS and Membranolytic Activity

To have a complete insight on the characteristics of nanoquartz, the surface characterization and the correlated membranolytic activity was tested.

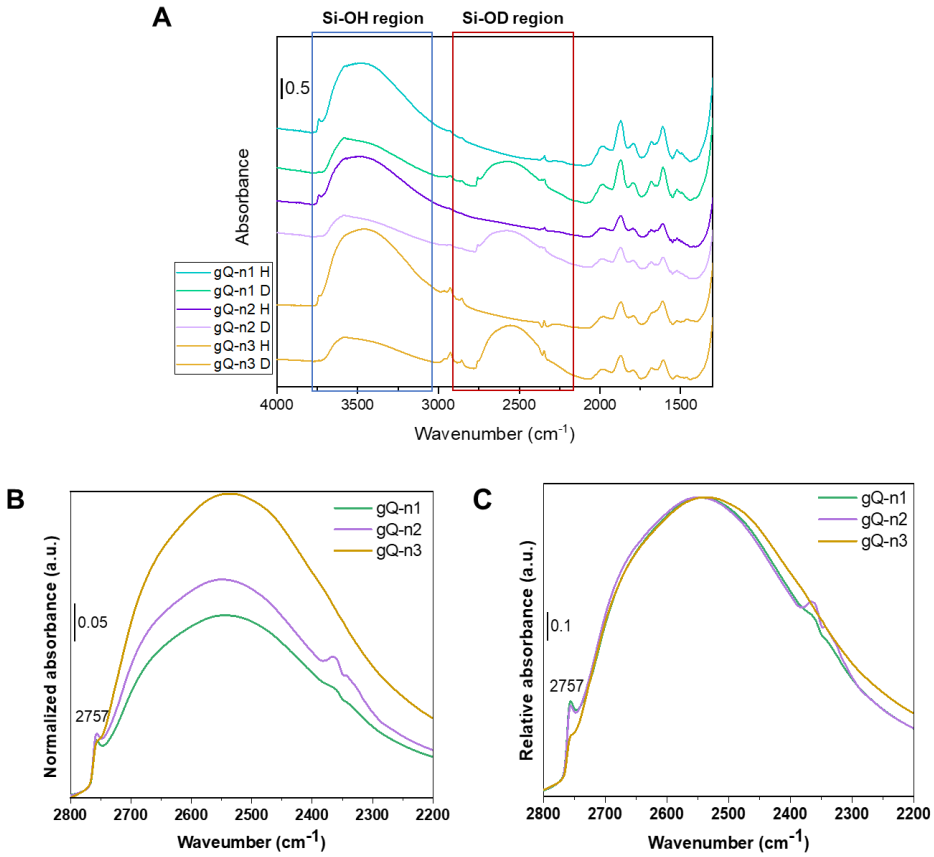

*Figure 4.6: Surface silanol distribution of nanoquartz samples (gQ-n1, gQ-n2, and gQ-n3). **A)**Transmittance FTIR spectra in the 4000-1400 cm^{-1} range were collected at beam temperature before and after H/D isotopic exchange and subsequent outgassing for 120 minutes. (vSi-OD region) **B)** magnification of FTIR spectra in the 2200-2800 cm^{-1} range (only vSi-OD region), normalized by the bulk mode and the SSA of the particles **C)** magnification of FTIR spectra in the 2200-2800 cm^{-1} range (only vSi-OD region), by the amount of interacting silanols.*

To identify the surface silanols, IR spectroscopy in transmission mode was carried out. Quartz particles pressed into self-supported pellets were submitted to an H/D isotopic exchange that allows for the analysis of the surface species without interference from the bulk species.

The results are described in Figure 4.6. In panel A is reported the full IR spectrum before and after the isotopic exchange, which highlighted the surface silanols exposed to the external surface. In panel B and C, the three nanoquartzes are normalized by SSA and interacting silanols (2550 cm^{-1}), respectively. In general, all three nanoquartzes exhibit a broad band centered at 2550 cm^{-1} which is the sum of different families of interacting silanols. [20, 28] In Figure 4.6B, the difference in intensity are related to the difference in the SSA of the samples. In all three cases, however, the narrow band at 2757 cm^{-1}, which is assigned to the nearly free silanols, was detected. [13, 29] To emphasize the differences in the silanol population, in Figure 4.6C spectra were normalized by the maximum intensity of the interacting silanol band. The intensities of the NFS band for gQ-n1 and gQ-n2 were almost superimposable. Conversely, the NFS band for gQ-n3 exhibited a relative lower intensity than the other two samples, with respect to the interacting silanols families. In the three samples, the NFS band at ca. 2757 cm^{-1}, represented about 1.6% of total silanols for gQ-n1, 1.5% for gQ-n2, and 0.6% for gQ-n3. In general, the silanol profiles observed for the gQ-n samples were qualitatively similar to the profiles observed for commercial quartz flours (*i.e.*, Min-U-Sil5) and for pyrogenic amorphous silica particles of similar size.

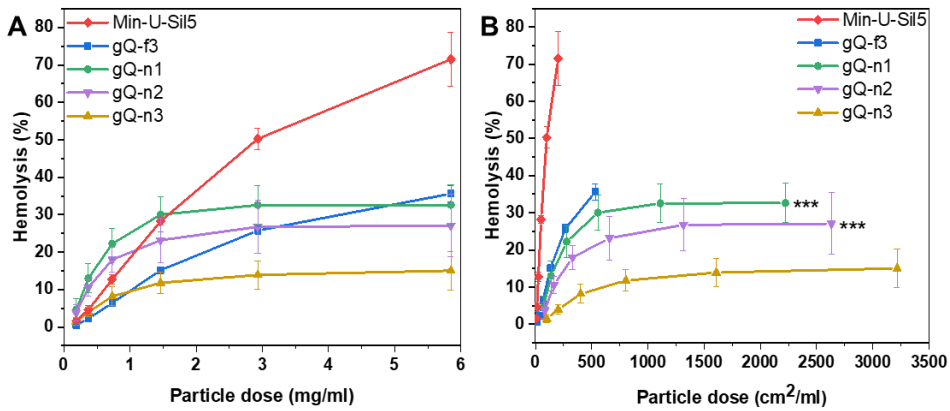

*Figure 4.7: Hemolytic activity of fine fractured (gQ-f3) and nano quartz samples (gQ-n1, gQ-n2, and gQ-n3), reported as function of the particle mass (**C**) or particle exposed surface area (**D**). A mined fractured quartz (cQ-f) was used as positive reference particle for the test. Data are mean ± s.d. of three independent experiments; P values of gQ-n1 and gQ-n2 compared to gQ-n3 determined by two-way ANOVA followed by Tukey's post hoc test (mean effect): ***P < 0.001.*

The ability of the nanoquartz particles to cause RBC membrane damage was then assessed using the hemolysis test, because membranolysis is considered as the MIE in quartz inflammation.[30, 31] In Figure 4.7, the hemolytic activity of the nanoquartz was reported as function of both particle mass (Panel A) and surface area (Panel B), and was compared with the activity of the dry milled precursor (gQ-f3) and the Min-U-Sil5 reference. When compared on a per mass basis (Panel A), gQ-f3 and nanoquartz samples were less hemolytic than Min-U-Sil5 at the highest doses, but gQ-n1 and gQ-n2 were more hemolytic than all the other samples tested at lower doses. As Min-U-Sil5 has a much lower SSA than gQ-f3 and gQ-n samples (SSA of 4.1 m^2/g), the hemolytic activity was also expressed as function of the surface area exposed (Panel B). By normalizing on the surface area dose a more linear trend was observed both at high and low doses and suggest an inverse relationship between the of surface area and the hemolytic effect, according to the following order: Min-U-Sil5 >> gQ-ff > gQ-n1 ≈ gQ-n2 > gQ-n3. For nanoquartz, this trend well correlated with the relative amount of NFS (Figure 4.6) and suggests that NFS are clearly involved in the interaction with cell membranes, as it has been already demonstrated for micrometric quartz. [13] However, the semi quantitative correlation between hemolytic activity and amount of NFS does not clearly explain why nanoquartz hemolytic effect show such a prominent plateau at relatively low concentration. Probably, each nanoquartz crystal has a finite binding capacity towards the RBC membrane that depends on the density of NFS and the contact area between quartz and RBC. In fact, assuming that the nanoquartz-RBC interaction can be reduced to a classical "contact of a sphere with a diameter D and a flat plate" problem, we can speculate that the diameter of the contact area is directly proportional to the diameter of the sphere. Hence, the lower is the quartz particle diameter, the lower is the contact area that is available to establish molecular interaction between NFS and RBC membranes. (Figure 4.8)

Furthermore, the lower is the nanoquartz diameter, the lower will be the particle mass, if we consider density constant. If we imagine that RBC membrane disrupts if a sufficient force is applied, we can speculate about an interaction model that take in consideration that, given an equal number of molecular interactions established between the membrane and the quartz, the higher is the mass of the particle, the higher deformation force will be applied on the membrane. This simplified yet practical model holds also for highly hemolytic silica nanoparticles,[32] in which the low contact area is likely compensated by the high density of NFS sites (*i.e.*, > 6% of the total silanols for pyrolytic silicas).[13]

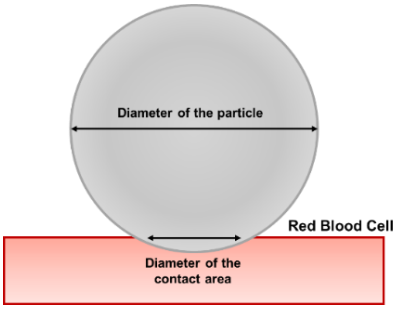

Figure 4.8: representation of the interaction between a nanoparticle (in grey) and the surface of the RBC.

4.4 Main Achievements

In this chapter, nanoquartz obtained by ball milling was studied, both in its physicochemical properties, and in its membranolytic potential. Considering that the reported literature mainly focuses on micrometric quartz, or on amorphous nanosilica, this is the first time a model quartz of high purity has been ball milled down to a nanometric size to be fully characterized. The top-down approach was crucial to mimic samples of industrial origin, but allowed to obtain a higher quantity of nanometric quartz which can be used for preliminary assessment. The aim was indeed to generate larger quantities of nanometric silica particles with a similar size range and biologically active surfaces that are comparable with industrially produced quartz dusts.
Notably, the nanoquartz samples obtained (gQ-ns) were for the most part crystalline and nanometric, according to XRPD diffraction and Rietveld refinement. The generation of an amorphous phase was anticipated, and paralleled the energy applied during ball milling. However, in all the cases, more than half of the gQ-ns were composed by crystallites with a diameter minor than 100 nm, and this characteristic included them in the nanomaterial class. [5] Moreover, it was proved that, even when subjected to high energy processes, the retention of the crystallinity is high, and it is possible to imagine that also in industrial samples, usually milled in systems with lower energies, the nanoparticles generated are for the most part crystalline. Interestingly, from EMs, it was possible to observe some primary particles around 20-30 nm, and to study the structure of some of the agglomerates. Thanks to TEM microscopy, it was clarified that these agglomerates are composed of nanometric crystals surrounded and held together by the amorphous phase, while for bigger particles, of submicrometric size and not agglomerated (Ø around 100-300 nm), the crystallinity was intact, and the amorphous phase was not detected.

With the aim of assessing the medium size of the gQ-ns, the nanoquartzes were dispersed in water and analyzed. The curves obtained with DCS showed that the size is inversely proportional to the energy applied by ball milling (gQ-n1>gQ-n2>gQ-n3). Nevertheless, the curves were broad, and their maximum was on higher values that the ones expected by their SSA, the XRPD analysis and EM micrographs. Moreover, the agglomerates were already observed with TEM. The profile suggested that the particles were organized in strong agglomerates, held together by electrostatic forces. Attempts to deagglomerate the nanoquartzes were carried out in several media, but none of them was able to successfully deagglomerate the majority of the sample. Notably, also SBFs were not able to deagglomerate, suggesting that strong agglomerates persist also in biological media when the particles are inhaled in industrial settings. Furthermore, the interparticle electrostatic forces that promote aggregation in our samples might well explain the difficulties in separating the nanometric fraction from the micrometric one in industrially generated quartz dusts. However, the strong agglomeration did not hamper the bioavailability of nanoquartz, which largely remains in the respirable size range, so their membranolytic activity was assessed and correlated with their silanol profile. Nearly free silanols were observed on the nanoquartz, and their relative number correlated well with the ability of the nanoquartz to cause red blood cell membrane lysis. The membranolytic activity was inversely correlated with the size of the particles, and also the NFS amount (gQ-n1≈ gQ-n2 > gQ-n3).

In this chapter a new feasible route for the top-down preparation of nanometric quartz with a controlled size and toxicological properties was obtained and optimized and allowed to describe the physicochemical properties of a nanometric quartz dust of high purity that is comparable with the nanometric fraction of an industrial quartz dust. Further development will use these samples as model examples to assess the relevance of nanoquartz in the overall toxic effect of crystalline silica.

4.5 Bibliography

1. Cullinan, P., et al., *Occupational lung diseases: from old and novel exposures to effective preventive strategies.* The Lancet Respiratory Medicine, 2017. **5**(5): p. 445-455.
2. Hoy, R.F. and D.C. Chambers, *Silica-related diseases in the modern world.* Allergy, 2020. **75**(11): p. 2805-2817.
3. Burmeister, C.F. and A. Kwade, *Process engineering with planetary ball mills.* Chemical Society Reviews, 2013. **42**(18): p. 7660-7667.
4. Kotake, N., et al., *Influence of dry and wet grinding conditions on fineness and shape of particle size distribution of product in a ball mill.* Advanced Powder Technology, 2011. **22**(1): p. 86-92.
5. EC, *Commission Recommendation of 10 June 2022 on the definition of nanomaterial (Text with EEA relevance) 2022/C 229/01*. 2022. p. 1-5.
6. Kim, W., et al., *A reliable approach for assessing size-dependent effects of silica nanoparticles on cellular internalization behavior and cytotoxic mechanisms.* International Journal of Nanomedicine, 2019. **14**: p. 7375-7387.
7. Napierska, D., et al., *Amorphous Silica Nanoparticles Promote Monocyte Adhesion to Human Endothelial Cells: Size-Dependent Effect.* Small, 2013. **9**(3): p. 430-438.
8. Auffan, M., et al., *Towards a definition of inorganic nanoparticles from an environmental, health and safety perspective.* Nature nanotechnology, 2009. **4**(10): p. 634-641.
9. ANSES, *OPINION of the French Agency for Food, Environmental and Occupational Health & Safety on "Updating knowledge on the hazards, exposures and risks associated with crystalline silica".* Request No 2015-SA-0236 – Crystalline silica, 2019.
10. Marques Da Silva, V., et al., *Pulmonary Toxicity of Silica Linked to Its Micro- or Nanometric Particle Size and Crystal Structure: A Review.* Nanomaterials, 2022. **12**(14): p. 2392.
11. Warheit, D.B., et al., *Pulmonary bioassay studies with nanoscale and fine-quartz particles in rats: toxicity is not dependent upon particle size but on surface characteristics.* Toxicological sciences, 2007. **95**(1): p. 270-280.
12. Turci, F., et al., *Revisiting the paradigm of silica pathogenicity with synthetic quartz crystals: the role of crystallinity and surface disorder.* Particle and Fibre Toxicology, 2016. **13**(1): p. 32.
13. Pavan, C., et al., *Nearly free surface silanols are the critical molecular moieties that initiate the toxicity of silica particles.* Proceedings of the National Academy of Sciences, 2020. **117**(45): p. 27836-27846.

14. Mischler, S.E., et al., *Differential activation of RAW 264.7 macrophages by size-segregated crystalline silica.* Journal of Occupational Medicine and Toxicology, 2016. **11**(1): p. 1-14.
15. Wiessner, J.H., et al., *Effect of particle size on quartz-induced hemolysis and on lung inflammation and fibrosis.* Experimental lung research, 1989. **15**(6): p. 801-812.
16. Kajiwara, T., et al., *Effect of particle size of intratracheally instilled crystalline silica on pulmonary inflammation.* Journal of occupational health, 2007. **49**(2): p. 88-94.
17. Wang, J.J., B.J. Sanderson, and H. Wang, *Cytotoxicity and genotoxicity of ultrafine crystalline SiO2 particulate in cultured human lymphoblastoid cells.* Environ Mol Mutagen, 2007. **48**(2): p. 151-7.
18. Pastero, L., et al., *Synthesis of α-quartz with controlled properties for the investigation of the molecular determinants in silica toxicology.* Crystal Growth & Design, 2016. **16**(4): p. 2394-2403.
19. Colombo, C., A.J. Monhemius, and J.A. Plant, *Platinum, palladium and rhodium release from vehicle exhaust catalysts and road dust exposed to simulated lung fluids.* Ecotoxicology and Environmental Safety, 2008. **71**(3): p. 722-730.
20. Carteret, C., *Mid-and near-infrared study of hydroxyl groups at a silica surface: H-bond effect.* The Journal of Physical Chemistry C, 2009. **113**(30): p. 13300-13308.
21. Finch, G.I., *The Beilby Layer on Non-Metals.* Nature, 1936. **138**(3502): p. 1010-1010.
22. Glasson, D.R., *Vacuum balance studies of milled material and mechanochemical reactions.* Thermochimica Acta, 1981. **51**(1): p. 45-52.
23. Bai, Y., et al., *Adsorption of Triton X-series surfactants and its role in stabilizing multi-walled carbon nanotube suspensions.* Chemosphere, 2010. **79**(4): p. 362-367.
24. *Normative e metodologie tecniche di applicazione dell'art. 6, comma 3, e dell'art. 12, comma 2, della legge 27 marzo 1992, n. 257, relativa alla cessazione dell'impiego dell'amianto*, in *094A5917*, M.d. Sanità, Editor. 1996: Gazzetta Ufficiale della Repubblica Italiana.
25. Peyser, P., *The drag reduction of chrysotile asbestos dispersions.* Journal of Applied Polymer Science, 1973. **17**(2): p. 421-431.
26. Innes, E., et al., *Simulated biological fluids–a systematic review of their biological relevance and use in relation to inhalation toxicology of particles and fibres.* Critical Reviews in Toxicology, 2021. **51**(3): p. 217-248.

27. Pavan, C., et al., *Z potential evidences silanol heterogeneity induced by metal contaminants at the quartz surface: Implications in membrane damage.* Colloids and Surfaces B: Biointerfaces, 2017. **157**: p. 449-455.
28. Rimola, A., et al., *Silica surface features and their role in the adsorption of biomolecules: computational modeling and experiments.* Chemical reviews, 2013. **113**(6): p. 4216-4313.
29. Pavan, C., et al., *Molecular recognition between membrane epitopes and nearly free surface silanols explains silica membranolytic activity.* Colloids and Surfaces B: Biointerfaces, 2022. **217**: p. 112625.
30. Pavan, C. and B. Fubini, *Unveiling the variability of "quartz hazard" in light of recent toxicological findings.* Chemical Research in Toxicology, 2017. **30**(1): p. 469-485.
31. IARC, *Silica dust, crystalline, in the form of quartz or cristobalite*, in *Arsenic, Metals, Fibres and Dusts*. 2012, International Agency for Research on Cancer.
32. Thomassen, L.C., et al., *Model system to study the influence of aggregation on the hemolytic potential of silica nanoparticles.* Chemical Research in Toxicology, 2011. **24**(11): p. 1869-1875.

CHAPTER 5: Investigation on the nature of interaction between silica particles and biomembranes

5.1 Background

It was recently proposed by Pavan et al. [1] that the chemical feature able to trigger the membranolysis of phagolysosomes in the lungs and to start inflammation is a family of surface silanols called nearly free silanols, characterized by an intersilanol distance of 4-6Å and detectable with Infrared Spectroscopy. The details of this chemical feature are reported in Paragraph 1.4. NFS can be described as weakly interacting surface moieties as they interact with each other through weak Van der Waals forces and not through hydrogen bond. This makes NFS more prone to interact with molecules that are present in the surroundings of the surface, with respect to vicinal interacting silanols. In particular, according to computational studies, NFS peculiar geometry is held to favor the interaction with charged groups of phosphocholine, one of the most common polar headgroup of phospholipids (PLs), exposed by sphingomyelin (SM) and phosphatidylcholine (PC), PLs in the external leaflet of cellular plasma membranes. [2] The interaction of silica particles with PLs is of crucial interest, because PLs of different kind are present in the lung environment. When a particle is inhaled and reaches the lung (Paragraph 1.1.3), it comes into contact with lipids and proteins that are present in the lung lining layer. Phosphatidylcholine (PC), dipalmitoyl phosphatidylcholine (DPPC), phosphatidylglycerol, phosphatidylserine (PS), sphingomyelin (SM), and albumin are the main molecular components of the lung lining layer. [3] Moreover, phosphatidylcholine, phosphatidylethanolamine, phosphatidylserine, and sphingomyelin are also the major components of the molecular membranes in animal cells. [4]

Interaction between PLs and NFS and their role in membranolysis has been already elucidated. The central role of NFS in causing the silica-induced membrane damage suggests the existence of a molecular recognition pattern between specific phospholipid headgroups and NFS. The interaction between silica particles and phosphatidylcholine has been already studied by Wallace in *in vitro* studies, because it is the most common pulmonary surfactant and the principal component of cellular membranes. [5] Interaction of silica particles with other PLs has not been tested yet.
Moreover, also the role of water in the interaction between NFS and biomembranes has not been elucidated yet.
Water is ubiquitous in the body, and along with surfactants and proteins, it is the solvent in which everything is dispersed and solubilized. Pavan and co-workers simulated the interaction between NFS and PC head without considering the presence of water molecules. [1] At the moment, no experimental evidence on the role of water molecules is reported in literature, because of the difficulty in the detection of the molecular dynamics of this molecule. In recent years, a surface-sensitive technique called Sum-Frequency Generation (SFG) Vibrational Spectroscopy was employed for the detection of the molecular behavior of liquid water in contact with solid surfaces, such as materials or membranes.[6, 7] For example, Ostroverkhov [8] and Ong [9] studied liquid water at the surface of a quartz slab and observed that the orientation of water changes according to the degree of silanol groups protonation. This highly surface sensitive technique is employed also in the study of water at the interface with biological membranes in presence of nanoparticles. [10]

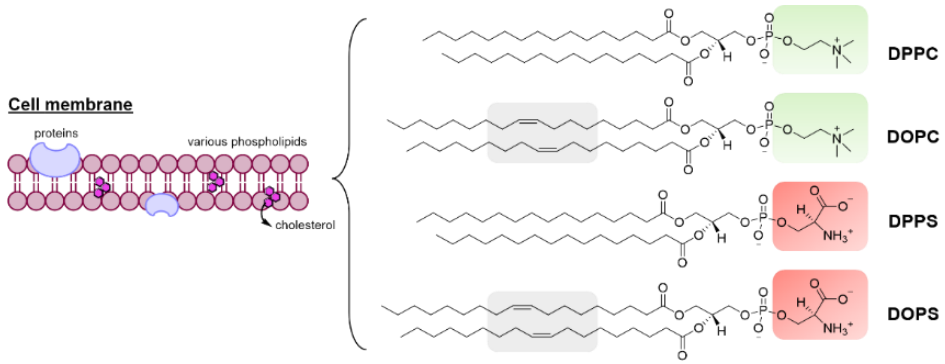

Figure 5.1: schematic structure of a cell membrane and the principal phospholipids taken into account in this Chapter.

In this Chapter, two main topics have been investigated.

1. The first part of this work aims to investigate the specificity of the interaction between silica particles and PLs bearing different polar

heads. For this purpose, silica particles with variable amount of NFS and bulk properties were contacted with two self-assembled PLs vesicles, DOPC (dioleoyl phosphatidylcholine) and DOPS (dioleoyl phosphatidylserine) characterized by the same fatty chain but with a different polar head. (Figure 5.1)

2. The second part aims to investigate the role of water in the interaction between NFS and biomembranes with SFG. For this purpose, an experimental set up for the analysis of interfacial liquid water at the surface of biomembranes in presence of silica particles has been tuned, and three silica particles of different origins and different amount of NFS have been studied, in the interaction with different PLs (Figure 5.1) to understand if there is a correlation between the behavior of water at the interface and the interaction between NFS and PLs heads in biomembranes.

Further insights about the mechanisms of molecular recognition between NFS and membrane epitopes and the molecular behavior of water molecules in interaction with silica will be detailed in the following sections.

5.2 Materials and Methods

5.2.1 Silica particles.

Silica samples selected for this work are the following:

- gQ-f, synthetic quartz ground in a vibratory ball mill, characterized in Chapter 2.
- gQ-f3, synthetic quartz (1.5 g) ground in a planetary ball mill, characterized in Chapter 2.
- Synthetic amorphous silica (aS) of pyrogenic origin kindly supplied by industrial manufacturers.
- Mineral quartz Min-U-Sil 5 (U.S. Silica, Berkeley Springs, WV) was used as a positive reference particle because of its well-documented membranolytic activity and toxicity. [11]
- gQ-n3, nanometric fractured synthetic quartz (1.5 g) ground in a planetary ball mill in a two-step approach, characterized in Chapter 2.
- pS (Areosil50, Degussa), amorphous silica of pyrogenic origin, known for its documented membranolytic activity and NFS amount. [12]
- The silica samples have been selected for their properties, *i.e.,* crystallinity, size, and NFS amount.

5.2.2 Lipid preparation

All phospholipids were purchased from AVANTI polar lipids (AL) in powder form.

- Self-assembled PLs were prepared by adapting a procedure reported in literature, with minor modifications. [13] PL dispersion was probe sonicated three times for 3 min (horn, 3 mm; frequency, 20 kHz; maximum power output, 30 W; amplitude, 120 μm; Sonopuls HD 3100, Bandelin), stored for 10 min on ice, and centrifuged at 2500 x g for 10 min. The supernatant was then diluted to 0.2 mg mL^{-1} to verify the size of the supramolecular structures formed by DLS (Zetasizer Nano ZS, Malvern).
- Solid-supported lipid bilayers (SSLB) of DOPC, DPPC and DPPS were prepared on a CaF_2 prism, with a procedure reported in literature by Cecchet and co-workers [14] Lipid vesicles were prepared by i) solubilizing 1 mg of DPPC or DOPC powder in a minimum amount of chloroform ($CHCl_3$), ii) evaporating chloroform under a N_2 stream and adding 1 mL of MilliQ water. The dispersions were sonicated for 10 min and then centrifuged for 10 min at 6000 rpm. The vesicle dispersions were injected into a Teflon cell (volume equal to 1 mL) holding the CaF_2 substrate to allow the bilayer formation. After 3 h SSLBs of PLs were formed.[10, 15] The vesicles in excess in solution were fully removed by washing with Milli-Q water. Washing of the measure cell was carried out by adding 0.5 mL of Milli-Q water and then removing 0.5 mL of the diluted solution.

5.2.3 Hemolysis assay

5.2.3.a) Hemolysis assay in the absence of PLs.

Hemolysis assay was performed with the procedure reported in Paragraph 3.2.3.

5.2.3.b) Hemolysis assay in the presence of PLs.

Firstly, silica particles were incubated for 30 minutes with the self-assembled PLs dispersions and serial dilutions were performed. A group consisting just of silica particles (without PLs) was added as reference groups. After incubation, suspension of 5% RBC was added to the mixture and the hemolytic activity assessed after a further incubation of 30 min, as described in the previous chapter. PLs at the highest concentration (0.1 mg mL^{-1}) were also incubated with 5% RBC without silica to demonstrate the absence of any

hemolytic effect induced by PLs alone. The hemolytic activity of the silica particles in presence of DOPC was also assessed after washing particles incubated with DOPC. In detail, silica particles were incubated with DOPC (0.1 mg mL^{-1}) or just 0.01M PBS for 30 min at 37 °C on a plate shaker. The mixture was centrifuged at 2500 x g for 10 min (Rotina 380), the supernatant removed, and the pellet obtained used to test the hemolytic activity after washing three times with 1 ml of 0.01M PBS and vortexing for 30 sec.

5.2.4 Thermogravimetric analysis (TGA)

For thermogravimetric measurements, particles incubated with PLs or just 0.01 M PBS were prepared as described for the hemolysis test, and drying particles in an oven at 70 °C overnight. The thermal analysis was performed in an oxidizing atmosphere (O_2 35 mL min^{-1} and N_2 65 mL min^{-1}) with an ultra-microbalance (sensitivity 0.1 µg). The particles (about 10 mg) were heated from 30 to 650 °C at the rate of 2.5 °C min^{-1} in a thermogravimetric balance (Pyris 1 TGA, Perkin-Elmer). The results were analyzed with the Pyris Manager 11 software (Perkin-Elmer) and reported as a weight percentage change at 500 °C with respect to RT for each sample. The temperature of 450 °C was selected because at higher temperatures a weight loss was observed for silica incubated in 0.01M PBS, not observed with dry silica, which has been ascribed to the decomposition of phosphate groups.

5.2.5 Infrared Spectroscopy

IR measurements were carried out in the transmission mode. Aliquots of the sample particles were pressed in self-supporting pellets and placed in a quartz cell equipped with CaF_2 windows. The FTIR spectra were recorded with a Bruker INVENIO R FTIR spectrometer (liquid nitrogen cooled MCT detector; resolution, 4 cm^{-1}) by averaging 128 scans to attain a good signal-to-noise ratio. The cell was attached to a conventional vacuum line (residual pressure ≤ 1×10^{-4} mbar) allowing adsorption–desorption experiments to be carried out *in situ*. Silica samples underwent an hydrogen/deuterium (H/D) isotopic exchange by adsorption/desorption of D_2O (99.90% D) to convert surface silanols (SiOH) in the SiOD) form.

5.2.6 Sum-Frequency Generation (SFG) Spectroscopy measurements.

5.2.6.a) SFG apparatus

The 1064 nm pump beam of the SFG spectrometer is a 15 ps pulsed laser, obtained with the combination of active and passive mode locking of a

Nd:YAG laser source. The repetition rate of each train of pulses is 25 Hz. This beam synchronously pumps two optical parametric oscillators (OPOs), generating the tunable IR and visible photons. The power of the final IR beam is around 12 mW, while that of the visible beam is about 10 mW. In this work, the frequency range of the tunable IR OPO was between 3700 and 2800 cm^{-1}, while the visible OPO was fixed at 532 nm. More details about the SFG spectrometer can be found in the literature. [16] SFG measurements of the substrates/PL and substrates/PL/Si-particles interfaces were recorded in total internal reflection geometry through a prism at both the solid/water and the solid/air interfaces with the SFG, vis, and IR beams in p polarization (ppp).

5.2.6.b) SFG analysis of particle/membrane systems.

SFG spectra of interfacial water was acquired i) on the nude CaF_2 prism, ii) after the formation of the lipid bilayer and iii) after the interaction between the bilayer and the silica particles. A suspension of the silica particle was prepared (0.1 mg mL^{-1}) and probe sonicated for 2 minutes (35% amplitude, 0.5s pulse, UP200S, Hielscher, Berlin, Germany). 0.5 mL of dispersion was injected in the measure cell (Figure 5.7). 0.5 mL of Ultrapure water were then injected to get a total volume of 1 mL. The particles were left in contact with the SSLB for 1 hour.
After the interaction, particles were washed away with ultrapure water and the cell was dried from water using a N_2 stream. SFG spectra of the membrane exposed to air was acquired.

5.2.7 Computational details

All structures shown in Figure 5.5 have been pre-optimized at GFN2 [17] level using the xTB code [18] and subsequently refined at B97–3c [19] level using the ORCA code [20]. This level of theory has been shown to be well suited for structures where non-bonded interactions are dominant. All considered systems have been optimized by embedding in a continuous solvent (water) using the CPMC methods [21], to represent the water environment in which the experiments have been carried out. This approach, albeit unable to consider specific local interactions like hydrogen bonds, allows for a reasonable estimate of the solvation energy.
Computational studies have been performed by prof. Ugliengo and prof. Corno.

5.3 Results and discussions

5.3.1 The molecular recognition between NFS and membrane epitopes is specific and irreversible.

5.3.1.a) Physicochemical characterization of silica particles.

Four silica samples were selected for this study. Model quartz of synthetic origin (gQ) was ball milled in two different conditions to obtain fractured quartzes of different size and SSA (gQ-f and gQ-f3).
Along with the two quartzes, an amorphous silica of pyrogenic origin (aS) was included in the panel as a model for low-hydroxylated (ca. 1.5 OH nm^{-2}), high SSA silica powder characterized by a roundish morphology and particles in the submicrometric range. [22] Finally, Min-U-Sil5 was used as reference due to the well-known toxic activity. Physicochemical characteristics are reported in Figure 5.2.

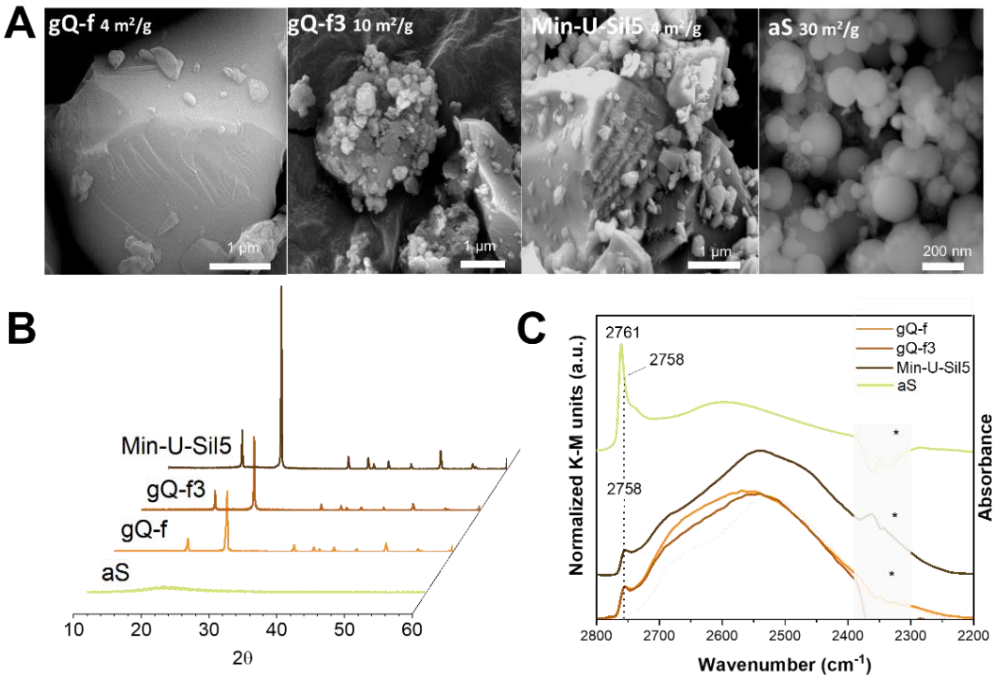

*Figure 5.2: Main physicochemical properties of gQ-f, gQ-f3, aS and Min-U-Sil5. (A) FE-SEM micrographs of the silica samples (B) XRD patterns of quartz and amorphous silica particles, with related SSA (C) Surface silanol distribution measured by IR spectroscopy after H/D isotopic exchange. (data from [1] - except gQ-f3 and aS, from this work). Peak at 2758 cm^{-1} of gQ-f, gQ-f3, Min-U-Sil5, and aS is assigned to nearly free silanols (NFS). *not compensated CO_2.*

5.3.2 Alteration of the hemolytic activity of silica particles when contacted with self-assembled lipid vesicles.

Membranolytic activity of silica particles was assessed with red blood cells (RBC). As already reported in previous literature, gQ-f, Min-U-Sil5 and aS are highly hemolytic. [1, 12, 23] Conversely, gQ-f3 was hemolytic only at the highest dose (200 cm^2/ml). (
Figure 5.3A) The relatively high surface area of gQ-f3 (10.7 m^2/g, about 2-3 times larger than gQ-f and Min-U-Sil5, Figure 5.2A) corresponds to a particle size distribution similar to gQ-f (100% peak around 1.45 µm according to DCS, Paragraph 4.3.1). This peculiar aspect likely accounts for a significant aggregation of this sample. Therefore, the hemolytic activity of gQ-f3 - assessed by dosing equal surface areas - could be lower than what was expected due to the strong aggregation of the particles that effectively decreases the available surface area for the interaction with RBC membrane. The effect observed for gQ-f3 is consistent with similar conclusions drawn for nanosilica aggregates interacting *in vitro* with human bronchial epithelial cells, macrophages, and RBC. [24, 25]

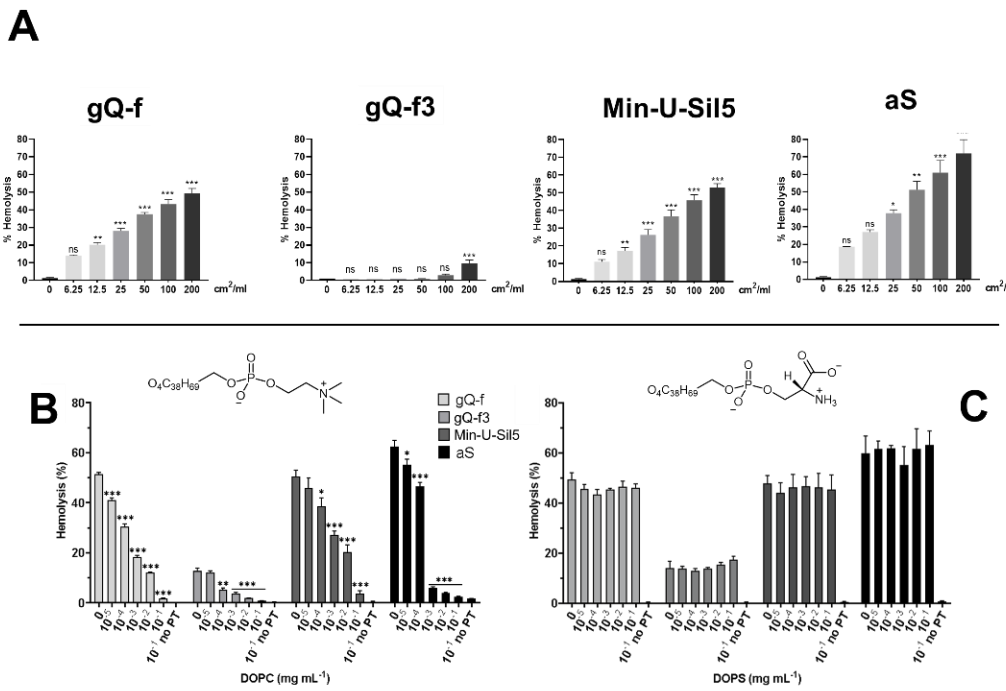

Figure 5.3: Alteration of the hemolytic activity of silica particles. (A) Hemolytic activity of the silica particles incubated with red blood cells. (B-C) Hemolytic activity of the silica particles in presence of self-assembled DOPC and DOPS. Particles were pre-

incubated with just the vehicle (0 mg mL^{-1}) or increasing concentrations (from 10^{-5} to 10^{-1} mg mL^{-1}) of (B) DOPC or (C) DOPS for 30 min.

To investigate the specificity of the interaction between silica and principal components of cell membranes, two PLs with different chemical characteristics were selected, DOPC and DOPS. Selected PLs shared the same lipid chain (dioleoyl, DO) and differed only in the polar headgroup, specifically, phosphocholine (PC) and phosphoserine (PS) (Figure 5.1). At the experimental pH (7.4), PC and PS are highly polar but exhibit different net charges. PC is characterized by a positively charged quaternary amine that balances the negative charge of phosphate, thus rendering the PC polar head zwitterionic. The positive charge on PC is mainly formalized on the nitrogen atom, though some of the positive charge is also distributed on the three methyl groups. [26] The net negative charge of PS is due to the presence of a carboxylic acid residue on the phosphoethanolamine headgroup.

As anticipated in Paragraph 5.1, PC and PS are two of the most common polar headgroups exposed on the surface of cellular membranes and in the composition of the lung lining layer. PC is the headgroup characteristic of DPPC, DOPC and SM. These PLs are usually exposed on the outer part of the membrane, while in the inner leaflet DPPS and DOPS, along with phosphatidylethanolamine (PE), are exposed. [4] Red blood cell membrane is composed in this way. When RBC are subjected to eryptosis, (the death of the RBC) [27], flippases inside the cell expose the inner leaflet (rich in PS) to the external biological environment. Thus, the exposure of PS to the external environment is reported in literature as a clear sign of RBC damage and death. [28]

The investigation on the ability of the silica surface to interact with these PLs is important to understand the role of silica particles in the membranolysis mechanism. Thus, silica particles have been incubated with DOPC and DOPS and the hemolytic activity of the particles in presence of self-assembled DOPC or DOPS structures is reported in

Figure 5.3B-C. Experimental PL concentrations ranged from 10^{-5} to 10^{-1} mg mL^{-1}. DOPC, but not DOPS, reduced the membranolytic activity of the four silica particles in a concentration-dependent manner, and completely inhibited hemolysis at the highest concentration tested. In contrast, DOPS did not significantly reduce the hemolytic activity of the particles at any concentration. This data confirmed the high affinity of silica particles with PC, already reported in literature. [29, 30] However, the selectivity of the interaction was something new. In fact, the different affinity with DOPS confirmed that a stronger interaction occurs between the surface features of silica particles, possibly the NFS, and the polar headgroup of DOPC.

The strong affinity for silica surface that is exhibited by DOPC was confirmed by performing the hemolysis experiment on DOPC-coated silica particles that were washed three times with culture media prior incubation with RBC. Even after washing, the quenching of the hemolytic activity of DOPC-coated silica was observed Figure 5.4A. This finding suggests that DOPC is irreversibly adsorbed on silica surfaces.

The hypothesis was that adsorbed DOPC specifically masked the NFS sites, which are held responsible for silica hemolytic activity. This specific interaction was confirmed for aS, whose high specific surface area allowed to obtain Infrared spectra of self-supporting pellets of aS incubated with PBS, DOPC, and DOPS for 30 min, washed three times with PBS, and dried (Figure 5.4B). The IR spectrum in the ν_{OD} domain of aS+PBS is clearly dominated by the surface NFS stretching band at 2757 cm^{-1}.

The relative intensity of the NFS band was reduced virtually to zero when DOPC irreversibly interacted with silica. The suppression is clearly related with the occurrence of irreversibly adsorbed DOPC molecules sitting at the silica surface. Conversely, the interaction with DOPS did not modify the NFS adsorption band and the spectrum of aS+DOPS was largely superimposable with the aS+PBS spectrum. (Figure 5.4B) It was possible to quantify the amount of the PLs adsorbed on the silica surface by thermogravimetric analysis (TGA) (Figure 5.4C).

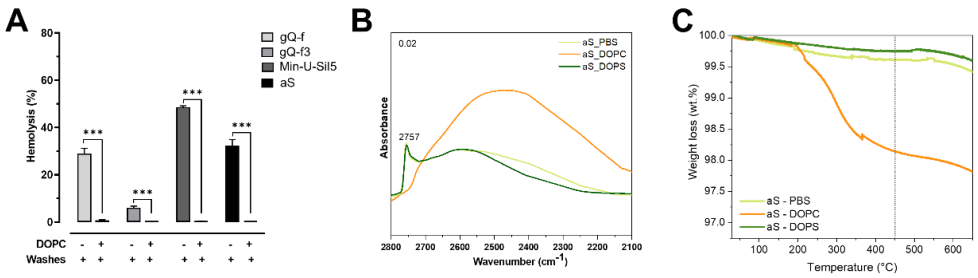

*Figure 5.4: The interaction of silica particles with self-assembled DOPC, but not DOPS, is irreversible and specific for NFS. (A) Irreversible adsorption of DOPC inhibits the hemolytic activity of the silica particles. Data are the mean ± SEM of three independent experiments and were compared with a two-tailed Student's t test. ***p < 0.001 vs. group without PLs, containing only silica. (B) Surface silanol in the vOD spectral region (after H/D isotopic exchange and vOH spectra subtraction) of aS incubated with just 0.01 M PBS, or 0.1 mg mL^{-1} of DOPC or DOPS. (C) Thermogravimetric analysis of dry powder of aS incubated with just the vehicle (0.01 M PBS), or with 0.1 mg mL^{-1} of self-assembled DOPC or DOPS.*

For aS reported in the Figure, but in general for all the silica particles analyzed, DOPC irreversibly adsorbed in significantly larger quantities than DOPS, which confirmed the selective interaction between surface silanols and PC and PS,

respectively. The as+DOPC system reported a significant weight loss starting from 200°C, attributable to the thermal combustion of adsorbed DOPC. In the aS+DOPS system this loss does not occur, because DOPS was not adsorbed on the silica surface.
All these data are in accordance with the reactivity between silica particles and RBC membranes. As anticipated before, the outer leaflet of the RBC membrane is composed for the most part by PLs bearing a PC headgroup. The strong and irreversible interaction between NFS and PC observed here well explains the ability of silica particles to damage RBC membrane and cause membranolysis.

5.3.3 DFT modelling of the DOPC and DOPS phospholipids interaction with the NFS site.

To gain a molecular insight of the possible interaction between the PLs and the silica surface, simulations of the NFS site with PC and PS were performed in collaboration with the group of Computational Chemistry at the University of Turin.

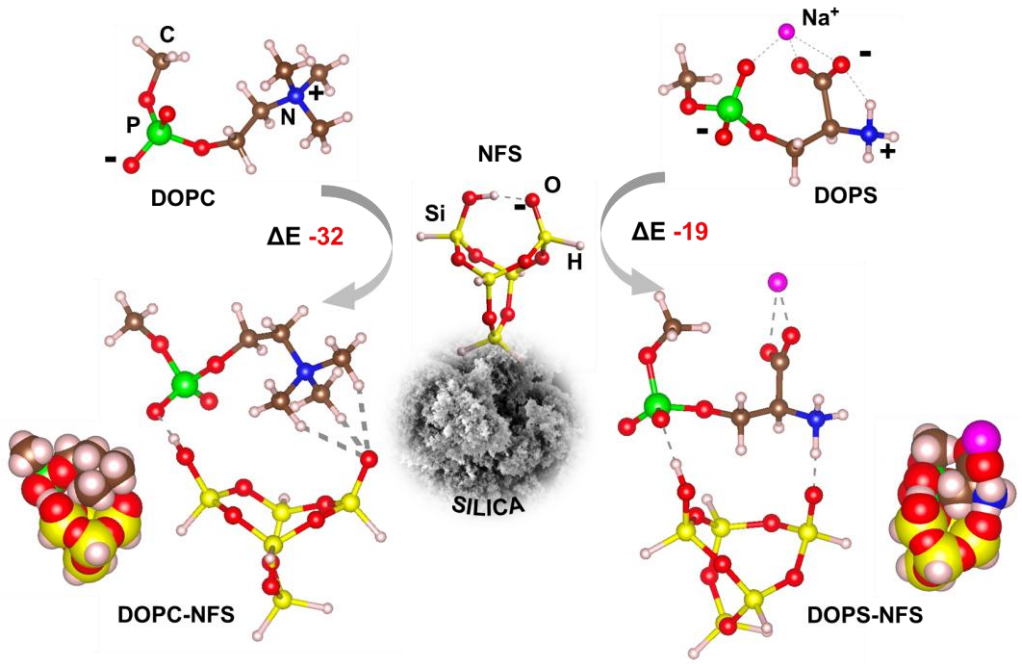

Figure 5.5: Adopted models for PLs (DOPC and DOPS) and the NFS silica site. The energies of interactions (ΔE) between DOPS/DOPC and NFS are reported in unit of kJ mol^{-1}. The van der Waals representations (bottom sides) highlight the most favorable dispersion interactions of DOPC with respect to DOPS.

The simulation was performed using a small cluster exposing a NFS silanol pair on a four membered ring (4MR). To better investigate the effect of charge one silanol group of the NFS pair was deprotonated. The deprotonation of only one of the two silanols of the pair is in agreement with the experimental pH condition (pH 7), in which some of the Si-OH of silica are deprotonated. The $Si–O^-$ is engaged in a strong hydrogen bond with the non-deprotonated silanol. PLs have been represented with idealized structures, in which the role of the hydrophobic tail is played by a single CH_3 group attached to the PO_4 moiety. In this way, we assumed that the lipophilic tail, which is identical in both DOPC and DOPS, is not involved in the interaction with silica, at least when single molecules are considered. The net negative charge of DOPS would impart a bias in the molecular simulation when the interaction of DOPC and DOPS with a negatively charged NFS site is compared.

Therefore, DOPS structure was simulated by adding a Na^+ ion close to the carboxylate group. The Na^+ counterbalances the charge and is consistent with the rich ion environment of the experiments. The interacting structures of both DOPC and DOPS with the NFS sites are shown in Figure 5.5. Their interaction energies showed that the formation of the NFS-DOPC adduct is a more favorable process than NFS-DOPS, with energies of interaction (ΔE) of −32 and −19 kJ mol^{-1}, respectively. As expected from previous experiments, [31] one important component of the ΔE comes from the three weak CH···O bonds that are established between the negative end of the NFS and one positive methyl of the $N(CH_3)_3^+$ group of DOPC. Conversely, a stronger but a single hydrogen bond is formed between DOPS amine and the charged oxygen of NFS. Moreover, if the role of dispersion (London) forces is considered, our model indicates that the two CH_3 groups of DOPC are hosted within the cradle made by the siloxane bonds of the NFS, when the most energetically favorable configuration is reached (see van der Waals representations in Figure 5.5). DOPS can only contribute with a single CH_2 group. Therefore, also the London component of the ΔE is expected to be higher for DOPC than DOPS. Both phospholipids are engaged in one hydrogen bond interaction between the Si-OH group and the negative oxygen of the PO_4^- group and, therefore, are almost equally stabilized in that respect. Another factor of distinction could be the role of the explicit water solvation of both silica and the phospholipids. Assuming the same pattern of solvation for the PO_4^- moiety, the difference is entirely due to the NH_3^+ vs the $N(CH_3)_3^+$ moieties. Calculations with the same methodology adopted here for $N(CH_3)_4^+$ and $CH_3NH_3^+$ (as simplified models for the ammonium groups of DOPC and DOPS, respectively) showed a free energy of solvation favorable for the latter moiety by about 77 kJ mol^{-1}. This indicates that de-solvation of the amino moieties is more favorable for DOPC than DOPS. Ultimately, the electrostatic,

the dispersion, and the de-solvation contributions of the interactions between PLs and NFS indicate that a more favorable energy of interaction for DOPC than DOPS is likely to be observed in neutral saline environments.

5.3.4 Sum-Frequency Generation Spectroscopy as a powerful tool in the detection of the interfacial water layer between silica particles and biomembranes.

5.3.4.a) Sum-Frequency Generation Vibrational Spectroscopy (SFG).

The study of the molecular structures at interfaces is a challenging topic. While the solid-gas interface is usually well studied as it can rely on a plethora of sensitive techniques (IR spectroscopy, Surface Area Analysis Equipment, high vacuum lines, and so on) the investigation of solid-liquid interface is more challenging and requires indirect or non-linear approaches. Sum-Frequency Generation (SFG) Vibrational Spectroscopy is a sensitive vibrational technique which is increasingly used to investigate the solid-liquid interface *in situ*, at the molecular level. [6, 32] SFG is a non-linear optical technique (NLO), based on the combination of two lasers of different frequencies. Non-linear optical techniques are a group of spectroscopies (as Second Harmonic Generation Spectroscopy, Stimulated Raman Spectroscopy) in which photons, in the form of laser sources, interact with the material and generate new photons at different frequencies, which can be detected. These photons are generated by specific phenomena related to the material (according to the technique taken into account), thus they can be extremely specific and selective. [33, 34]
In the case of SFG, the combination of a visible and a IR laser allows to have access on vibrational spectra of adsorbates at an interface. The two lasers give rise to a third beam, which has a wavelength equal to the sum of the other two:

$$\omega_{sfg} = \omega_1 + \omega_2 \qquad \textit{Eq. 5.1,}$$

where ω_1 and ω_2 are the wavelengths of the two primary laser fields and ω_{sfg} is the sum wavelength of the generated SFG photon.
The selection rule of this three-photon process is that an SFG signal is observed only in media without inversion symmetry. Thus, a molecule or a material is detectable only when it does not possess inversion symmetry. Inversion is the property in which, if we change the position of each atom of the material/molecule to its inverse position, through a center of inversion, the material/molecule remains unchanged. [35]

Most bulk materials possess inversion symmetry, and they do not generate SFG signals. On the surface, the inversion symmetry of the bulk is broken, and the molecules on the surface are SFG sensitive.
Usually, in the IR-Vis SFG, the ω_1, which represents the IR laser beam, is tunable, and ω_2 is the fixed visible beam at 532 nm. During the tuning of the IR laser beam, if ω_1 is in resonance with a vibrational mode of a functional group at the interface, the SFG signal intensity, $I(\omega_{sfg})$ is enhanced. The intensity of the SFG signal vs. ω_1 can produce vibrational spectra of the compounds specifically at the surface or at an interface, because of the specific selection rule of SFG.
Experimental and theoretical calculations confirm the applicability of the SFG beam in exploring the molecular environment of surfaces and interfaces. [36] SFG is indeed able of probing interfacial structures of complex surfaces and interfaces, and has been exploited in the last decade to selectively analyze liquid-liquid, liquid-gas, liquid-solid and solid-solid interfaces, including polymeric and biological interfaces. [37]
SFG spectroscopy has been already exploited for the characterization of lipid films. As instance, the symmetry of the two leaflets of a PL bilayer, the kinetics of the flip-flop process of asymmetric bilayers, the structure and orientation of lipids and their surrounding water molecules, and the alterations of membrane models provoked by binding of proteins and peptides, have been elucidated in previous literature. [38-41]

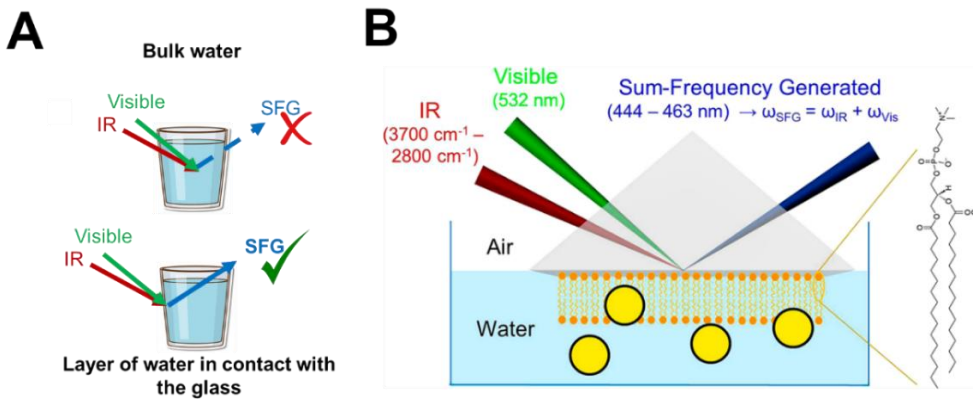

Figure 5.6: Principles of SFG vibrational spectroscopy. (A) Generation of the SFG signal dependent of the orientation of H_2O molecules. Bulk water does not generates any SFG signal, while the water layer at the interface of the glass can generate the SFG signal. (B) Experimental set up useful for the study of water at the interphace with 2D biomembranes in presence of nanoparticles. Reproduced from [10].

Among the possible applications, the detection of interfacial water is of particular interest. In Figure 5.6A is reported the concept of inversion

symmetry applied on interfacial water. While bulk water does not generate an SFG signal, the layer of water molecules in contact with the glass do not possess inversion symmetry and water molecules gain a specific orientation. Thus, a SFG signal is detected.
The study of interfacial water has been exploited both for the characterization of the surface of materials and for the analysis of the organization of water on the surface of two-dimensional biofilms. Among the studies flourishing in the last years, the use of SFG spectroscopy to study the interaction between 2D membranes and nanoparticles in water has been recently approached. In Figure 5.6B is reported the typical experimental set up for this kind of study, in which the lipid bilayer is grown on the CaF_2 prism that conveys the laser beams inward and outward the water-lipid interface. The interfacial water, in contact with the PL layer, organizes in a specific way according to the properties of the bilayer. If nanoparticles are dispersed in water or interact with the lipid bilayer, the interfacial water layer rearranges and its organization at the interface changes. Examples of this phenomenon are reported in recent investigations of the interface between lipid bilayers and gold nanoparticles, [5, 10, 14], antimicrobial peptides, [42] and chitosan oligomers. [43]
We moved forward from these applications of SFG spectroscopy on the study of biomolecular dynamics *in situ* and designed a study to elucidate the behavior of interfacial water during the interaction between NFS-rich silica particles and lipid bilayers.

5.3.4.b) Aim of the study.

Three silica particles with different bulk and surface properties were selected for this study (Table 5.1). Namely, two pyrogenic silicas with different Specific Surface Areas and a crystalline silica (aS, pS, and gQ-n3, respectively) were chosen for their nanometric size, their hemolytic activity and the presence of surface NFS. The experimental set up was inspired from Ref. [10]. In their work, Toledo-Fuentes and co-workers studied the alteration of the water signal before and after the injection of gold nanoparticles. A stable suspension is indeed required to prevent particles to deposit at the bottom of the cell and not interacting with the membranes. The experimental cell and water-lipid-NPs interactions are sketched in Figure 5.7.

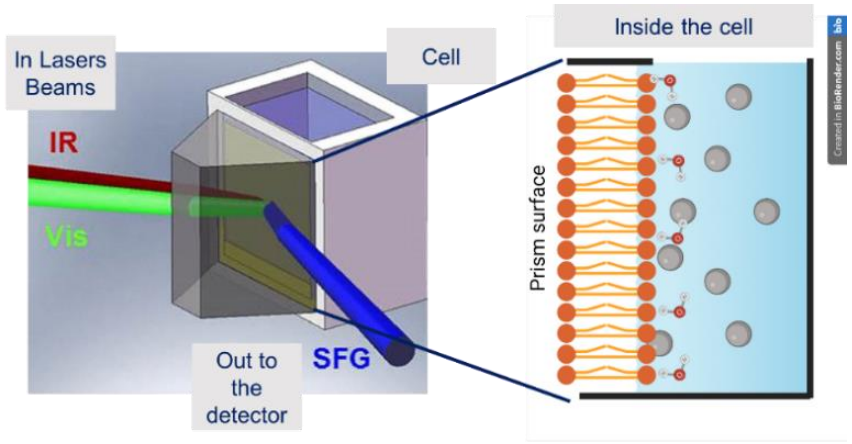

Figure 5.7: details of the experimental design of the SFG cell. Reproduced and adapted from [44]

Silica particles with a variable membranolytic activity and a variable amount of NFS were selected to understand whether NFS have a direct role in the organization of the interfacial water between the particles and the biomembrane. In the paragraph 5.3.1, we proved that NFS specifically and irreversibly interact with PC polar headgroups in PLs. Whether this interaction occurs directly with the formation of H-bonds between charged choline and OH groups in NFS or it is mediated by bridging molecular water is still to be understood. SFG spectroscopy can help to verify if water at the interface has a role in this interaction. For this purpose, three PLs have been chosen: DPPC, DOPC and DPPS (Figure 5.1). Further details are reported in Figure 5.8 and in Table 5.1.

Table 5.1: principal characterization of the silica particles involved in the study.

	pS	**aS**	**gQ-n3**
SSA (m^2/g)	50	27	55
Size (µm ± SD)‡	0.43±0.01	0.35±2.6	0.33±3.2
Hemolysis	+++	+++	+

‡*Hydrodynamic diameter measured in water with Dynamic Light Scattering.*

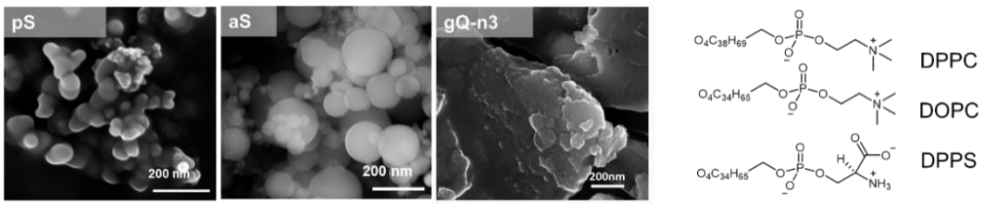

Figure 5.8: morphology of silica particles (on the left) and chemical structure of the PLs selected for the study (on the right).

5.3.4.c) Effect of silica particles on interfacial water orientation.

The interaction between silica particles and DPPC, DOPC and DPPS was investigated, to observe the behavior of interfacial water.

Interaction between the three silica particles and phospholipid membranes has been analyzed by describing the relative intensity of the water band organized at the CaF_2, CaF_2+PL, and CaF_2+PL+SiO_2 interfaces.

In Figure 5.9a is reported the SFG spectrum of interfacial water in contact with the CaF_2 prism (blue spectrum). Water alignment at the interface is related to the absolute ζ potential and the electric field of the surface. Two large SFG superimposed signals at 3150 cm^{-1} (s) and 3350 cm^{-1} (vw) are generated by the oriented molecules of water at the interface with CaF_2. Considering that CaF_2 prism is not characterized by a high electric potential (neutral or weakly positive), the two bands are broad and indistinguishable. When the PL suspension is injected in the measure cell (Figure 5.7b), the intensity of the water signal at 3150 cm^{-1} was monitored as a function of the injection time during the formation of the lipid bilayer on the surface of the prism.

The formation of the DPPC and the DOPC bilayer is reported (panel b and f, Figure 5.9). The intensity of the SFG signal was not subjected to strong alterations, due to the weak change in surface charge. In fact, CaF_2 has a neutral/weakly positive charge, while DPPC/DOPC have a zwitterionic polar head, with a net neutral charge. Thus, the formation of the bilayer did not strongly alter the organization of liquid water at the interface. After the formation of the DPPC/DOPC bilayer the PL in excess was washed away from the cell and the signal of water was collected. The shape of the interfacial water signal remained unaltered, but a visible increase in SFG intensity was observed (panel a and e, red spectrum). This is due to a major structural organization of water molecules sitting at the interface with DPPC/DOPC, and establishing of an electrostatic interaction with PC polar headgroup. According to electrostatic forces, a major coordination can be related to the zwitterionic nature of the PC head, which is overall neutral, but characterized by two separate charges. However, the limited increase in signal intensity is likely due to the ζ potential of the neat prism and the PC membranes.

After the formation of the lipid bilayer, silica particles have been injected in the measure cell. Once more, the intensity of the water signal at 3150 cm^{-1} was monitored as a function of the time of interaction, to monitor any alteration of the signal of interfacial water. (Figure 5.9, panel c and g)

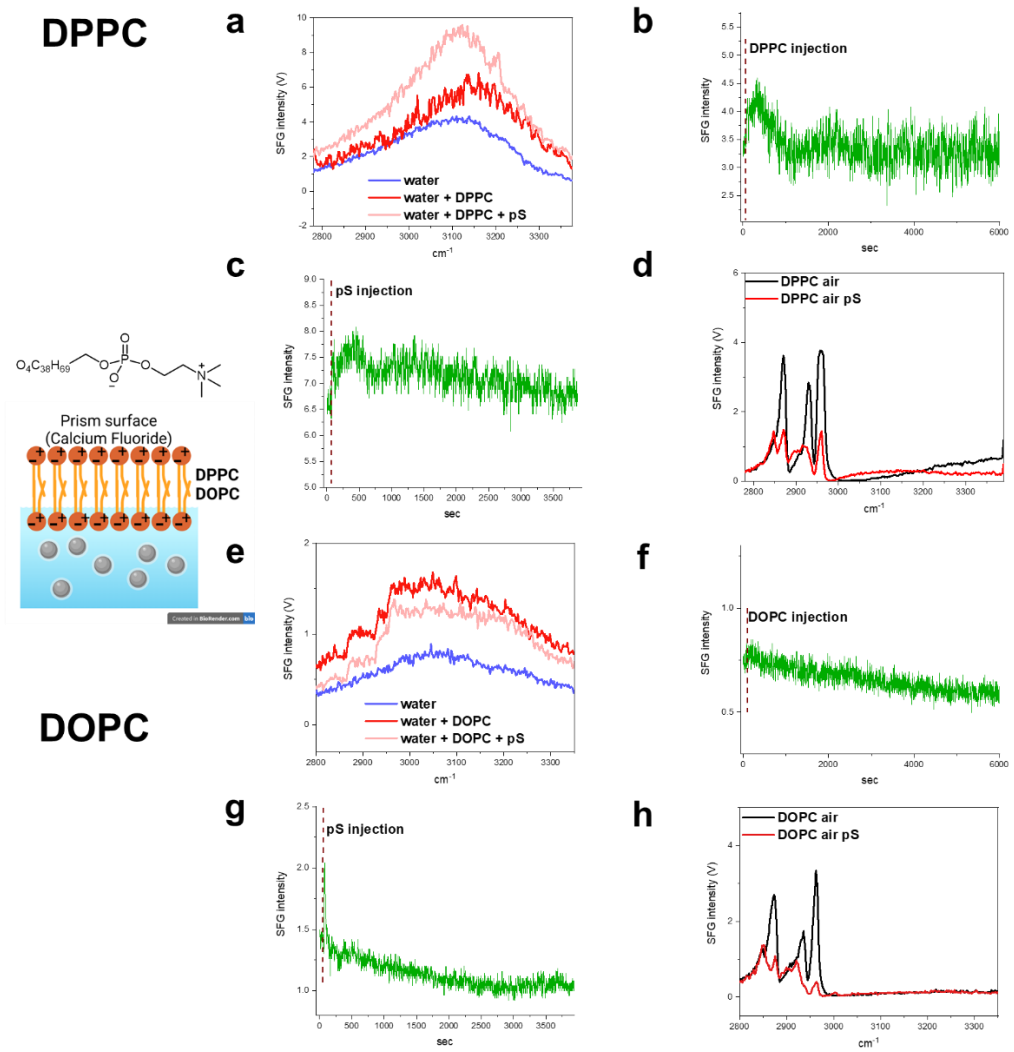

Figure 5.9: SFG experiments of pS with DPPC and DOPC. (a)-(e) interfacial water vibration modes of water+CaF_2 (blue spectrum), water+PL (red spectrum) and water+PL+pS (pink spectrum). (b)-(f) $I_{(sfg)}$ of interfacial water in function of time (s) during the formation of the PL bilayer. (c)-(g) $I_{(sfg)}$ of interfacial water in function of time (s) during the interaction between PL bilayer and pS. (d)-(h) PL interfacial vibration modes when the membrane is exposed to air. v_{as}= antisymmetric stretching of CH_3; v_{Fermi}= CH_3 Fermi resonance; v_s= symmetric stretching of CH_3.

When pS is injected in the measure cell, (panel c and g, Figure 5.9) no differences in the intensity of water were detected for 1 hour. In the case of DOPC, at the moment of the injection of pS a peak of intensity in the water signal was observed (panel g, Figure 5.9). We can speculate that this variation can be reconducted to a greater mobility of the bilayer of DOPC, sensible to

the movement of water during the injection, and not to a direct effect of the presence of the particles.
After the interaction and the washing of the measure cell from the particles the signal of SFG-active water molecules was significantly higher for DPPC (panel a, pink spectrum) and almost unaltered for DOPC (panel e). The correlation between the variation of the water signal intensity and an effect of the particles on the DPPC/DOPC membrane could be explained by investigating the state of the dry membrane, after the interaction.
In fact, SFG is sensitive to the CH stretching generated by the lipid chains of the PL bilayer. Usually, when the bilayer is immersed in water, no signal from the PLs is observed, meaning that the lipid chains experience an environment with inversion symmetry, typical of a homogeneous bilayer. However, when the bilayers formed in an aqueous environment are exposed to air, an intense set of peaks appears at 2959, 2933 and 2870 cm^{-1}, due to the degenerate asymmetric stretching mode, the Fermi resonance, and the symmetric stretching mode of CH_3 groups, respectively (Figure 5.9d, black spectrum and Figure 5.10). [45]

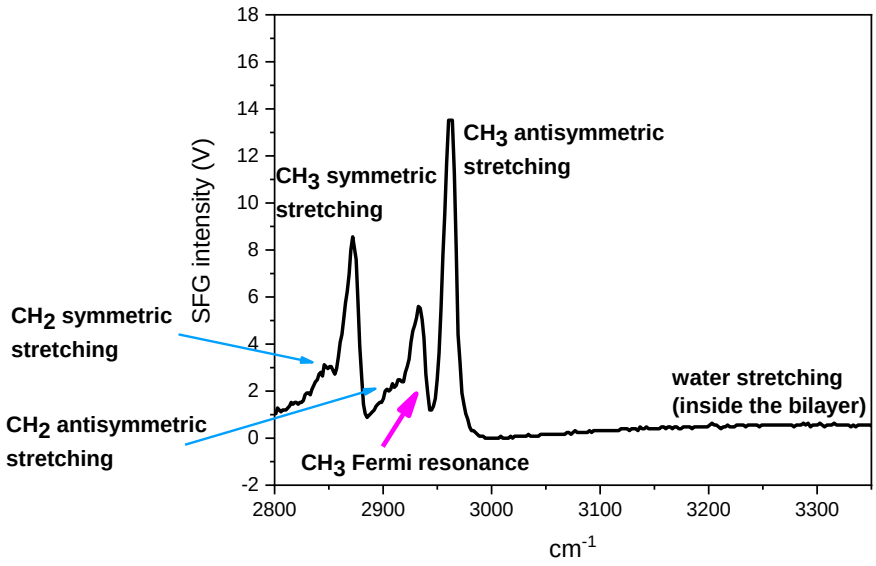

Figure 5.10: Magnification of the spectrum of an ordered lipid bilayer

The SFG-active modes of CH_3 indicate that the inversion symmetry of the lipid bilayer is broken, once one layer of the membrane is exposed to air. The bilayer exposed to air spontaneously unfold forming non-symmetric monolayers and trilayers of lipids. [46, 47] However, the negligible SFG signals from CH_2 groups forming the lipid chains, prove that the hydrophobic tails

have kept an *all trans* conformation, typical of a well packed phospholipid macrostructure. Finally, in the 3100-3300 cm^{-1} range, a broad weak shoulder indicates the presence of SFG-active OH vibrations and suggests that water is not completely expelled from the CaF_2 interface during the formation of the PL layer. [48, 49]

In panel d and h are reported the SFG spectra of DPPC and DOPC before (in black) and after (in red) the interaction with pS. The dry DPPC/DOPC spectrum is characterized by the three features previously described. After the interaction with pS, the SFG-visible CH_3 stretchings were accompanied by two more signals at 2960 and 2888 cm^{-1}, which belongs to the antisymmetric and symmetric stretching of CH_2 groups, respectively. These two bands signal a change in the order of the lipidic tails of DPPC and DOPC. In general, the packing of the lipid tails exhibits an *all-trans* conformation, with an environment characterized by inversion symmetry of all the CH_2 groups that renders the CH_2 stretching modes SFG-silent. When the membrane interacts with pS, the CH_2 SFG signal indicates a higher disorder of the lipid membrane, that can be explained with the reorientation of some lipid chains in a *gauche* conformation. [50] This may signal a structural damage of the lipid bilayer, and prompted us to speculate that pS damaged the DPPC/DOPC membrane in the interaction. Following the Toledo-Fuentes and coworkers hypothesis, [10] the increase of the SFG signal of water observed after the interaction with the particles (Figure 5.9a) indicate the reinforcement of the water alignment after the interaction between pS and the membrane, meaning that some nanoparticles can be in close contact with the zwitterionic polar heads of PC. In turn, this strong interaction would extract the choline groups from the membrane surface, thus enhancing the water loss of symmetry and rendering the choline group more available in the interaction with the silica surface. This would well correlate with the subsequent disorder of the PL bilayer observed. However, with DOPC a strong alteration of the membrane was detected with the predominance of CH_2 signals, but the corresponding increase in the water signal during the interaction was not observed.

Intriguingly, an opposite trend was observed when DPPS was contacted with pS. DPPS shows a net negative charge due to the carboxylated serine polar head. The SFG signal of water recorded a time-dependent modification during the DPPS bilayer formation (Figure 5.11b).

The *in situ* real time monitoring of the molecular reorientation of water can be observed in panel b (Figure 5.11). After 500 seconds from PL injection, a minimum of the intensity of the SFG signal of water is observed. This minimum corresponds to the higher degree of molecular disorder reached by interfacial water during formation of the DPPS bilayer. Once the bilayer is formed, water re-aligned with time and the intensity of the SFG signal returns

to the original value, signaling the restoration of a molecular ordered state, even with an opposite orientation.

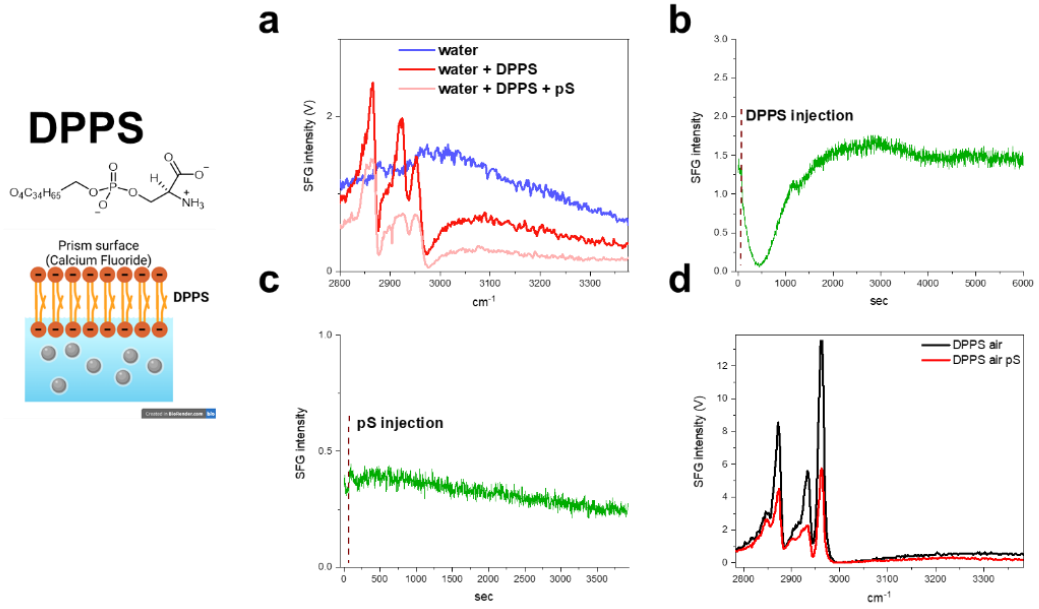

Figure 5.11: SFG experiments of pS with DPPS. (a) interfacial water vibration modes of water+CaF_2 (blue spectrum), water+PL (red spectrum) and water+PL+pS (pink spectrum). (b) $I_{(sfg)}$ of interfacial water in function of time (s) during the formation of the PL bilayer. (c) $I_{(sfg)}$ of interfacial water in function of time (s) during the interaction between PL bilayer and pS. (d) PL interfacial vibration modes when the membrane is exposed to air.

This strong reorientation of water was visible with DPPS but not with DPPC and DOPC, because their zwitterionic polar headgroups do not cause a strong polarization and consequent rearrangement of the water layer, during the formation of PL bilayer.

However, the intensity of the SFG spectrum of water significantly decreased after the DPPS bilayer formation and the washing of the cell, and the three-featured SFG profile of the lipid chains was evidenced already in the wet experiment (Figure 5.11, panel a, red spectrum). Adding pS to the cell did not cause any alteration of the water signal during the time of interaction (panel c), but after the washing of the measure cells from the particles, the intensity of the water signal further decreased. The presence of the SFG profile of the lipid chain in presence of water in the cell usually suggests a high disorder of the membrane. [5, 10]

However, when the DPPS layer is dried and exposed to the air, the SFG spectrum of CH_3 in the lipid tails signals an highly ordered bilayer (panel d, red curve). After the interaction with pS, the dry DPPS layer exhibited a rather

superimposable SFG spectrum with respect to the pristine DPPS. The relatively low presence of CH_2 bands signal a well-ordered lipidic structure. We can therefore assume that a negligible interaction occurred between pS and DPPS.
The behavior of DPPS in water on the CaF_2 prism observed in the experiment is quite peculiar and no other examples are reported in literature at the moment. The net negative charge of DPPS probably generated vesicles that in pure water tended to remain in the micellar form, even if CaF_2 is neutral-weakly positive. Probably the surface charge of the prism can induce the micelles to adhere at the surface but did not dissolve them to form a continuous bilayer. This may explain the presence of SFG signals from CH_3 also in water.
The interaction with DPPC, DOPC and DPPS has been performed also on the other two silica particles, with similar results. For brevity, only pS is shown here, but the other results are reported in Table 5.2. By varying the silica particle involved in the interaction, little to none difference was observed. As instance, aS and DOPC strongly interacted, while gQ-n3 is the one that interacted less with all the three membranes. DPPS remained unaltered after the interaction with all the three silica particles. The results on the membrane damage are well correlated with the amount of nearly free silanols present on the surface of silica particles. As instance, gQ-n3, the NFS-poorest of the three samples, is also the one that interacted less with the membranes.
Moreover, all the three silica particles did not interact with DPPS, in good accordance with the results obtained in the first part of this Chapter.

Table 5.2: Summary of the results of the interaction between phospholipids and silica particles monitored by SFG spectroscopy.

	Hemolytic activity	*NFS*	DPPC	DOPC	DPPS
pS	+++	+++	++	+++	–
aS	+++	+++	+	+++	–
gQ-n3	+	+	–	–	–

However, the difference in the membrane damage, and the relative amount of NFS, are difficult to correlate with the variations observed in the $I_{(sfg)}$ of the interfacial water modes.
Two different hypotheses can be taken into account:

- The role of water is not crucial in the interaction between NFS and biomembranes. We can hypothesize a model of interaction devoid of the mediation of water between NFS and phospholipid heads. The SFG data would confirm the model previously described in which the

NFS pair and the PC head directly interact through H-bond, without the presence of water molecules at the interface mediating the interaction. This explains the lack of correlation between the alteration of the water signal and the different outcomes in the membrane damage.

- The result can be due to an issue related to the size of the silica particles. Nanoparticles in a very small and controlled size range (around 5-10 nm) were used in previous works, while silica particles used in our study have a variable size range due to strong agglomeration behavior (200-400 nm). It can be possible that a part of the samples, organized in agglomerates, was not able to interact with the membrane because it deposited at the bottom of the cell without interacting with the membrane. The other part of the sample could interact with the membrane, but the alteration could be lower than the expected, with also a lower involvement of the interfacial water.

In conclusion, despite we were able to gather precious information about the different interactions established, still a strong conclusion about the behavior of water molecules in the NFS-PL interaction is difficult to draw. A reliable way to strengthen these results is by expanding the panel of samples, and by varying the surface characteristic and the size of the particles.

5.4 Main achievements

In this Chapter, the interaction between nearly free silanols and four phospholipids, namely DOPC, DPPC, DOPS and DPPS, was investigated. The favorable interaction between the phosphatidylcholine (PC) and NFS was elucidated in previous studies. Here, DOPC and DOPS vesicles were contacted with silica particles with a variable amount of NFS and a macroscopic selectivity in the interaction was observed. Silica interacted selectively and irreversibly with phospholipid structures when they exhibit a neutral PC but not when a negatively charged PS is exposed. It was possible to conclude that DOPC is able to adsorb on the surface of silica by specifically masking NFS. On the contrary, DOPS was not able to interact at all. These data support the hypothesis that such specific and selective interaction requires concurrently the presence of NFS on silica surface and the presence of a definite molecular conformation and charge distribution on the PL polar head. The quaternary amine and the phosphate group of PC offer the ideal molecular conformation that maximizes the interaction energy with a NFS pair. This finding is supported also by and *ab initio* modeling of the interaction reported here.

The second aspect investigated in this Chapter is the possible role of water in the NFS-PLs interaction. To observe the behavior of water at the interface with a phospholipid membrane in presence of silica particles, an experimental set up with Sum-Frequency Generation Vibrational spectroscopy was designed and carried out at University of Namur (B). The result verified the different interactions between a PC and a PS headgroups when in interaction with NFS rich silica particles. Also, variability in the water behavior was observed, but it was not possible to establish a strong correlation between the water behavior and the resulted membrane damage. In the future, it should be possible to expand the panel of silica particles involved in the study to gain a further insight in this aspect of the interaction. Moreover, SFG spectroscopy was proved to be a very sensitive and powerful tool to study specific molecular dynamics *in situ*, otherwise only accessible with computational studies.

5.5 Bibliography

1. Pavan, C., et al., *Nearly free surface silanols are the critical molecular moieties that initiate the toxicity of silica particles.* Proceedings of the National Academy of Sciences, 2020. **117**(45): p. 27836-27846.
2. Van Meer, G., D.R. Voelker, and G.W. Feigenson, *Membrane lipids: where they are and how they behave.* Nature reviews Molecular cell biology, 2008. **9**(2): p. 112-124.
3. Schleh, C. and J.M. Hohlfeld, *Interaction of nanoparticles with the pulmonary surfactant system.* Inhalation toxicology, 2009. **21**(sup1): p. 97-103.
4. Cooper, G.M., *The Cell, a molecular approach, 2nd edition*, ed. S.M.S.A. 2000. 2000.
5. Toledo-Fuentes, X., C. Molinaro, and F. Cecchet, *Interfacial charges drive the organization of supported lipid membranes and their interaction with nanoparticles.* Colloids and Surfaces B: Biointerfaces, 2018. **172**: p. 254-261.
6. Vidal, F. and A. Tadjeddine, *Sum-frequency generation spectroscopy of interfaces.* Reports on Progress in Physics, 2005. **68**(5): p. 1095.
7. Morita, A., *Theory of sum frequency generation spectroscopy*. Vol. 97. 2018: Springer.
8. Ostroverkhov, V., G.A. Waychunas, and Y. Shen, *New information on water interfacial structure revealed by phase-sensitive surface spectroscopy.* Physical review letters, 2005. **94**(4): p. 046102.
9. Ong, S., X. Zhao, and K.B. Eisenthal, *Polarization of water molecules at a charged interface: second harmonic studies of the silica/water interface.* Chemical Physics Letters, 1992. **191**(3): p. 327-335.
10. Toledo-Fuentes, X., D. Lis, and F. Cecchet, *Structural changes to lipid bilayers and their surrounding water upon interaction with functionalized gold nanoparticles.* The Journal of Physical Chemistry C, 2016. **120**(38): p. 21399-21409.
11. IARC, *Silica dust, crystalline, in the form of quartz or cristobalite*, in *Arsenic, Metals, Fibres and Dusts*. 2012, International Agency for Research on Cancer.
12. Pavan, C., et al., *In search of the chemical basis of the hemolytic potential of silicas.* Chemical research in toxicology, 2013. **26**(8): p. 1188-1198.
13. Wallace Jr, W., et al., *In vitro biologic toxicity of native and surface-modified silica and kaolin.* Journal of Toxicology and Environmental Health, Part A Current Issues, 1985. **16**(3-4): p. 415-424.

14. Molinaro, C. and F. Cecchet, *Label-free, quantitative and sensitive detection of nanoparticle/membrane interactions through the optical response of water.* Sensors and Actuators B: Chemical, 2019. **289**: p. 169-174.
15. Keller, C., et al., *Formation of supported membranes from vesicles.* Physical Review Letters, 2000. **84**(23): p. 5443.
16. Mani, A., et al., *Pumping picosecond optical parametric oscillators by a pulsed Nd: YAG laser mode locked using a nonlinear mirror.* Applied Physics Letters, 2001. **79**(13): p. 1945-1947.
17. Bannwarth, C., S. Ehlert, and S. Grimme, *GFN2-xTB—An accurate and broadly parametrized self-consistent tight-binding quantum chemical method with multipole electrostatics and density-dependent dispersion contributions.* Journal of chemical theory and computation, 2019. **15**(3): p. 1652-1671.
18. Bannwarth, C., et al., *Extended tight-binding quantum chemistry methods.* Wiley Interdisciplinary Reviews: Computational Molecular Science, 2021. **11**(2): p. e1493.
19. Brandenburg, J.G., et al., *B97-3c: A revised low-cost variant of the B97-D density functional method.* The Journal of chemical physics, 2018. **148**(6): p. 064104.
20. Neese, F., et al., *The ORCA quantum chemistry program package.* The Journal of chemical physics, 2020. **152**(22): p. 224108.
21. Barone, V. and M. Cossi, *Quantum calculation of molecular energies and energy gradients in solution by a conductor solvent model.* The Journal of Physical Chemistry A, 1998. **102**(11): p. 1995-2001.
22. Zhuravlev, L., *Concentration of hydroxyl groups on the surface of amorphous silicas.* Langmuir, 1987. **3**(3): p. 316-318.
23. Turci, F., et al., *Revisiting the paradigm of silica pathogenicity with synthetic quartz crystals: the role of crystallinity and surface disorder.* Particle and Fibre Toxicology, 2016. **13**(1): p. 32.
24. Thomassen, L.C., et al., *Model system to study the influence of aggregation on the hemolytic potential of silica nanoparticles.* Chemical Research in Toxicology, 2011. **24**(11): p. 1869-1875.
25. Murugadoss, S., et al., *Toxicology of silica nanoparticles: an update.* Archives of toxicology, 2017. **91**(9): p. 2967-3010.
26. Yeagle, P.L., *The membranes of cells*. 2016: Academic Press.
27. Repsold, L. and A.M. Joubert, *Eryptosis: An Erythrocyte's Suicidal Type of Cell Death.* Biomed Res Int, 2018. **2018**: p. 9405617.
28. Chen, Z., et al., *Eryptosis is an indicator of hematotoxicity in the risk assessment of environmental amorphous silica nanoparticles*

exposure: The role of macromolecule corona. Toxicology Letters, 2022. **367**: p. 40-47.
29. Gao, N., et al., *Effects of simulated pulmonary surfactant on the cytotoxicity and DNA-damaging activity of respirable quartz and kaolin.* Journal of Toxicology and Environmental Health Part A, 2000. **60**(3): p. 153-167.
30. Liu, X., et al., *Phospholipid surfactant adsorption by respirable quartz and in vitro expression of cytotoxicity and DNA damage.* Toxicology letters, 1998. **96**: p. 77-84.
31. Depasse, J. and J. Leonis, *Inhibition of the hemolytic activity of quartz by a chemically modified lysozyme.* Environmental research, 1976. **12**(3): p. 371-374.
32. Eisenthal, K.B., *Second harmonic spectroscopy of aqueous nano-and microparticle interfaces.* Chemical reviews, 2006. **106**(4): p. 1462-1477.
33. Boyd, R.W., *Nonlinear optics*. 2020: Academic press.
34. Shen, Y., *A few selected applications of surface nonlinear optical spectroscopy.* Proceedings of the National Academy of Sciences, 1996. **93**(22): p. 12104-12111.
35. Atkins, P., P.W. Atkins, and J. de Paula, *Atkins' physical chemistry*. 2014: Oxford university press.
36. CHEN, Z., *Molecular structures of buried polymer interfaces and biological interfaces detected by sum frequency generation vibrational spectroscopy.* Acta Physico-Chimica Sinica, 2012. **28**(3): p. 504-521.
37. Chen, Z., *Investigating buried polymer interfaces using sum frequency generation vibrational spectroscopy.* Progress in polymer science, 2010. **35**(11): p. 1376-1402.
38. Liu, J. and J.C. Conboy, *Direct measurement of the transbilayer movement of phospholipids by sum-frequency vibrational spectroscopy.* Journal of the American Chemical Society, 2004. **126**(27): p. 8376-8377.
39. Chen, X., et al., *Interfacial water structure associated with phospholipid membranes studied by phase-sensitive vibrational sum frequency generation spectroscopy.* Journal of the American Chemical Society, 2010. **132**(32): p. 11336-11342.
40. Lis, D., et al., *Vibrational Sum-Frequency Generation Activity of a 2, 4-Dinitrophenyl Phospholipid Hybrid Bilayer: Retrieving Orientational Parameters from a DFT Analysis of Experimental Data.* ChemPhysChem, 2013. **14**(6): p. 1227-1236.
41. Fu, L., Z. Wang, and E.C. Yan, *Chiral vibrational structures of proteins at interfaces probed by sum frequency generation spectroscopy.*

International journal of molecular sciences, 2011. **12**(12): p. 9404-9425.
42. Chen, X. and Z. Chen, *SFG studies on interactions between antimicrobial peptides and supported lipid bilayers.* Biochimica et Biophysica Acta (BBA)-Biomembranes, 2006. **1758**(9): p. 1257-1273.
43. Rimoli, C.V., R. de Oliveira Pedro, and P.B. Miranda, *Interaction mechanism of chitosan oligomers in pure water with cell membrane models studied by SFG vibrational spectroscopy.* Colloids and Surfaces B: Biointerfaces, 2022. **219**: p. 112782.
44. Lis, D. and F. Cecchet, *Unique Vibrational Features as a Direct Probe of Specific Antigen–Antibody Recognition at the Surface of a Solid-Supported Hybrid Lipid Bilayer.* ChemPhysChem, 2016. **17**(17): p. 2645-2649.
45. Liu, J. and J.C. Conboy, *Phase transition of a single lipid bilayer measured by sum-frequency vibrational spectroscopy.* Journal of the American Chemical Society, 2004. **126**(29): p. 8894-8895.
46. Castellana, E.T. and P.S. Cremer, *Solid supported lipid bilayers: From biophysical studies to sensor design.* Surface Science Reports, 2006. **61**(10): p. 429-444.
47. Cremer, P.S. and S.G. Boxer, *Formation and spreading of lipid bilayers on planar glass supports.* The Journal of Physical Chemistry B, 1999. **103**(13): p. 2554-2559.
48. Watanabe, K., *Model for measurement of water layer thickness under lipid bilayers by surface plasmon resonance.* Biomedical Optics Express, 2011. **2**(5): p. 1115-1120.
49. Khan, M.S., N.S. Dosoky, and J.D. Williams, *Engineering lipid bilayer membranes for protein studies.* International journal of molecular sciences, 2013. **14**(11): p. 21561-21597.
50. Yellin, N. and I.W. Levin, *Hydrocarbon chain trans-gauche isomerization in phospholipid bilayer gel assemblies.* Biochemistry, 1977. **16**(4): p. 642-647.
51. Khatib, R., et al., *Water orientation and hydrogen-bond structure at the fluorite/water interface.* Scientific reports, 2016. **6**(1): p. 24287.

CHAPTER 6: General conclusions

6.1 Concluding remarks

Crystalline silica is a well-known toxic particle that may cause severe pathologies, such as silicosis, lung cancer, and autoimmune diseases. [1-3]
Prolonged exposure to silica particles may occur in some occupational settings (*e.g.*, mining, sandblasting, construction, clothe sanding). Outbreaks of silicosis were reported in developing countries, which do not have strict prevention rules, and in specific occupational settings, such as those related to the processing of artificial stones. [4-6] However, not all silica sources are equally pathogenic, and differences among silica sources were often highlighted in scientific studies, exposing the issue of the "variability of silica hazard". [7] For decades, the origin of the toxic activity of respirable silica particles was unclear. As crystalline silica was generally more pathogenic than amorphous silica, several studies postulated that crystallinity was the crucial chemical feature able to trigger silicosis. However, not all the crystalline silica polymorphs are pathogenic (*e.g.*, stishovite), and some amorphous silicas, such as pyrolytic amorphous silicas, can provoke acute inflammation in the lung. Moreover, even between quartz particles of different industrial origin the toxic effect is not equal.
Recently, it was reported that synthetic quartz, with non-fractured as-grown surfaces, is not able to provoke membranolysis, which is the molecular initiating event (MIE) of the adverse outcome pathway (AOP) for silica dust. [8, 9] When the same quartz was mechanically fractured, it became membranolytic. [10] For this reason, the role of crystallinity was disregarded, and other surface properties were taken into account. In particular, the surface disorder generated by the mechanical fracturing is reflected in a major disorder of the surface features and, specifically, on the distribution of surface silanols. Silanols and siloxanes are the two functional groups present on the surface of quartz. Silanols (≡SiOH) have the ability to interact with molecules present in the external environment with hydrogen bonding or other intermolecular forces. When crystalline silica is subjected to mechanical fracturing (*e.g.*, ball milling) a new family of surface silanols, called nearly free silanols, is formed. NFS are silanols with a specific topochemistry

distinguished by an intersilanol distance of 4-6 Å. It was observed a direct correlation between the presence of NFS on the surface of fractured crystalline silica of respirable size (RCS) and its ability to cause membranolysis. [11] NFS were also detected on the surface of inflammogenic pyrolytic silicas. NFS were proposed to be the responsible molecular agents of membranolysis, but the paradigm of the lower toxicity of amorphous vs. crystalline silica still holds. The lungs in fact clear amorphous silicas more efficiently than crystalline silica, because the former lower biopersistence causes only a transient inflammation. [12] The positive correlation between the occurrence of NFS and the membranolytic activity was confirmed for all the different silica polymorphs. In particular, stishovite, the non-toxic crystalline polymorph of silica, was shown to be the only SiO_2 polymorph that does not exhibit NFS. [13] The NFS paradigm explains several aspects of silica membranolytic activity and inflammation. However, regarding the surface characterization of fractured quartz and some details on the interaction between NFS and biomembranes, some questions remain unanswered.
In this PhD thesis three main topics were addressed.

1. The effect of the milling and ageing environments on the surface reconstruction of quartz subjected to mechanical fracturing.
2. The study of the physicochemical characteristics and the membranolytic activity of top-down generated nano-quartz.
3. The study of the membranolytic activity of NFS, specifically the role of membrane epitopes and interfacial water.

6.1.1 Effect of the milling and the ageing environments on the surface reconstruction of quartz

The study of the surface reconstruction of milled quartz started with the optimization of the milling protocol, with the aim of milling down to a respirable size two model quartzes, one of mineral origin and one of synthetic origin. The optimized procedure was performed in four different environments, varying the concentration of oxygen and water vapor. The amount and the types of radical species were assessed with EPR spectroscopy. EPR spectroscopy allowed us a sensitive analysis of the samples without any manipulation of the powder, analyzed without alterations immediately after milling.
The radical species detected by EPR differed both qualitatively and quantitively on the four milled samples, confirming that surface sites generated by milling are indeed influenced by the milling environment. The largest amount of radicals was generated in water-free environments. Oxygen, when present in the milling environment, generated a larger quantity of oxygenated radical species. The lowest amount of radical species was

formed when in the milling environment was present water vapor. Moreover, radical species were also characterized by a different reactivity when exposure to probe molecules. A higher reactivity of the surface was evidenced on quartz milled in the $–H_2O/–O_2$ environment.

Under the four milling environments ($\pm H_2O/\pm O_2$), all quartz dusts resulted non-membranolytic. However, when the four quartzes were exposed to water vapor their membranolytic activity differentiated. Quartz milled in a water-free environment, once exposed to water vapor, immediately became membranolytic. Quartz milled in a water-rich environment remained non-membranolytic after the contact with water vapor. Furthermore, continuous exposure to water vapor after milling had the ability to mildly activate the surfaces of quartz, also when milled in water-rich environments. Thus, this study for the first time highlighted two main points:

1. Milling environment affects the formation and the stabilization of the surface active sites of milled quartz and determines the reactivity of the surface towards active molecules.
2. Water vapor is the molecular determinant able to activate non-stabilized surface radicals on fractured quartz. Water vapor rapidly reacts with quartz milled in water-poor environments, while slowly reacts with quartz milled in water-rich environments. In both cases, quartz became membranolytic, and milling conditions affected the activation kinetics.

The investigation on the mechanisms of surface reconstruction of milled quartz was completed with two more quartz flours that were ground in respirable size by the industrial partners and received by our lab two weeks after milling. Starting from the conclusions of the study on model quartzes, the effect of ageing environment was monitored. Industrial quartz flours were stored in different ageing environments differing by water vapor pressure that ranged from ca. 0 to 300 mbar. The membranolytic activity of the two industrial quartz flours was not affected by any of the four ageing environments up to 10 months. Only a strong acidic treatment (*i.e*, treatment with hydrofluoric acid) was able to vary the membranolytic activity of these quartz flours, confirming the strong stability of the surface of these quartzes of industrial origin and the role of NFS in determining pro-inflammatory action of quartz.

6.1.2 Characteristics and toxicological activity of fractured nanoquartz.

Pure synthetic quartz of micrometric size (gQ) was milled down to nanometric size (< 100 nm) by high-energy planetary ball milling. The top-down method, not designed to mimic industrially relevant conditions, was optimized to

generate an ultrafine quartz sample to be used as a reference material for toxicological and occupational exposure to respirable crystalline silica (RCS). Our quartz nanoparticles showed dimensional and adhesion properties compatible with the quartz nanoparticles generated during standard workplace operations. Quartz nanoparticles exhibited a specific surface area up to 55 m^2/g, a primary particle size in the nanometric range, and a negligible number of micrometric particles. During the milling procedure, some nanometric crystalline particles were progressively amorphized (up to 40 wt.%), likely due to local thermal effects, but a relevant number of crystalline nanometric particles were preserved (ca. 55 wt.% of every ball milled sample). Several agents were used to examine the dispersibility of the nanoquartz in aqueous media. Overall, the nanoquartz resulted largely agglomerated in water, in different biologically-relevant media (*e.g.*, phosphate buffer and artificial lysosomal fluid), in presence of surfactants, and after sonication. This suggested that during milling strongly interacting agglomerates were formed, which also persisted in biological media. However, the strong aggregation did not hamper the bioavailability of the nanoquartz agglomerates, which largely remains in the respirable size range. Furthermore, the interparticle electrostatic forces that promote agglomeration in the samples might well explain the difficulties in separating the nanometric fraction from the micrometric one in industrially generated quartz dusts. Nearly free silanols were observed on nanoquartz, and their relative amount well correlated with the ability of the nanoquartz to cause membranolysis.
This study provides a new feasible route for the top-down preparation of nanometric quartz with a controlled size and toxicological properties and allowed us to define, for the first time, the physicochemical properties of a nanometric quartz particle that is comparable with the nanometric fraction of an industrial quartz dust.

6.1.3 Details on the interaction between NFS-rich silica particles and biomembranes.

Recently, NFS have been individuated by Pavan and co-workers [11] as the critical molecular moiety that is able to interact with biomembranes and cause the membranolysis of phagolysosomes. However, the details of the interaction were still unclear. In this part of the work, two aspects of the interaction were mainly investigated:

1. The specificity of the interaction between NFS and selected membrane epitopes present on the surface of cellular membranes.
2. The possible role of liquid water molecules, ubiquitous in the body, in mediating the interaction between NFS and biomembranes.

NFS-rich silica particles, both crystalline and amorphous, were characterized and contacted with two different phospholipids (PLs), DOPC and DOPS. The two PLs possess the same lipidic chain but differ for the functional groups present on the phospholipid head. Phosphocholine (PC) is characterized by a positively charged quaternary amine and was able to establish a strong interaction with the silica surface. IR spectroscopy and thermogravimetric analysis allowed us to ascertain that the interaction was irreversible, with the vesicles of DOPC adsorbed on the silica surface. Furthermore, the interaction was NFS-specific. Conversely, phosphoserinic (PS) PLs, characterized by a serinic group, showed a negligible interaction with all silica surfaces, suggesting that the interaction of silica particles with cellular membranes is mediated by specific chemical functionalities of the membrane surface.

DFT calculations allowed us to support the establishment of intermolecular bonds between the quaternary amine of PC and NFS. Such bonds were energetically more stable than the interaction between PS and NFS. PC is a common epitope exposed by several PLs on cellular membranes, including DOPC, DPPC and SM (sphingomyelin). The observed specificity between the PC functional group and NFS suggests an equal interaction with PLs characterized by the same functional group. For the first time, we were able to establish a direct correlation between different phospholipid heads and occurrence of nearly free silanols on the surface of silica particles.

Moreover, the role of interfacial water in the interaction between silica particles and biomembranes was investigated. Even if water was considered in the force-field approximation used in computational calculations on the NFS-PLs interaction, the role of water molecules still remains one of the most intriguing and difficult aspect to investigate. For this purpose, an experimental set up was designed using Sum-Frequency Generation Vibrational (SFG) spectroscopy. SFG is a non-linear optical technique that is sensitive to molecules at the interface. SFG was firstly demonstrated in the 1987 for the study of surfaces of inorganic materials and polymers,[14] and it was used in the last 10 years to characterize the solid-liquid interphase between biomembranes and interfacial water. SFG can characterize the behavior of water at the interface of the biomembranes also in presence of nanoparticles. For this reason, three silica particles were selected for this experiments and contacted with bidimensional biomembranes, and the variation of the water signal at the interface detected. Variations of the signal of interfacial water during the interaction of the nanoparticles with the biomembrane were observed, and correlated with a possible alteration of the structure of the biomembranes. However, it was not possible to establish a causal correlation between the variation of the signal of water and the alteration of the membrane. To strengthen the model, it will be necessary to

investigate a larger panel of silica particles, and support the experimental data with molecular dynamics calculations.

To sum up, the *fil rouge* of my PhD thesis is the study of fractured crystalline silica particles of micrometric size. In particular, new insights on the reactivity of fractured silica surfaces have been elucidated, highlighting the role of water vapor in the surface reconstruction process, and the preservation of the membranolytic potential of silica surface once reached the stability after fracturing. Moreover, for the first time, the properties of a ball milled nanoquartz were investigated, giving new information about the properties of the nanofraction of industrial quartz dusts. Finally, the details of the interaction between nearly free silanols on the surface of fractured quartz were investigated, highlighting the specific interaction of NFS with some molecular epitopes on the surface of cellular membranes.

6.2 Future perspectives.

Considering the large difference in membranolytic activity between milled quartz that was aged in dry or water vapor-rich environments, future research efforts can be aimed to understand how the formation of NFS is achieved in quartz after interaction with water molecules. Having obtained inactive and active milled quartz samples, the evaluation of surface silanols and, specifically, the quantification of NFS will be made possible by further improving the detection methodology. Beside IR, Raman and NMR spectroscopies might be investigated. Finally, to modify the NFS content and reduce the membranolytic effect of quartz, surface chemical modifiers that directly bond to silicon (such as ascorbic acid) can be proposed as agents for the chemical inactivation of NFS and detoxification of silica surface.
To further explore the role of nanoquartz obtained by ball milling, our sample could be effectively used in *in vitro* and *in vivo* tests to assess the relevance of the nanometric fraction on the overall toxic effect of crystalline silica. Particle size distribution by number and quantification of the nanometric fraction could be measured by DCS and DLS on micrometric industrial samples. Separation methods (such as filtering) could be applied to separate the nano-fraction from industrial samples, and the recovery ratios of the nanometric fraction could be compared. Nanometric fraction that is recovered from industrial quartz could be physicochemically characterized (*e.g.,* particle size distribution, degree of amorphism, aggregation behaviour), tested for bioactivity (*e.g.,* membrane lysis, macrophage cytotoxicity), and these properties compared with the nanoquartz prepared by top-down approach.

Finally, the role of the lung milieu, including liquid water and surfactants, in mediating the interaction between NFS and membranes can be clarified by advanced non-linear spectroscopic approaches, including Raman and SFG, adapted to investigate a larger panel of silica particles and by supporting the experimental findings with computational modelling studies.

6.3 Bibliography.

1. IARC, *Silica, some silicates, coal dust and para-aramid fibrils*. Vol. 68. 1997: World Health Organization.
2. IARC, *Silica dust, crystalline, in the form of quartz or cristobalite*, in *Arsenic, Metals, Fibres and Dusts*. 2012, International Agency for Research on Cancer.
3. (IARC), I.A.f.R.o.C., *A Review of Human Carcinogens: Arsenic, Metals, Fibres, and Dusts.* IARC Monographs on the Evaluation of Carcinogenic Risks to Human., 2012. **Vol. 100/C**.
4. Sauvé, J.F., *Historical and emerging workplaces affected by silica exposure since the 1930 Johannesburg conference on Silicosis, with special reference to construction.* American Journal of Industrial Medicine, 2015. **58**(S1): p. 67-71.
5. Kramer, M.R., et al., *Artificial stone silicosis: disease resurgence among artificial stone workers.* Chest, 2012. **142**(2): p. 419-424.
6. Tustin, A.W., et al., *An outbreak of work-related asthma and silicosis at a US countertop manufacturing and fabrication facility.* American Journal of Industrial Medicine, 2022. **65**(1): p. 12-19.
7. Bruch, J., et al., *Variation of biological responses to different respirable quartz flours determined by a vector model.* International Journal of Hygiene and Environmental Health, 2004. **207**(3): p. 203-216.
8. NADLER, S. and S. GOLDFISCHER, *The intracellular release of lysosomal contents in macrophages that have ingested silica.* Journal of Histochemistry & Cytochemistry, 1970. **18**(5): p. 368-371.
9. Pollard, K.M., *Silica, silicosis, and autoimmunity.* Frontiers in immunology, 2016. **7**: p. 97.
10. Turci, F., et al., *Revisiting the paradigm of silica pathogenicity with synthetic quartz crystals: the role of crystallinity and surface disorder.* Particle and Fibre Toxicology, 2016. **13**(1): p. 32.
11. Pavan, C., et al., *Nearly free surface silanols are the critical molecular moieties that initiate the toxicity of silica particles.* Proceedings of the National Academy of Sciences, 2020. **117**(45): p. 27836-27846.
12. Croissant, J.G., et al., *Synthetic amorphous silica nanoparticles: toxicity, biomedical and environmental implications.* Nature Reviews Materials, 2020. **5**(12): p. 886-909.
13. Pavan, C., et al., *Nearly free silanols drive the interaction of crystalline silica polymorphs with membranes: Implications for mineral toxicity.* Frontiers in Chemistry, 2023. **10**.

14. Zhu, X.D., H. Suhr, and Y.R. Shen, *Surface vibrational spectroscopy by infrared-visible sum frequency generation.* Physical Review B, 1987. **35**(6): p. 3047-3050.